Anderson transitions and multifractal finite-size scaling

Ph.D. thesis

László Ujfalusi
Supervisor: Dr. Imre Varga

Budapest University of Technology and Economics
Department of Theoretical Physics

2015

Acknowledgments

I wish to express my gratitude to my supervisor, Dr. Imre Varga, for his invaluable advices, suggestions and for his helpful comments to my thesis. I would like to thank him for his guidance during all these years. I am also very thankful to my family for their support along my whole life. And last but not least, I would like to thank my beloved wife for her everlasting love and support.

Contents

Chapter 1

Introduction

1.1 Motivation

The metal-insulator transition (MIT), and disordered systems have been at the forefront of condensed matter research since the middle of the last century. Our work focuses on Anderson metal insulator transition (AMIT) [1], which has a very wide literature [2, 3, 4, 5], and yet this topic still has several open questions and is still actively investigated. There are several reasons behind this, what we would like to discuss here to shed light on the motivations of this work. We find Ref. [2] especially didactic, therefore we use several thoughts from this review.

We can describe good metals and good insulators at low temperature very well, but they are robust against changing external parameters. This makes the manipulation of the properties of these materials difficult, what would be important for modern technology. Now let us assume that there is an externally tunable parameter which drives the system from a metal to an insulator. This parameter can be for example the number of charge carriers. Figure 1.1 shows the schematic picture of the MIT. For different parameter values one can see a metallic or an insulating behavior below a temperature, T^*, see Figure 1.1(a). This temperature goes to zero exactly at the transition point, which is visible in Figure 1.1(b), while T^* depending on the external parameter separates three regions: the metallic, the critical and the insulating ones. In the critical region, where the MIT occurs, one can change the properties of the matter dramatically by tuning the external parameter.

As mentioned above, T^* reaches zero at the transition point, therefore MIT is a genuine quantum phase transition. Since electric conduction properties are based on the properties of the electrons, and the transition occurs at $T = 0$, quantum fluctuations dominate the critical region. As one expects for a quantum phase transition, we can find universal quantities and universal phenomena. This allows us to investigate relatively simple models, and extract results, which are useful for real materials too. This makes this field very interesting both from the theoretical and the practical point of view.

Although we used the word „relatively" above, these models are rather hard -and therefore still interesting and challenging- to solve analytically for several reasons. Good metals are well-described by Fermi-liquid theory, where the elementary excitations are fermionic quasiparticles: electrons, which can be excited above the Fermi-surface. Good insulators can be described at low temperature usually by collective bosonic excitations,

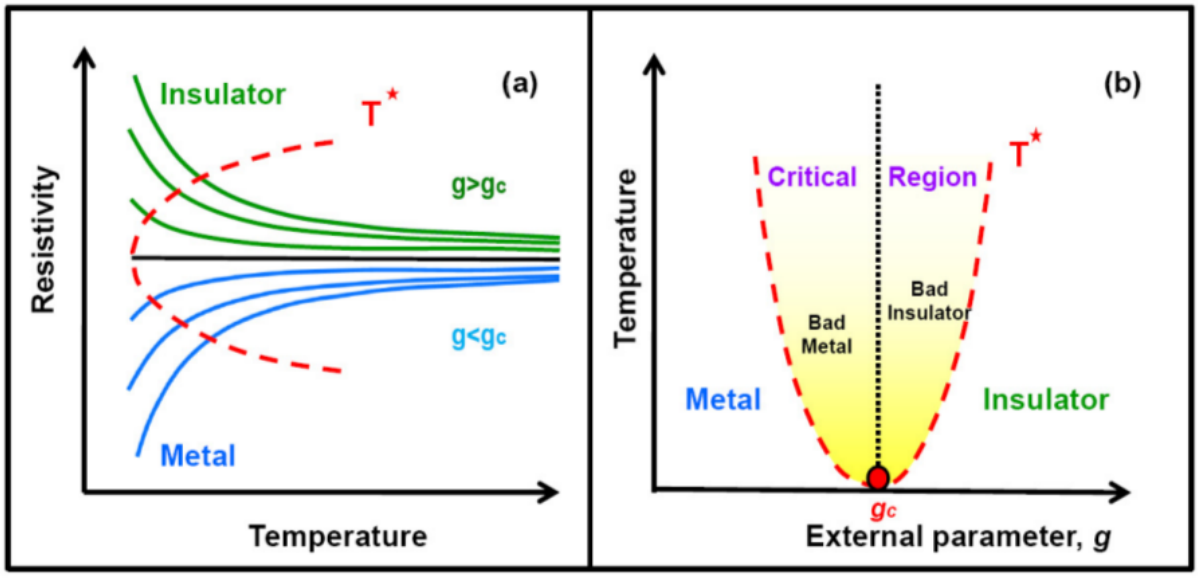

Figure 1.1: Schematic picture of MIT. The figure was taken from the review of Dobrosavljević [2]

like phonons. In between, in the critical regime fermionic and bosonic excitations of the two limiting cases can coexist, which definitely makes theoretical description difficult. Usually phase transitions are related to spontaneous symmetry breaking. For example in the Ising model at zero external field spins break the spin-flip symmetry of the Hamiltonian below T_c leading to a ferromagnetic phase, while the system shows the symmetry above T_c, resulting in a paramagnetic phase. Therefore average magnetization can be used as order parameter. MIT has no such an obvious symmetry-breaking which could lead us to a proper order parameter.

Since analytical description is quite difficult, the development of computational resources in the past decades is crucial for the research. The lower critical dimension for the MIT is in most cases two, therefore many times three-dimensional systems must be investigated numerically. The progress of computational efforts in the past decades allows us to run such large-scale simulations that was not possible not even twenty years ago. In this work we exploit this advancement, too.

There are several reasons, why MIT can occur. We are going to discuss the case in this work, when the MIT is induced by disorder, called Anderson transition (see Section 1.2). However, the effect of disorder sometimes can be neglected, disorder is present in every real system. Moreover, there are systems where disorder plays an important role or even dominates the behavior. One such case is the integer quantum Hall effect, where disordered potential plays a crucial role in the understanding of the plateau transitions [6]. Interestingly disorder can have even positive effect for superconductivity, it can increase the superconducting critical temperature through the large overlap between critical multifractal (see Chapter 2) electronic states [7]. Multifractals have strong fluctuations on every length scale, they are discussed in detail in Chapter 2. Multifractality has an important role in the field of Kondo-physics also, the multifractal fluctuations of the local density of states (LDOS) close to criticality induces a new phase due to the

presence of local Kondo effects induced by local pseudo gaps at the Fermi energy [8]. Anderson localization is present on different topologies also, Sade *et al.* found Anderson localization on various complex networks [9].

Another reason why physicists still examine MIT is that experimental methods also developed a lot lately. In the last few years experimental evidence has been obtained about this topic. Richardella *et al.* [10] examined the MIT in a dilute magnetic semiconductor $Ga_{1-x}Mn_xAs$, which is a strongly interacting and disordered system, which still does not have a complete theoretical description. They used scanning tunneling microscopy, and investigated the LDOS of the excitations. They found a diverging correlation length at the Fermi energy, exponential LDOS autocorrelation function above and below the Fermi energy, and power law LDOS autocorrelation at the Fermi energy, indicating a second order phase transition. Moreover they even found that the LDOS has multifractal fluctuations at the Fermi-energy showing that multifractality is a robust property of critical electronic wave-functions. The group of A. Aspect and P. Bouyer found Anderson-localization in a three-dimensional disordered ultracold atomic system. [11] Although several things can result in the observed localization, they found a time-evolution, which is compatible only with the predictions of Anderson localization. Since Anderson localization is mainly an interference effect (see Section 1.2), not only condensed matter systems can produce the phenomenon. The group of van Tiggelen reported Anderson localization of ultrasound in a three-dimensional elastic network [12], later they found multifractality also [13]. Segev *et al.* found Anderson localization of light in disordered photonic lattices in the transverse direction [14].

Many-body localization [15] is also an actively examined aspect of localization. Its main idea is that if the eigenvectors of the many-body Hamiltonian are localized, the system fails to thermalize. In other words if one prepares the system near to a many-body localized eigenvector, the system cannot be described by usual statistical ensembles, it preserves some reminiscence of the initial state for arbitrarily long time.

1.2 Introduction to Anderson metal insulator transition

Band theory works well for a very wide range of materials, and gives a simple explanation for the conduction properties. But it works only if the kinetic energy of the electrons dominate over all other energy scales. Band theory does not always give a complete description: It can happen that a band is not fully filled, and meanwhile the matter is an insulator.

For example certain metal oxides can be described well by the Hubbard model. If they have an odd number of electrons per unit cell they should be metals according to band theory. If pressure is decreased, the lattice constant increases leading to decreasing hopping integral. If hopping becomes much smaller than the on-site repulsion between the electrons, large energy cost of hopping to an occupied site can prevent the hopping of electrons, this way the material becomes an insulator. The phenomenon is called Mott transition.

Without any interaction, disorder itself can also lead to MIT, known as AMIT or Anderson localization. A schematic figure is seen in Figure 1.2. At zero disorder a crys-

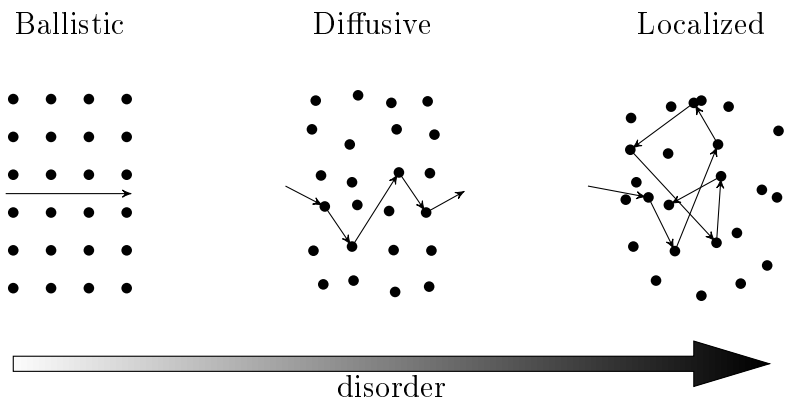

Figure 1.2: The schematic effect of disorder.

tal is periodic, the electronic eigenstates are Bloche-states, the conduction is ballistic. If disorder is induced on a moderate level, conduction becomes diffusive due to scattering, and the usual Drude theory applies. However, if disorder is strong enough, it can trap electrons due to multiple scattering leading to no conduction at all, this way disorder can induce an MIT. Since electrons are quantum waves, it is more appropriate to think about Anderson localization as an interference effect, than multiple bouncing of balls. It has to be noticed that the above reasoning can be applied not just for electrons, but for any kind of wave-phenomena, see Section 1.1. According to Ref. [14], even the opacity of microscopically transparent media, like clouds or milk, might be explained through multiple random scattering of light, which is exactly the phenomenon in Anderson localization.

The random misplacement of the lattice points in Figure 1.2 can be viewed as an additional random potential to the original periodic potential of the lattice. Similar effect can be realized thorough injecting impurities, where the difference of the potential of the randomly placed impurity atoms and the atoms of the lattice can be treated as an additional random potential. If the impurity concentration is small, and therefore the energy scale of the additional random potential is small, its effect can be treated as a perturbation, and Drude model describing a diffusive transport works nicely. On the other hand if impurity concentration is large enough, thus the energy scale of the random potential is larger than the kinetic energy, electrons can get trapped at the impurities. In a condensed matter system of course thermal excitations can move out the electrons from the trap, therefore this phenomenon leads to a real sharp phase transition only at zero temperature, like in Figure 1.1. At finite temperature one can find only a crossover, see also Figure 1.3(b).

The order of the metal insulator phase transition is a non-trivial question. In the late 1970s Mott argued that if Drude model works, disorder only reduces the mean free path, which cannot be shorter than the lattice constant, a. This leads to a minimal Drude-conductivity, $\sigma_{min} = \frac{ne^2a}{mv_F}$ [16], suggesting that the transition is first order. A few years later, however a conductivity much smaller than the Mott-limit was found in a doped semiconductor, Si:P. In Figure 1.3(a) it is shown that conductivity drops down very rapidly near a critical impurity concentration, and conductivity can be two orders of magnitude smaller than the Mott limit suggesting a continuous, second-order phase tran-

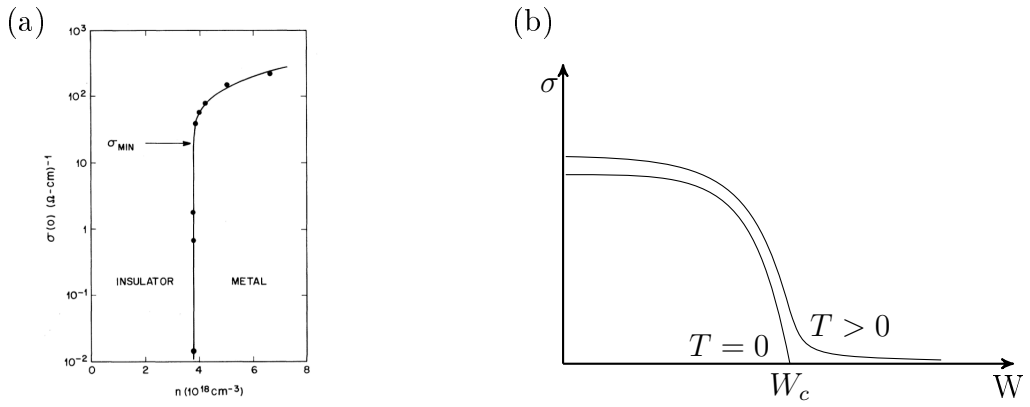

Figure 1.3: Conductivity of disordered systems. (a) First experimental result of Rosenbaum *et al.*[17] suggesting a second-order phase transition using doped semiconductor, Si:P. (b) Schematics of a typical behavior of the conductivity as the function of disorder.

sition. Since then various theoretical works assuming a second-order transition were very successful, such as the non-linear sigma model [18] or one-parameter scaling theory [19]. The result of diverging correlation length and the power-law LDOS autocorrelation at the transition found by Richardella *et al.* [10] is a recent experimental confirmation of the second-order nature of the transition. Figure 1.3(b) shows the schematic behavior of the conductivity as the function of disorder. If disorder, W, is small (metallic regime), at $T = 0$ one finds a decreasing conductivity with increasing disorder. Conductivity tends to zero at a critical value of disorder, W_c, and for $W > W_c$ it remains zero describing an insulator.

As mentioned in Section 1.1, for a second-order phase transition one expects universality, therefore one can extract valid results for universal quantities from any model belonging to the same universality class. We describe different cases in more details in Chapter 4, but now for an introduction we would like to consider one of the simplest models to describe a disordered system: a non-interacting spinless nearest-neighbor tight-binding Hamiltonian, where disorder is introduced through a random on-site potential, called the Anderson model:

$$\mathcal{H}_{\mathcal{A}} = \sum_i \varepsilon_i c_i^\dagger c_i - t \sum_{\langle ij \rangle} c_i^\dagger c_j + h.c. \tag{1.1}$$

For setting the unit of energy it is common to use $t = 1$, for the random potential a W-wide uniform distribution around zero is a usual choice, $\varepsilon_i \in U\left[-\frac{W}{2}, \frac{W}{2}\right]$. Since the Hamiltonian is symmetric on average for reflection of energy, $-E \leftrightarrow E$, every disorder-averaged quantity is a symmetric function of energy, therefore in many cases the range $E \geq 0$ is investigated. Examples for the electronic eigenfunctions for the Anderson model and for the quantum percolation model (see Chapter 5) is visible in Figure 1.4.

If W is large enough, the Hamiltonian is diagonally dominant, and states are typically exponentially localized around a site, see the right column of Figure 1.4. If W is small, the off-diagonal hopping elements (kinetic energy) dominate, and states will extend over the whole system, which is visible in the left column of Figure 1.4. However, in this

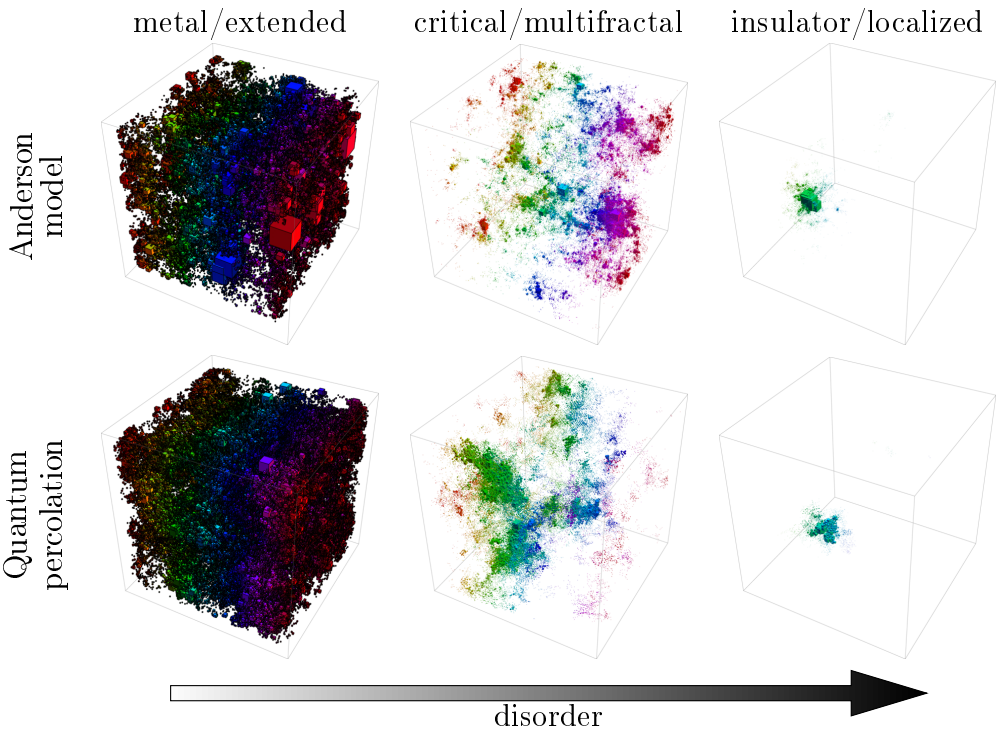

Figure 1.4: First row: Eigenvectors of the Anderson model at $E = 0$ on the metallic side at $W = 14$, close to criticality $W = 16.5$ and on the insulating side at $W = 20$. Second row: Eigenvectors of the quantum percolation model at energy $E = 0.1$ on the metallic side at $p = 0.5$, close to criticality $p = 0.4535$ and on the insulating side at $p = 0.4$. Box sizes correspond to $400 \cdot \sqrt{|\Psi|^2}$ for the left column, $70 \cdot \sqrt{|\Psi|^2}$ in the middle column and $20 \cdot \sqrt{|\Psi|^2}$ in the right column. Multiplying factors were tuned to best sight but without overlapping cubes. System size is $L = 120$ for all subfigures. Coloring is due to x coordinate.

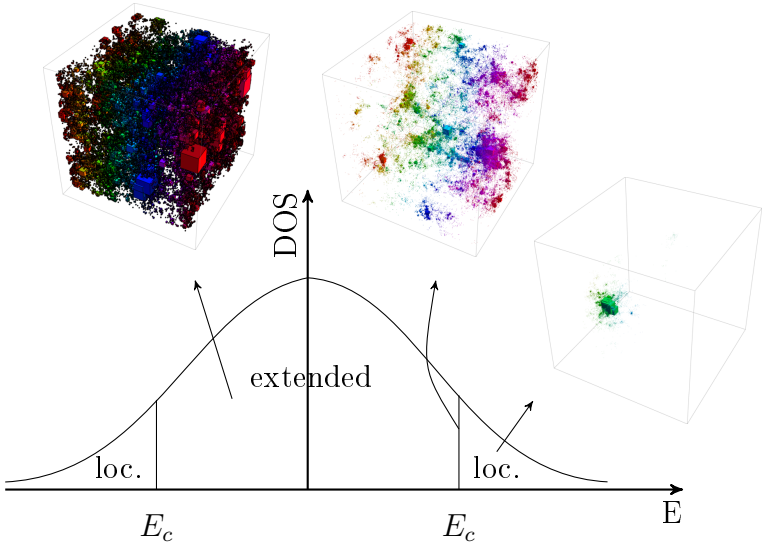

Figure 1.5: Typical structure of a disordered band, E_c denotes the mobility edge separating extended and localized states.

case there are localized states in the system also, separated in energy from the extended states by the so-called mobility edge, E_c, see Figure 1.5. The reason why a mobility edge should exist is the following: Suppose that there is a localized state in the energy regime of extended states. Due to perturbation theory with an infinitesimal change of the random disorder the localized state hybridizes with the extended states to a new extended state. Even though there is no rigorous proof for localized states being near the edge of the band and for extended states being in the middle of the band, mostly this is the situation. On the other hand approaching the very edge of the band, beyond the critical energies, $E_\pm$, one finds the so-called Lifschitz-tail [4, 20] which consists of strongly localized states. In this region the density of states decreases rapidly, with a typical functional form $DOS(E) = Ae^{-B(\pm(E-E\pm))^\alpha}$.

Figure 1.5 actually explains, how a disordered material with unfilled band can be an insulator. If the Fermi-energy, E_F, is in the localized regime, electrons near E_F are exponentially localized, hence no conduction is possible. Now by changing E_F for example with a gate voltage, one can shift E_F into the extended region, and one can measure a finite conduction. In between, exactly at the mobility edge, E_c, electronic eigenstates are multifractals, see the middle column of Figure 1.4, here the critical behavior can be measured. For theoretical computations sometimes it is more convenient to fix the energy, E, and change the disorder. With increasing disorder the mobility edges start to shift towards to band center, and it reaches the examined energy value at a certain value of disorder. As written above, one can find critical behavior at this specific energy-disorder combination resulting an energy-dependent critical disorder-value, $W_c(E)$. The $W_c(E)$ curve, which is often referred to as the mobility edge curve, for the model described here is seen in Figure 1.6.

With growing disorder the mobility edge moves away from the band center, but of course in the meantime the band also widens with the increasing disorder. Then it turns

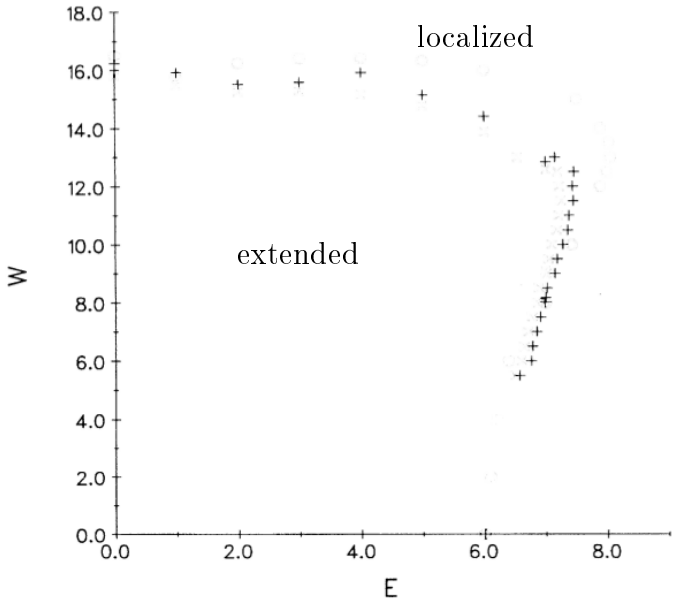

Figure 1.6: The critical disorder as the function of energy, $W_c(E)$, or in other words the mobility edge curve of the Anderson model [21].

back, and moves rapidly in, leading to a large interval, $0 \leq E \leq 4.0$, where the mobility edge is roughly constant. At a certain critical disorder, $W_c \approx 16.5$, the mobility edge curve reaches zero energy, i.e. the two mobility edges, $\pm E_c$, merge at $E = 0$. This point is usually called the critical point of the system, since increasing disorder beyond this limit, $W > W_c$, the whole band will consist of localized states. The trajectory of the mobility edge is continuous, so the number of extended states varies continuously with disorder if the density of states, DOS, is continuous. Since these extended states are responsible for the conductance of the system, it is plausible that the conductance also varies continuously with disorder suggesting a second-order transition again.

1.3 Global symmetries

The latest theoretical and experimental works, discussed in Section 1.1, show an increased interest in understanding the nature of the Anderson transition in the presence of various global symmetries. A comprehensive review of the current understanding is given in Ref. [5]. These symmetry classes have been introduced first to describe random matrix ensembles, but the naming conventions are the same in the field of disordered systems.

The original classification considers two global symmetries: time-reversal and spin-rotational symmetry. If time-reversal and spin-rotational symmetries are also present, the Hamiltonian is invariant under orthogonal transformations, thus it is a real symmetric operator. This class is called the orthogonal class. If time-reversal symmetry is broken, which can be realized physically by applying a magnetic field, the system is invariant under unitary transformations. The Hamiltonian is a complex hermitian operator in this

case, and it belongs to the unitary class. It can be shown that either spin rotational symmetry is broken or not, the model is in the unitary class. In the symplectic class time-reversal symmetry is present, and spin-rotational symmetry is broken, which describes a system with spin-orbit interaction. In this case the Hamiltonian is invariant under symplectic transformations, leading to a quaternion hermitian operator. These three classes are called together the Wigner-Dyson (WD) classes. Since time-reversal symmetry can be represented by an anti-unitary symmetry operator, A, the classification can be formulated the following way also: The absence of any anti-unitary symmetry, corresponds to the unitary class. If an anti-unitary symmetry is present, there are two cases. If $A^2 = I$, the system belongs to the orthogonal class, if $A^2 = -I$, it belongs to the symplectic class.

The reason why naming conventions come from the field of random matrix theory is that in the metallic phase the eigenvalue statistics of disordered systems is well-described by eigenvalue statistics of random matrices with the same symmetry. For example the nearest level spacing distribution, $P(s)$, characterizes the probability distribution of having two eigenvalues separated by an energy distance s. For random matrices and disordered systems in the metallic phase this function is well-described by the Wigner-Dyson distribution, which has Gaussian envelope, and it is proportional to s^β for $s \ll 1$ with $\beta = 1, 2$ and 4 for the orthogonal, unitary and symplectic class, leading to level repulsion. Meanwhile the nearest level spacing distribution of a disordered system in the insulating regime follows the distribution of a random diagonal matrix, $\sim e^{-s}$, called Poisson statistics. The first numerical works on disordered systems used the $P(s)$ functions in the two phases to obtain critical properties.

Later it turned out that there are three more symmetry classes according to the presence of chiral symmetry beside the above symmetries, leading to the chiral orthogonal, chiral unitary and chiral symplectic classes. By chirality we mean that there exists an operator C, such that $C^\dagger C = C^2 = 1$ holds that anticommutes with the Hamiltonian, $\{C, \mathcal{H}\} = 0$. Therefore these models are symmetric not only on average for the exchange of eigenenergies, $-E \leftrightarrow E$, but for every single disorder realization. A chiral disordered system can be realized for example by off-diagonal disorder on a bipartite lattice, where the hopping elements are random, and on-site terms are the same, hence set to zero. In the chiral classes the band center, $E = 0$, is a special point in the spectrum, and many anomalies were found in this regime [22]. We discuss anomalies also in Section 5.3. On the other hand according to Ref. [22] the bulk of the spectrum behaves similarly to the corresponding non-chiral class. For example the authors of Ref. [22] found Wigner-Dyson statistics in the bulk spectrum of a three-dimensional chiral orthogonal disordered model. Moreover even the critical exponent of the orthogonal and chiral orthogonal class which will be defined in Section 3.1, turns out to be the same numerically up to a very high precision [23]. These show that in the bulk of the corresponding chiral and non-chiral classes are very similar, chirality affects the band center mainly.

For the sake of completeness we mention that there are four Bogoliubov-de Gennes classes also, corresponding to particle-hole symmetry [5], but the examination of these classes is beyond the scope of our work.

The structure of this work is the following: First we introduce and describe the theoretical background of the concepts and tools we use later, therefore in Chapter 2 we introduce multifractals, and in Chapter 3 we describe finite-size scaling laws and

their usage for multifractal quantities, called multifractal finite-size scaling. In the next Chapters we show how powerful multifractal finite-size scaling is for various problems of disordered systems: For Anderson models in the three Wigner-Dyson classes (Chapter 4) and for the quantum percolation model (Chapter 5). In Chapter 6 we show that at very strong disorder Anderson models can be described -at least qualitatively- by simple analytically solvable two- and three-site models. In Chapter 7 we use multifractal finite-size scaling for quantum chromodynamics. After these, in Chapter 8, we list the thesis points, publications and the acronyms we use.

Chapter 2

Multifractals

2.1 Fractals

A fractal is a set with non-integer dimension. Dimension can be defined through the box counting algorithm, and the result is the so called box dimension. The main idea of the definition is to cover the set with N hypercubes with linear size ℓ, and let $\lambda = \frac{\ell}{L}$ be the portion of ℓ and the full linear size of the system, L. The resulting number of necessary boxes $N \propto \lambda^{-D}$, as $\lambda \to 0$, therefore $D = -\lim_{\lambda \to 0} \frac{\ln N}{\ln \lambda}$. A fractional dimension can be produced with a recursion method, like for the Koch snowflake, but fractals in nature usually are not coming from a recursion, there is no strict deterministic rule to produce them. Their self-similarity is a statistical property: any measurable average quantity shows scale independence, and as an outcome of the box counting algorithm the dimension is non-integer. For example the borderline of the geometric clusters of the Ising model at the critical point is this kind of fractal, with dimension $D = \frac{187}{96}$ [24]. At criticality Ising model does not change during renormalization, thus it must be statistically the same on all length scales (scale independence), which means self similarity. Critical systems are fixed points of renormalization flows, thus one expects that some kind of fractality appears in critical systems.

2.2 Introduction to multifractals

Multifractals are the generalization of fractals [25], and since we will use them to analyze simulation data, we will define them on a lattice, not on a continuum. For an introduction, let us consider first a little handwaving picture of multifractals. A multifractal, p, is a normalized probability distribution function on a d-dimensional hypercube with linear size L, $\sum_{i=1}^{L^d} p_i = 1$. Such a multifractal function is depicted in two dimensions in Figure 2.1(a) and (b) as an example. p fluctuates in a very broad range, therefore it seems useful to investigate its logarithm, or more precisely the variable $\alpha = -\frac{\ln p}{\ln L}$, see Figure 2.1(c) and (d). One can cut this α function and obtain the contour of it at different values, see Figure 2.2. The mass corresponding to a contour is given by the probability distribution of alpha:

$$\mathcal{P}(\alpha) \sim L^{f(\alpha)}, \tag{2.1}$$

where $f(\alpha)$ is the fractal dimension of the contour at height α:

$$f(\alpha) = \lim_{L\to\infty} \frac{\ln \mathcal{P}(\alpha)}{\ln L}. \tag{2.2}$$

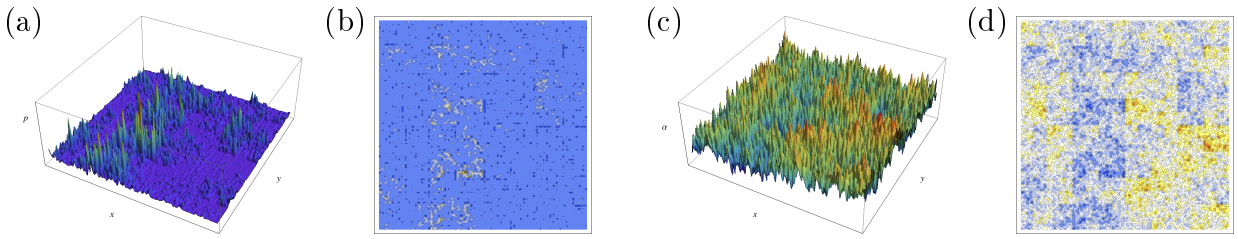

Figure 2.1: A multifractal, p, and its transformed variable, α over a two dimensional lattice on a 3D plot ((a) and (c)) and on a contour plot ((b) and (d)).

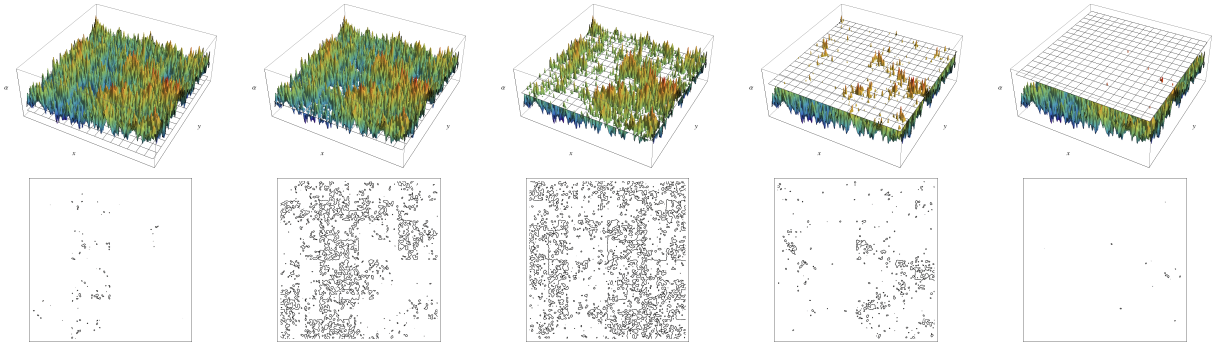

Figure 2.2: Upper row: The α function cut at different levels. Lower row: Contours obtained by cutting the α function at different values.

For a regular set or a regular fractal, $\mathcal{S}$, p is a uniform distribution over $\mathcal{S}$:

$$p_i = \begin{cases} L^{-D_f}, \text{ if } i \in \mathcal{S} \\ 0, \text{ otherwise} \end{cases}, \tag{2.3}$$

where D_f stands for the fractal dimension of $\mathcal{S}$. In this case $\mathcal{P}(\alpha) = \delta(\alpha - D_f)$. The $\mathcal{P}(\alpha)$ distribution has a final width for a multifractal, and its scaling is described by $f(\alpha)$.

The multifractal quantities can be precisely defined on a lattice in the following way: First take a d-dimensional hypercubic lattice with linear size L, and a normalized probability on it, $\sum i = 1^{L^d} p_i = 1$. Divide this lattice into smaller hypercubes (boxes) with size ℓ, and introduce the ratio $\lambda = \frac{\ell}{L}$. With coarse graining p_i, in other words with summing all its values in the kth box, we obtain:

$$\mu_{k,\lambda} = \sum_{i \in box_k} p_i, \tag{2.4}$$

$\mu_{k,\lambda}$ is the weight associated to the kth box termed as box–probability. As an average over boxes α can be obtained, from which $\mathcal{P}(\alpha)$ can be computed which leads to the definition of $f(\alpha)$ as

$$\alpha = \lim_{\lambda\to 0} \frac{\ln \langle \mu_\lambda \rangle}{\ln \lambda} \qquad \mathcal{P}(\alpha) \sim \lambda^{f(\alpha)} \qquad f(\alpha) = -\lim_{\lambda\to 0} \frac{\ln \mathcal{P}(\alpha)}{\ln \lambda}. \tag{2.5}$$

$f(\alpha)$ is called the singularity spectrum, and describes the usual fractal dimension of the set of points having value α. Later we would like to investigate disordered system, where averaging over different disorder-realizations is essential. Therefore for a disordered system, the $\langle . \rangle$ sign in Eq. (2.5) means average over disorder too, as it will mean that later in the thesis also.

There is another way to describe multifractals through the qth moment of the mass, frequently called generalized inverse participation ratio (GIPR), and it's derivative:

$$R_q = \sum_{k=1}^{\lambda^{-d}} \mu_k^q \qquad S_q = \frac{dR_q}{dq} = \sum_{k=1}^{\lambda^{-d}} \mu_k^q \ln \mu_k, \tag{2.6}$$

The average of R_q and S_q follows a power-law behavior as a function of $\lambda = \frac{\ell}{L}$, with exponent τ_q and α_q:

$$\tau_q = \lim_{\lambda\to 0} \frac{\ln \langle R_q \rangle}{\ln \lambda} \qquad \alpha_q = \frac{d\tau_q}{dq} = \lim_{\lambda\to 0} \frac{\langle S_q \rangle}{\langle R_q \rangle \ln \lambda}. \tag{2.7}$$

τ_q can be written in the form:

$$\tau_q = D_q(q-1) = d(q-1) + \Delta_q, \tag{2.8}$$

where D_q is the generalized fractal dimension, and Δ_q is the anomalous scaling exponent:

$$D_q = \frac{1}{q-1} \lim_{\lambda\to 0} \frac{\ln \langle R_q \rangle}{\ln \lambda} \qquad \Delta_q = (D_q - d)(q-1). \tag{2.9}$$

The function $f(\alpha)$ and τ_q are related through Legendre-transformation:

$$f(\alpha_q) = q\alpha_q - \tau_q = q\alpha_q - D_q(q-1). \tag{2.10}$$

τ_q, α_q, D_q and Δ_q are often referred to as multifractal exponents (MFEs). D_q is directly related to the so-called *Rényi-entropy*, $H_q = -\frac{\ln \langle R_q \rangle}{q-1}$, which in the limit $q \to 1$ yields the well-known *Shannon-entropy*, i.e. $-\left\langle \sum_k \mu_k \ln \mu_k \right\rangle$. This is the reason why D_1 is also referred to as information dimension:

$$D_1 = \lim_{q\to 1} \frac{1}{q-1} \lim_{\lambda\to 0} \frac{\ln \langle R_q \rangle}{\ln \lambda} \overset{L'H}{=} \alpha_1 = \lim_{\lambda\to 0} \frac{1}{\ln \lambda} \left\langle \sum_{k=1}^{\lambda^{-d}} \mu_k \ln \mu_k \right\rangle, \tag{2.11}$$

while another frequently used dimension is the correlation dimension, D_2. The latter dimension appeared often in recent studies of the physical relevance of multifractal eigenstates [26]. A schematic figure of the above MFEs is depicted in Figure 2.3. Easy to

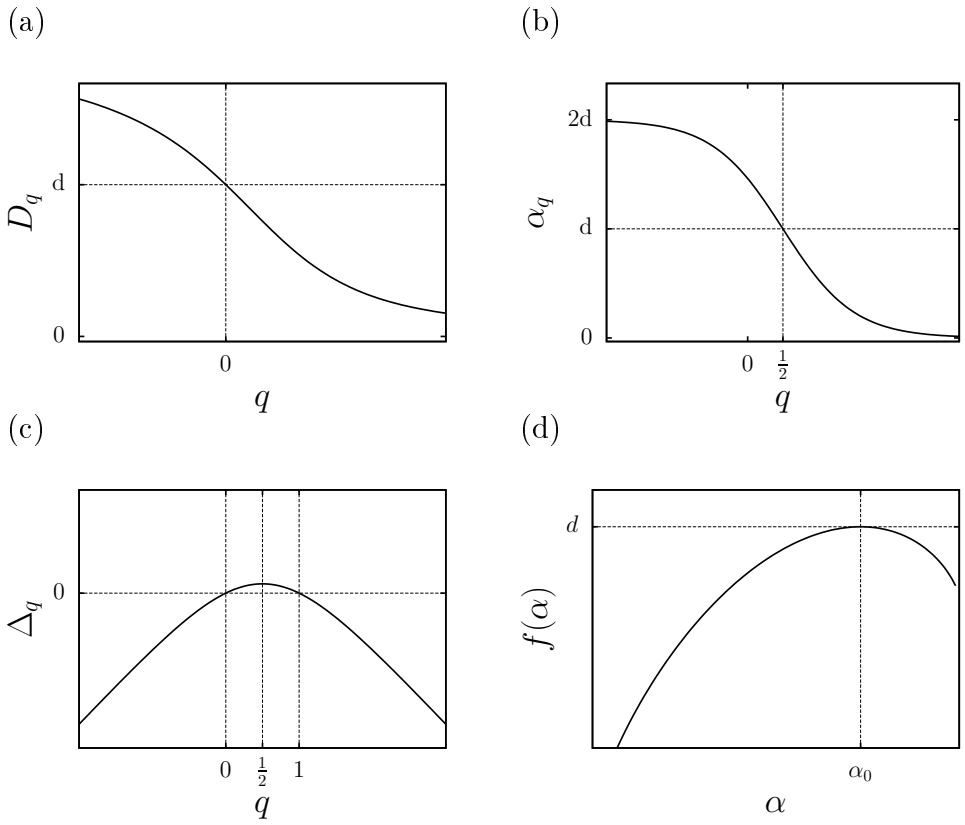

Figure 2.3: Schematic behavior of MFEs.

check that for a regular fractal D_q and α_q are q-independent, and $D_q \equiv \alpha_q = D_f$. In this sense multifractals are generalized fractals.

According to recent results a symmetry relation exists for α_q and Δ_q given in the form [27]:

$$\Delta_q = \Delta_{1-q} \qquad \alpha_q + \alpha_{1-q} = 2d \tag{2.12}$$

This relation was first obtained for some random matrix ensemble numerically and using the supersymmetric non-linear sigma model analytically [27]. It was later confirmed for several two dimensional [28, 29] and three-dimensional systems [30]. The robustness of this relation has been investigated also for many-body localization [31].

2.3 Numerical calculation of GMFEs

For numerical approaches one has to define the finite-size version of these MFEs at a particular value of disorder, termed as generalized multifractal exponents (GMFEs), $\tilde{\tau}_q$, $\tilde{\alpha}_q$, $\tilde{D}_q$ and $\tilde{\Delta}_q$.

For a quantummechanical system, the absolute value square of the wave-function defines a natural probability measure in real space, therefore the obvious choice for μ_k is

$$\mu_k = \sum_{i \in box_k} |\Psi_i|^2 . \tag{2.13}$$

With the above μ_k from the eigenfunction R_q and S_q can be computed according to Eq. (2.6) for every state at different values of q. Later we would like to investigate

Anderson transitions, where disorder, denoted by W, drives the system through the transition, which occurs at a critical value of disorder, W_c. The value of the GMFEs depends on disorder of course, therefore at fixed W, system size, L, and box size, ℓ, every finite size GMFE is computable from R_q and S_q in the following way [32]:

$$\tilde{\tau}_q^{ens}(W,L,\ell) = \frac{\ln\langle R_q\rangle}{\ln\lambda} \qquad \tilde{\tau}_q^{typ}(W,L,\ell) = \frac{\langle \ln R_q\rangle}{\ln\lambda} \tag{2.14a}$$

$$\tilde{\alpha}_q^{ens}(W,L,\ell) = \frac{\langle S_q\rangle}{\langle R_q\rangle \ln\lambda} \qquad \tilde{\alpha}_q^{typ}(W,L,\ell) = \left\langle \frac{S_q}{R_q}\right\rangle \frac{1}{\ln\lambda} \tag{2.14b}$$

$$\tilde{D}_q^{ens}(W,L,\ell) = \frac{1}{q-1}\frac{\ln\langle R_q\rangle}{\ln\lambda} \qquad \tilde{D}_q^{typ}(W,L,\ell) = \frac{1}{q-1}\frac{\langle \ln R_q\rangle}{\ln\lambda} \tag{2.14c}$$

$$\tilde{\Delta}_q^{ens}(W,L,\ell) = \frac{\ln\langle R_q\rangle}{\ln\lambda} - d(q-1) \qquad \tilde{\Delta}_q^{typ}(W,L,\ell) = \frac{\langle \ln R_q\rangle}{\ln\lambda} - d(q-1), \tag{2.14d}$$

where *ens* and *typ* denote the *ensemble* and *typical* averaging over disorder. Every GMFE approaches the value of the corresponding MFE at the critical point, $W = W_c$, only in the limit $\lambda \to 0$, when self-similarity and therefore multifractality is expected.

We would like to emphasize that τ_q – and therefore every MFE – in principle is defined through *ensemble* averaging (see Eqs. (2.7) and (2.9)), and *ensemble* and *typical* averaged MFEs are equal only in a range of q [5]. It can be shown that

$$\tau_q^{typ} = \begin{cases} q\alpha_{q_-}, & \text{if } q < q_- \\ \tau_q^{ens}, & \text{if } q_- < q < q_+ \\ q\alpha_{q_+}, & \text{if } q_+ < q \end{cases}, \tag{2.15}$$

where q_- and q_+ correspond to values, where the singularity spectrum reaches zero, $f(\alpha_{q_\pm}) = 0$. Therefore when we compute an MFE later, we will use *ensemble* averaging always.

The choice of the investigated range of q is influenced by the following three effects. If q is big, the qth power in Eq. (2.6) enhances the numerical and statistical errors, leading to a noisy dataset. If q is negative with large absolute value, the relatively less precise small wave-function values dominate the sums in Eq. (2.6), which also results in a noisy dataset. These two effects together lead to a regime $q_{min} \leq q \leq q_{max}$, where GMFEs behave numerically the best. The third effect is that coarse graining suppresses the noise. For $\ell > 1$ in an $\ell \times \ell \times \ell$ sized box positive and negative errors on the wave-functions can cancel each other. Besides in a box large and small wave-function amplitudes appear together with high probability, and this way the relative error of a μ_k box probability is reduced. In other words coarse graining has a nice smoothing effect, which can help to widen the investigable range of q.

Chapter 3

Finite-size scaling

3.1 Introduction

Scaling theory [33] has been proven to be very useful for solving various statistical physics problems. Anderson transition can be very efficiently described in the frame of one parameter scaling theory introduced by the „gang of four", Abrahams, Anderson, Licciardello and Ramakrishnan in 1979 [19] based on the ideas of Thouless [34] and Wegner [35]. The dimensionless conductance, $g = \frac{2e^2}{h}G$, of a sample is the function of the linear size of the sample, L, and the dimensionless disorder $w = \frac{W-W_c}{W_c}$: $g = g(L, w)$. Putting together b^d pieces of these systems, yields to a system with linear size bL, see Figure 3.1(a), with conductance, $g(bL, w)$. According to one parameter scaling theory the conductance of the big and the original system is related as

$$\ln g(bL, w) = F\left(\ln g(L, w), b\right), \tag{3.1}$$

or in continuous form

$$\frac{d \ln g(L, w)}{d \ln L} = \beta\left(\ln g(L, w)\right) \tag{3.2}$$

meaning, that the conductance of the rescaled system depends on the scaling factor, b, and the original conductance only. From the renormalization point of view $\beta > 0$ ($\beta < 0$) means, that the system shifts towards a metallic (insulating) fixed point, since the conductance increases (decreases) in a renormalization step. In between there should be an unstable critical fixed point of the renormalization flow corresponding to $\beta = 0$. In the metallic regime for large conductance, $g \gg 1$, in the Ohmic limit

$$g = \frac{2\hbar}{e^2}\sigma L^{d-2} \;\Rightarrow\; \beta(\ln g) = d - 2 \tag{3.3}$$

holds, where σ is the conductivity of the sample. In the insulating regime, $g \ll 1$, due to exponentially localized wave-functions g reads as

$$g = g_0 e^{-\frac{L}{\xi}} \;\Rightarrow\; \beta(\ln g) = \ln g - \ln g_0, \tag{3.4}$$

where ξ is the localization length of the electrons. On the metallic side the important length scale is the correlation length, that we are going to denote also with ξ, since localization length on the insulating side and correlation length on the metallic side of the transition play similar role from the point of view of scaling theory.

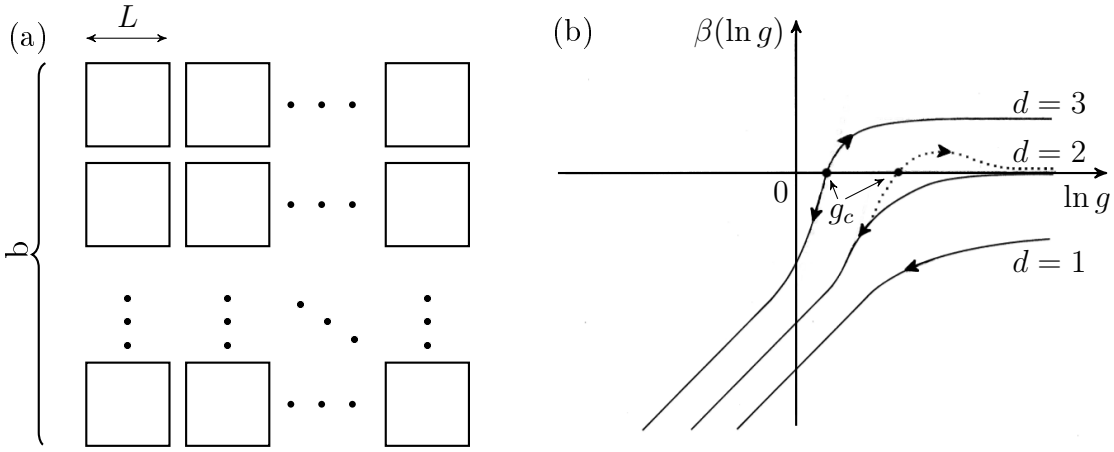

Figure 3.1: (a) Schematic figure for the renormalization. (b) $\beta(\ln g)$ in different dimensions. Dotted line stands for the *symplectic* symmetry class in two dimensions. The figure is based on Figure 1 of the article of Abrahams *et al.* [19]. Arrows show the directions of the renormalization flow, the critical point is marked with g_c.

Using perturbation theory around the metallic fixed point for weak localization the first non-vanishing correction happens to be negative for the *orthogonal* and the *unitary* symmetry classes, but positive for the *symplectic* class [5]. β is assumed to be continuous, therefore its schematic shape looks like Figure 3.1(b), resulting critical point and Anderson metal-insulator transition in three dimensions and in two dimensions for the *symplectic* class only.

Let us denote the derivative of the β function at the critical point with s, $\frac{d\beta(\ln g)}{d\ln g}\big|_{g_c} = s$. Near the critical point up to linear order

$$\frac{d\ln g}{d\ln L} = s(\ln g - \ln g_c) \quad \Rightarrow \quad \frac{1}{\ln g - \ln g_c} d(\ln g) = s \cdot d(\ln L) \tag{3.5}$$

holds. Let us integrate both sides of this equation from a lower bound L_0 and g_0, a microscopic cutoff and the corresponding conductance, to an upper bound, ξ and g_c, the correlation length and the critical conductance. Since for a system having size $L > \xi$ one basically sees a critical system, the above $\xi \leftrightarrow g_c$ pairing is proper. The result of the integration is

$$\ln \frac{g_0}{g_c} = \left(\frac{\xi}{L_0}\right)^{-s} \quad \Rightarrow \quad \xi \sim \left(\ln \frac{g_0}{g_c}\right)^{-\frac{1}{s}}. \tag{3.6}$$

Since $\ln \frac{g_0}{g_c} \approx \frac{g_0 - g_c}{g_c}$, and $g - g_c \sim W - W_c$ is expected,

$$\xi \sim w^{-\nu}, \tag{3.7}$$

where the the variable $\nu = \frac{1}{s}$ is introduced describing the divergence of the correlation/localization length near the transition point, called the critical exponent. Considering higher order terms leads to

$$\xi \sim \varrho(w)^{-\nu}, \tag{3.8}$$

where $\varrho(w) \approx w$ for $w \ll 1$.

3.2 Multifractal finite-size scaling (MFSS)

3.2.1 Introduction

In recent high-precision calculations [32] MFEs (see Chapter 2) have been used to describe the AMIT. The renormalization flow of the AMIT, as mentioned in the Section 3.1, has three fixed points: a metallic, an insulating and a critical one. In the metallic fixed point every state is extended with probability one, thus with increasing system size, the effective size of the states also grows proportional to the volume. So the fractal dimension of the states, is just the embedding dimension q-independently, $D_q^{met} \equiv d$. In the insulating fixed point every state is exponentially localized, their effective size does not change with growing system size, thus for $q > 0$ $D_q^{ins} \equiv 0$, for $q < 0$ $D_q^{ins} \equiv \infty$. At criticality the system does not change during renormalization, thus it must be statistically the same on all length scales showing scale independence, which means self similarity. Therefore wave-functions are multifractals, in other words generalized fractals [25], see Figure 1.4.

Close to the critical point due to standard finite-size scaling arguments we can suppose that the average of R_q and S_q shows scaling behavior determined only by the ratio of two length scales, L and ℓ, and the localization/correlation length, ξ, in the insulating/metallic phase:

$$\langle R_q \rangle (W, L, \ell) = \lambda^{\tau_q} \mathcal{R}_q \left(\frac{L}{\xi}, \frac{\ell}{\xi} \right). \tag{3.9}$$

According to Eqs. (2.14a)–(2.14d) for all GMFEs the scaling-law holds independently from the type of averaging [32]:

$$\tilde{\tau}_q(W, L, \ell) = \tau_q + \frac{q(q-1)}{\ln \lambda} \mathcal{T}_q \left(\frac{L}{\xi}, \frac{\ell}{\xi} \right) \tag{3.10a}$$

$$\tilde{\alpha}_q(W, L, \ell) = \alpha_q + \frac{1}{\ln \lambda} \mathcal{A}_q \left(\frac{L}{\xi}, \frac{\ell}{\xi} \right) \tag{3.10b}$$

$$\tilde{D}_q(W, L, \ell) = D_q + \frac{q}{\ln \lambda} \mathcal{T}_q \left(\frac{L}{\xi}, \frac{\ell}{\xi} \right) \tag{3.10c}$$

$$\tilde{\Delta}_q(W, L, \ell) = \Delta_q + \frac{q(q-1)}{\ln \lambda} \mathcal{T}_q \left(\frac{L}{\xi}, \frac{\ell}{\xi} \right), \tag{3.10d}$$

Since Eqs. (3.10a)–(3.10d) has the same structure, one can summarize them in one equation, using a common letter, G, for the GMFEs:

$$\tilde{G}_q(W, L, \ell) = G_q + \frac{1}{\ln \lambda} \mathcal{G}_q \left(\frac{L}{\xi}, \frac{\ell}{\xi} \right). \tag{3.11}$$

(L, ℓ) on the left-hand side and $\left(\frac{L}{\xi}, \frac{\ell}{\xi} \right)$ on the right-hand side can be changed to (L, λ) and $\left(\frac{L}{\xi}, \lambda \right)$:

$$\tilde{G}_q(W, L, \lambda) = G_q + \frac{1}{\ln \lambda} \mathcal{G}_q \left(\frac{L}{\xi}, \lambda \right). \tag{3.12}$$

Our goal is to fit the above formulas to the numerically obtained data, where W_c, ν, G_q and y (irrelevant exponent) appear among the fit parameters. This fit procedure will provide us the physically interesting quantities and confidence intervals. In the next subsections we are going to present different methods for the finite-size scaling.

3.2.2 Finite-size scaling at fixed λ

At fixed λ, G_q and the $\frac{1}{\ln\lambda}$ factor in Eq. (3.12) can be merged with the constant term of $\mathcal{G}_q$, therefore

$$\tilde{G}_q(W,L) = \mathcal{G}_q\left(\frac{L}{\xi}\right), \tag{3.13}$$

where the constant λ has been dropped from the notations. $\mathcal{G}_q$ can be expanded with one relevant, $\varrho(w)$, and one irrelevant variable, $\eta(w)$, by using Eq.(3.8) the following way:

$$\tilde{G}_q(W,L) = \mathcal{G}_q\left(\varrho L^{\frac{1}{\nu}}, \eta L^{-y}\right) = \mathcal{G}_q^r\left(\varrho L^{\frac{1}{\nu}}\right) + \eta L^{-y}\mathcal{G}_q^{ir}\left(\varrho L^{\frac{1}{\nu}}\right), \tag{3.14}$$

where $\varrho L^{\frac{1}{\nu}}$ is used instead of $\varrho^\nu L$ for better numerical stability. It is important to mention that the irrelevant term is not dangerously irrelevant, therefore the formula above can be applied. All the disorder-dependent quantities in the above formula can be expanded in Taylor-series:

$$\mathcal{G}_q^r\left(\varrho L^{\frac{1}{\nu}}\right) = \sum_{i=0}^{n_r} a_i \left(\varrho L^{\frac{1}{\nu}}\right)^i \tag{3.15}$$

$$\mathcal{G}_q^{ir}\left(\varrho L^{\frac{1}{\nu}}\right) = \sum_{i=0}^{n_{ir}} b_i \left(\varrho L^{\frac{1}{\nu}}\right)^i \tag{3.16}$$

$$\varrho(w) = w + \sum_{i=2}^{n_\varrho} c_i w^i \qquad \eta(w) = 1 + \sum_{i=1}^{n_\eta} d_i w^i \tag{3.17}$$

The advantage of this method is that in the Taylor-series only one variable appears, $\varrho L^{\frac{1}{\nu}}$, therefore the number of parameters (including W_c, ν and y) is $n_r + n_{ir} + n_\rho + n_\eta + 4$, which grows linear with the expansion orders. This method is very effective for computing W_c, ν, and y, but since λ is fixed, one can not obtain the MFEs. In all cases we used $\lambda = 0.1$ (except in Chapter 7), because it leads to excellent results in Ref. [32]. It seems that it is small enough to capture the details of a wave-function, and it allows a lot different system sizes in the $20 \leq L \leq 100$ range, what we investigated. This way we can also compare our results to the results of Ref. [32] very well.

3.2.3 Finite-size scaling for varying λ

In order to take into account different values of λ, the scaling law given in Eq. (3.11) has to be considered. The expansion of $\mathcal{G}$ in (3.11) is

$$\begin{aligned}\mathcal{G}_q\left(\varrho L^{\frac{1}{\nu}}, \varrho\ell^{\frac{1}{\nu}}, \eta' L^{-y'}, \eta\ell^{-y}\right) = \mathcal{G}_q^r\left(\varrho L^{\frac{1}{\nu}}, \varrho\ell^{\frac{1}{\nu}}\right) + \\ +\eta' L^{-y'}\mathcal{G}_q^{ir}\left(\varrho L^{\frac{1}{\nu}}, \varrho\ell^{\frac{1}{\nu}}\right) + \eta\ell^{-y}\mathcal{G}_q^{ir}\left(\varrho L^{\frac{1}{\nu}}, \varrho\ell^{\frac{1}{\nu}}\right).\end{aligned} \tag{3.18}$$

According to the numerical results of Rodriguez *et al.* [32] the most important irrelevant term is the one containing the finite box size, ℓ, therefore we took into account that only. This leads to

$$\tilde{G}_q(W,L,\ell) = G_q + \frac{1}{\ln\lambda}\left(\mathcal{G}_q^r\left(\varrho L^{\frac{1}{\nu}}, \varrho\ell^{\frac{1}{\nu}}\right) + \eta\ell^{-y}\mathcal{G}_q^{ir}\left(\varrho L^{\frac{1}{\nu}}, \varrho\ell^{\frac{1}{\nu}}\right)\right). \tag{3.19}$$

The Taylor-expansions of the above functions are

$$\mathcal{G}_q^r\left(\varrho L^{\frac{1}{\nu}}, \varrho \ell^{\frac{1}{\nu}}\right) = \sum_{i=0}^{n_r}\sum_{j=0}^{i} a_{ij}\varrho^i L^{\frac{j}{\nu}}\ell^{\frac{i-j}{\nu}} \tag{3.20}$$

$$\mathcal{G}_q^{ir}\left(\varrho L^{\frac{1}{\nu}}, \varrho \ell^{\frac{1}{\nu}}\right) = \sum_{i=0}^{n_{ir}}\sum_{j=0}^{i} b_{ij}\varrho^i L^{\frac{j}{\nu}}\ell^{\frac{i-j}{\nu}} \tag{3.21}$$

$$\varrho_{(w)} = w + \sum_{i=2}^{n_\varrho} c_i w^i \qquad \eta_{(w)} = 1 + \sum_{i=1}^{n_\eta} d_i w^i \tag{3.22}$$

The advantage of this method is that it provides the MFE, since it is one of the parameters to fit, G_q. There are also many more data to fit compared to the fixed λ case. Fixed λ means that at a given system size one can use GMFEs obtained at a certain ℓ – the one that leads to the desired λ – , while in this case one can fit to GMFEs obtained at different values of ℓ. However, these GMFEs are correlated, because they are the result of coarse graining the same wave-functions with different sizes of boxes. During the fitting procedure one has to take into account these correlations, see Section 3.2.5. Since the relevant and irrelevant scaling functions have two variables, $\varrho L^{\frac{1}{\nu}}$ and $\varrho \ell^{\frac{1}{\nu}}$, one has to fit a two-variable function with the number of parameters $(n_r+1)(n_r+2)/2+(n_{ir}+1)(n_{ir}+2)/2+n_\rho+n_\eta+3$. We can see that the number of parameters grows as $\sim n_{r/ir}^2$, instead of as $\sim n_{r/ir}$ as for fixed λ. This makes the fitting procedure -together with the correlations- definitely much more difficult.

3.2.4 Finite-size scaling at fixed $\ell = 1$

For fixed ℓ the scaling law given in Eq. (3.11) has to be considered also. The expansion of $\mathcal{G}$ in Eq. (3.11) reads still as Eq. (3.18). Choosing $\ell = 1$, and considering that in most cases η and η' are constant, i.e. $n_\eta = 0$, the last term can be merged with the relevant part. Equation (3.11) has the following form for fixed $\ell = 1$ (leaving the $'$ of one remaining irrelevant term):

$$\tilde{G}_q(W, L) = G_q + \frac{1}{\ln L}\left(\mathcal{G}_q^r\left(\varrho L^{\frac{1}{\nu}}, \varrho\right) + \eta L^{-y}\mathcal{G}_q^{ir}\left(\varrho L^{\frac{1}{\nu}}, \varrho\right)\right). \tag{3.23}$$

The Taylor-expansions of the above functions are

$$\mathcal{G}_q^r\left(\varrho L^{\frac{1}{\nu}}, \varrho\right) = \sum_{i=0}^{n_r}\sum_{j=0}^{i} a_{ij}\varrho^i L^{\frac{j}{\nu}} \tag{3.24}$$

$$\mathcal{G}_q^{ir}\left(\varrho L^{\frac{1}{\nu}}, \varrho\right) = \sum_{i=0}^{n_{ir}}\sum_{j=0}^{i} b_{ij}\varrho^i L^{\frac{j}{\nu}} \tag{3.25}$$

$$\varrho_{(w)} = w + \sum_{i=2}^{n_\varrho} c_i w^i \qquad \eta_{(w)} = 1 + \sum_{i=1}^{n_\eta} d_i w^i \tag{3.26}$$

The advantage of this method is that it can be used for irregular lattices or graphs also, where it is nontrivial how to introduce boxes. Since GMFEs obtained at $\ell = 1$ are

used only, there are no correlations. On the other hand according to the arguments of Section 2.3 the smoothing effect of coarse graining is missing at $\ell = 1$, therefore the noise is bigger. Besides there is less data to fit, and one has to fit a two-variable function with the number of parameters $\sim n_{r/ir}^2$, which is the most difficult from the three cases considered in this work.

3.2.5 General principles for the FSS fit procedures

In this section we would like to discuss the details of the methods and criteria we used during the MFSS. In order to fit the scaling law Eq. (3.14), (3.19) or (3.23) we used the MINUIT library [36]. To find the best fit to the data, obtained numerically, the order of expansion of $\mathcal{G}_q^{r/ir}$, ϱ and η must be decided by choosing the values of n_r, n_{ir}, n_ϱ and n_η. Since the relevant operator is more important than the irrelevant one we always used $n_{rel} \geq n_{ir}$ and $n_\varrho \geq n_\eta$. To choose the order of the expansion we used basically three criteria. The first criterion we took into account was to check how close the ratio $\chi^2/(N_{df} - 1)$ approached unity. Let us denote the numerically obtained data points by y_i, the fit function value at the ith parameter value by f_i, and the covariance matrix of the numerically obtained data points by C, which can be computed numerically with a similar expression to the variance. With these notations χ^2 reads as

$$\chi^2 = \sum_{i,j} (y_i - f_i) \left(C^{-1}\right)_{ij} (y_j - f_j), \tag{3.27}$$

for more details see Ref. [32]. If the data points are not correlated, C is a diagonal matrix, and the expression leads to the usual form:

$$\chi^2 = \sum_i \frac{(y_i - f_i)^2}{\sigma_i^2}. \tag{3.28}$$

Let us use the notation N_{df} for the number of degrees of freedom, namely the number of data points minus the number of fit parameters. A ratio $\chi^2/(N_{df} - 1) \approx 1$ means that the deviations from the best fit are of the order of the standard deviation (covariance matrix). The second criterion was that the fit has to be stable against changing the expansion orders, i.e. adding a few new expansion terms. From the fits that fulfilled the first two criteria we chose the simplest model, with the lowest expansion orders. Sometimes we also took into account the error bars, and we chose the model with the lowest error bar for the most important quantities (W_c, ν, *etc*...), if similar models fulfilled the first two criteria.

The error bars of the best fit parameters were obtained by a Monte-Carlo simulation. The data points are results of averaging, so due to the central limit theorem, they have a Gaussian distribution. Therefore we generated Gaussian random numbers with parameters corresponding the mean of the raw data points and standard deviation (or covariance matrix) of the mean, and then found the best fit. Repeating this procedure $N_{\rm MC} = 100$ times provided the distribution of the fit parameters. We chose 95% confidence level to obtain the error bars.

Unfortunately for the fixed $\ell = 1$ case the fits were not so stable against changing the expansion orders, as the ones for example for fixed λ, because at fixed $\ell = 1$ we had to fit

much more parameters to the same amount of data. The value of the critical point must be q-independent, which – contrary to the other two methods – we had to keep also as a criterion. we had to compare fits at different values of q and choose the lowest expansion orders that led to a q-independent critical point, and still had $\chi^2/(N_{df}-1)$ ratio close to one. In some cases we also had to leave out the smallest system size(s) to fulfill the criteria above.

Chapter 4

MFSS for the three-dimensional Anderson models in the conventional Wigner-Dyson symmetry classes: orthogonal, unitary and symplectic class

4.1 Introduction

Our goal in this section is to compute critical quantities of Anderson models in the three conventional Wigner-Dyson (WD) classes, which were introduced in Section 1.3. To this end we apply the MFSS toolkit – see Section 3.2 –, developed by Rodriguez, Vasquez, Slevin and Römer [32, 37], to Anderson models in the WD classes. In these cases there is no chiral and no particle-hole symmetry. We will investigate the case of diagonal disorder and nearest-neighbor hopping only, therefore the Hamiltonian reads as

$$\mathcal{H} = \sum_{i\sigma} \varepsilon_i c^\dagger_{i\sigma} c_{i\sigma} - \sum_{\langle ij\rangle\sigma\sigma'} t_{ij\sigma\sigma'} c^\dagger_{i\sigma} c_{j\sigma'} + h.c., \tag{4.1}$$

where i, j and σ, σ' stand for site- and spin indexes, ε_i-s are random on-site energies, which are random uniformly distributed numbers over the interval $\left[-\frac{W}{2}, \frac{W}{2}\right]$, W acts as disorder. Using uniform distribution is just a convention, other distributions of disorder, like Gaussian, can be used as well.

4.2 Numerical method, and representations of the symmetries

In the orthogonal class time-reversal and spin-rotational symmetries are preserved, the Hamiltonian is a real symmetric matrix. Since spin does not play a role, we consider a spinless Anderson model. In the numerical simulations the Hamiltonian is represented by an $N \times N$ real symmetric matrix, where $N = L^3$, and L is the linear system size in

lattice spacing. The diagonal elements, are uniformly distributed random numbers, the off-diagonal elements are zero, except for the case, when i and j are nearest neighbors:

$$H_{ij}^{O} = \begin{cases} \varepsilon_i \in U\left[-\frac{W}{2}, \frac{W}{2}\right], \text{ if } i = j \\ -1, \text{ if } i \text{ and } j \text{ are neighboring sites} \\ 0, \text{ otherwise} \end{cases} \tag{4.2}$$

The energy unit is fixed by setting the hopping elements to unity. To avoid surface effects, we use periodic boundary conditions. Even though this case was investigated very deeply by Rodriguez *et al.* [32], we consider this symmetry class to verify our numerical method, and to obtain complete description of all the WD classes.

In the unitary class time-reversal symmetry is broken, the Hamiltonian is a complex hermitian matrix. We discuss the case when spin-rotational symmetry is present, because this way we can use spinless fermions again, which keeps the matrix size $N \times N$. However, one has to store about twice as much data compared to the orthogonal case, because here every off-diagonal matrix element is complex. Finding an eigenvalue and an eigenvector takes more time also. For the numerical simulations we follow the method described by Slevin and Ohtsuki [38]. Let us consider a magnetic field pointing in the y direction with flux Φ, measured in units of the flux quantum, $\frac{h}{e}$. Its effect can be represented by a unity phase factor for the hopping elements of the Hamiltonian matrix. The upper triangular of the Hamiltonian reads as

$$H_{i\leq j}^{U} = \begin{cases} \varepsilon_i \in U\left[-\frac{W}{2}, \frac{W}{2}\right], \text{ if } i = j \\ -1, \text{ if } i \text{ and } j \text{ are neighboring sites in the } x \text{ or } y \text{ direction} \\ -e^{i2\pi\Phi x}, \text{ if } i \text{ and } j \text{ are neighboring sites in the } z \text{ direction} \\ 0, \text{ otherwise} \end{cases} \tag{4.3}$$

Complex hermiticity defines the off-diagonal elements in the lower triangular part, $j < i$. Periodic boundary conditions and flux quantization force a restriction for the magnetic flux, namely that $\Phi \cdot L$ must be an integer. In the thermodynamic limit, arbitrarily small magnetic field drives the system from the orthogonal to the unitary class. However, in a finite system the relationship between the system size, L, and the magnetic length, $L_H = \frac{1}{\sqrt{2\pi\Phi}}$ matters. In the case of weak magnetic field, $L \ll L_H$, the system belongs to the orthogonal class, in the case of strong magnetic field, $L \gg L_H$, it belongs to the unitary class. Since we use system sizes that are multiples of 10 lattice spacings, see Table 4.1, we chose $\Phi = \frac{1}{5}$. This leads to $L_H \approx 0.892$, therefore this choice clearly fulfills the two conditions above.

In the symplectic class time-reversal symmetry is present, and spin-rotational symmetry is broken, therefore the Hamiltonian is a quaternion hermitian matrix. For the numerical simulations we followed the method described by Asada, Slevin and Ohtsuki [39]. Since in this case we have to deal with the spin index also, the Hamiltonian is a $2N \times 2N$ complex hermitian matrix. Diagonal elements corresponding to the ith site and hopping elements between sites i and j are 2×2 matrices because of the spin indexes, having a form

$$\epsilon_i = \begin{pmatrix} \varepsilon_i & 0 \\ 0 & \varepsilon_i \end{pmatrix} \qquad t_{ij} = \begin{pmatrix} e^{i\alpha_{ij}\cos\beta_{ij}} & e^{i\gamma_{ij}\sin\beta_{ij}} \\ -e^{-i\gamma_{ij}\sin\beta_{ij}} & e^{-i\alpha_{ij}\cos\beta_{ij}} \end{pmatrix}, \tag{4.4}$$

system size (L)	number of samples
20	15000
30	15000
40	15000
50	15000
60	10000
70	7500
80	5000
90	4000
100	3500

Table 4.1: System sizes and number of samples for the simulation for each WD symmetry class.

where ε_i is still a uniformly distributed random on-site energy from the interval $\left[-\frac{W}{2}, \frac{W}{2}\right]$, α_{ij}, β_{ij} and γ_{ij} were chosen to form an SU(2)-invariant parametrization, leading to the so-called SU(2) model: α_{ij} and γ_{ij} are uniform random variables from the interval $[0, 2\pi]$, and β has a probability density function $p(\beta)d\beta = \sin(2\beta)d\beta$ in the range $\left[0, \frac{\pi}{2}\right]$. The upper triangular of the Hamiltonian has the following form:

$$H^S_{i\leq j} = \begin{cases} \epsilon_i, \text{ if } i = j \\ t_{ij}, \text{ if } i \text{ and } j \text{ are neighboring sites} \\ 0, \text{ otherwise} \end{cases} \tag{4.5}$$

The off-diagonal elements in the lower triangular are defined following complex hermiticity. To store the Hamiltonian requires about eight times more space compared to the orthogonal case, because here every off-diagonal element contains four complex numbers. Finding an eigenvalue is much slower than for the unitary case, mainly because the linear size of the matrix is twice as large.

MFSS deals with the eigenvectors of the Hamiltonian, which is a large sparse matrix. Recent high precision calculations [32] use Jacobi-Davidson iteration with incomplete LU preconditioning, therefore we decided to use this combination. For preconditioning ILUPACK [40] was used, for the JD iteration the PRIMME [41] package was used. Since the metal-insulator transition occurs at the band center [5] ($E = 0$) at disorder $W_c^O \approx 16.5$ for the orthogonal, at $W_c^U \approx 18.3$ for the unitary (depending on the strength of magnetic field), at $W_c^S \approx 20$ for the symplectic class (for our parameters), most works study the vicinity of these points. To have the best comparison, we analyzed this regime also, therefore about 20 disorder values were taken from the range $15 \leq W \leq 18$ for the orthogonal class, 23 disorder values were taken from the interval $17 \leq W \leq 20$ for the unitary class, and 20 disorder values were taken from the interval $19.4 \leq W \leq 20.5$ for the symplectic class. System sizes were taken from the range $L = 20..100$, the number of samples are listed in Table 4.1.

We considered only one wave-function per realization, the one with energy closest to zero in order to avoid correlations between wave-functions of the same system [32]. From the eigenvectors every GMFE is computable. Since only $\mathcal{A}_q$ and $\mathcal{T}_q$ appear as a scaling function in Eqs.(3.10a)–(3.10d), we used only the $\tilde{\alpha_q}$ and $\tilde{D_q}$ GMFEs for the MFSS. We

investigated the range $-1 \leq q \leq 2$, because GMFEs behave the best in this regime. As written in the end of Section 2.3, if q is a negative number with large absolute value, the smallest, and – because of the numerical errors – the most uncertain wave-function values dominate the sums of Eq. 2.6, which enhance noise. If q is much larger than 1, numerical uncertainties also increase in Eq. 2.6, because of the qth power in the formulas.

4.3 Results of the MFSS at fixed $\lambda = 0.1$

The typical behavior of the GMFEs is presented in Figure 4.1. In all cases there is a clear sign of phase transition: With increasing system size the GMFEs tend to opposite direction on two sides of their crossing point. Note that there is no well-defined crossing point due to the irrelevant term in Eq. (3.14). Applying the MFSS method described in Section 3.2.2 with the principles of Section 3.2.5 to the raw data leads to a well fitting function, see the red lines on Figure 4.1. After the subtraction of the irrelevant part from the raw data, plotting it as a function of $\varrho L^{\frac{1}{\nu}}$ results a scaling function also, see the insets of Figure 4.1.

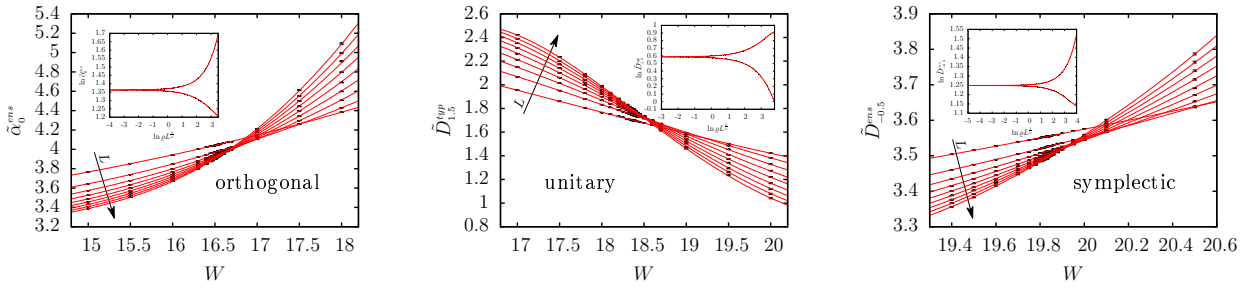

Figure 4.1: Dots are the raw data for different GMFEs in the conventional WD symmetry classes. Red line is the best fit obtained by MFSS. Insets are scaling functions on a log-log scale, after the irrelevant term was subtracted. Error bars are shown only on the large figures, in order not to overcomplicate the insets.

The MFSS provided us the critical point, W_c, the critical exponent, ν, and the irrelevant exponent, y at every investigated values of q. The numerical results are listed in Table 4.2–4.4, and visible in Figure 4.2.

The parameters of the critical point correspond to the system itself, therefore it should not depend on the quantity we used to find it. In other words it should be independent of q, averaging method and the GMFE we used. From Figure 4.2 it is clear that this requirement is fulfilled very nicely. There is a small deviation for the irrelevant exponent, y, obtained from α^{typ} at $q = -1$ and $q = -0.75$ in the unitary and symplectic class, but since y describes the subleading part, it is very hard to determine, and we cannot exclude some sort of underestimation of the error bar of this exponent. Another interesting feature of the results is that the error bars are getting bigger as q grows above 1. As written in Section 2.3, large q enhances the errors through the qth power in Eq. (2.6), leading to bigger error bars. A similar effect can be seen around $q \approx -1$, where the relatively less precise small wave-function values dominate the sums in Eq. (2.6), which

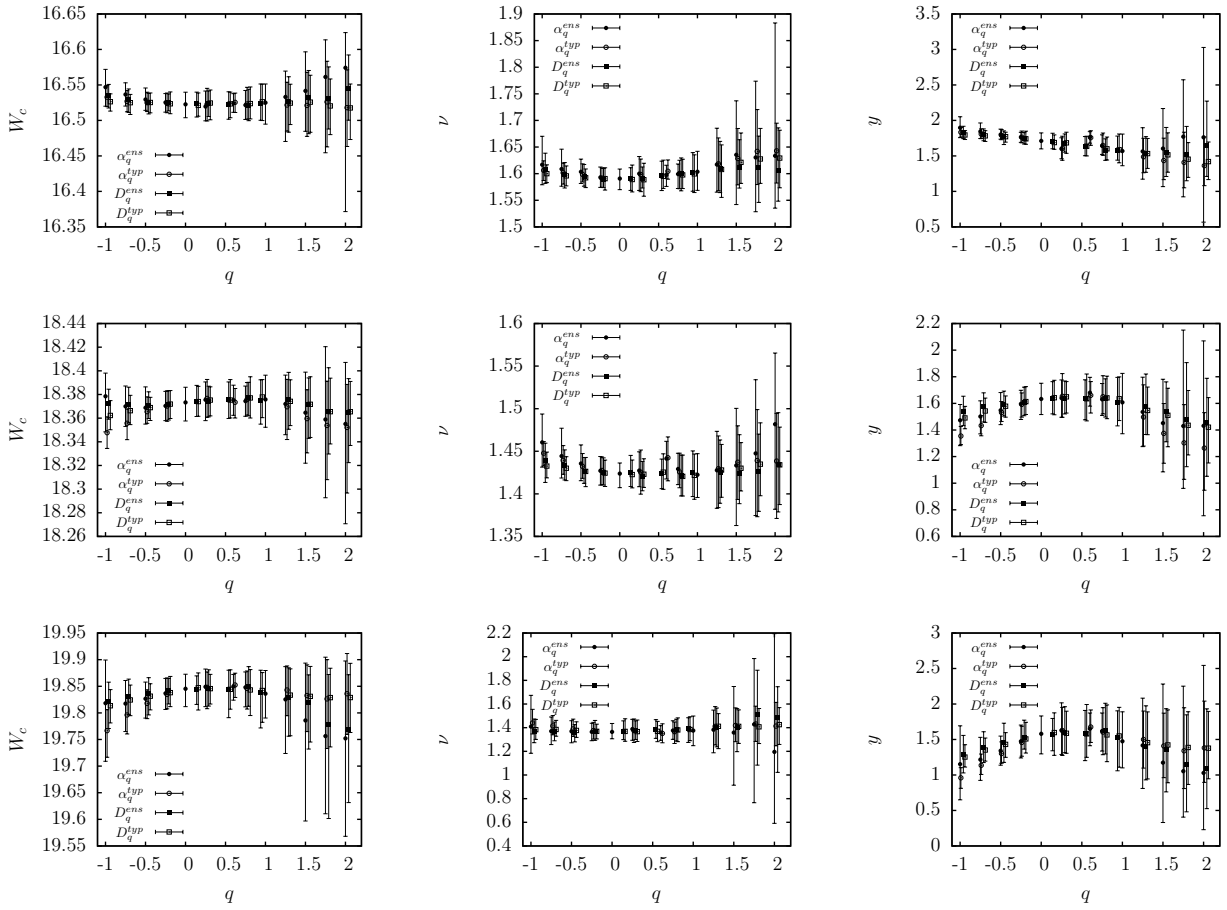

Figure 4.2: Critical parameters of the Anderson models in WD classes obtained by MFSS at fixed $\lambda = 0.1$. First row corresponds to the orthogonal class, second row corresponds to the unitary class, and third row corresponds to the symplectic class. The corresponding numerical values are listed in Table 4.2–4.4 alongside with the parameters of the fit method.

can also contribute to the deviation of y obtained from $\tilde{\alpha}^{typ}$ in this regime. These two effects together lead to our investigated interval $-1 \leq q \leq 2$, where GMFEs behave the best. The results are strongly correlated, since they were obtained from the same wavefunctions, therefore they cannot be averaged. We are going to choose a typical point from the dataset to describe the values of the critical parameters.

In the orthogonal class the critical parameters obtained from $\tilde{\alpha}_{0.6}^{ens}$ are the following: $W_c^{O\lambda} = 16.524\,(16.511..16.538)$, $\nu^{O\lambda} = 1.598\,(1.576..1.616)$ and $y^{O\lambda} = 1.763\,(1.679..1.842)$. These values are in excellent agreement with the most recent high precision result of Rodriguez *et al.* [32], $W_{c\,Rod}^{O\lambda} = 16.517\,(16.498..16.533)$, $\nu_{Rod}^{O\lambda} = 1.612\,(1.593..1.631)$ and $y_{Rod}^{O\lambda} = 1.67\,(1.53..1.80)$, obtained from $\tilde{\alpha}_0$ with the same method (fixed λ). This agreement verifies our numerics and fit method, and makes it reliable for the other two universality classes.

In the unitary class we selected the critical parameters obtained from $\tilde{\alpha}_0$: $W_c^{U\lambda} = 18.373\,(18.358..18.386)$, $\nu^{U\lambda} = 1.424\,(1.407..1.436)$ and $y^{U\lambda} = 1.636\,(1.521..1.763)$. Our

values match with the results of Slevin and Ohtsuki [38], $W_{c\ Sle}^{U} = 18.375$ (18.358..18.392) and $\nu_{Sle}^{U} = 1.43$ (1.37..1.49), obtained by transfer matrix method (they did not published the value of the irrelevant exponent). They used magnetic flux $\Phi = \frac{1}{4}$, while we used $\Phi = \frac{1}{5}$, and according to Dröse *et al.* [42], W_c^U depends on the applied magnetic flux. However, in Figure2. of Ref. [42] it can be seen that the critical points at $\Phi = \frac{1}{4}$ and $\Phi = \frac{1}{5}$ are very close to each other, hence the agreement between our critical point and the result of Slevin and Ohtsuki.

For the symplectic class we chose the critical parameters obtained from $\tilde{D}_{-0.25}^{typ}$: $W_c^{S\lambda} = 19.838$ (19.812..19.869), $\nu^{S\lambda} = 1.369$ (1.305..1.343) and $y^{S\lambda} = 1.508$ (1.309..1.743). These results agree more or less with the values of Asada, Slevin and Ohtsuki [39], $W_{c\ Asa}^{S} = 20.001$ (19.984..20.018), $\nu_{Asa}^{S} = 1.375$ (1.359..1.391) and $y_{Asa}^{S} = 2.5$ (1.7..3.3), obtained by transfer matrix method. However, the difference does not seem to be very large, our critical point is significantly different, even though we used exactly the same model. Due to bigger computational resources we could investigate much bigger system sizes than they did, therefore it possible that they underestimated the role of the irrelevant scaling, resulting a little bit higher critical point.

The critical points are higher in the unitary and in the symplectic class, than in the orthogonal class, showing that broken time-reversal or spin-rotational symmetry requires more disorder to localize wave-functions. Since the value of the critical point in the unitary and symplectic class can be influenced by the applied magnetic flux and the strength of the spin-orbit coupling, the relationship between $W_c^{U\lambda}$ and $W_c^{S\lambda}$ probably depends on these two parameters. However, because of their close value of the critical exponents, $\nu^{U\lambda}$ and $\nu^{S\lambda}$ are the same within our confidence interval, the following relation appears: $\nu^{O\lambda} > \nu^{U\lambda} \geq \nu^{S\lambda}$. We would like to note that a bit different values for these exponents – obtained at slightly different parameters – also appear in Refs. [38] and [39], which are significantly different from each other, conforming the relation $\nu^U > \nu^S$. Similar is the situation for the irrelevant exponent, namely that they are the same within error bar, but $y^{O\lambda}$ seems to be slightly higher than $y^{U\lambda}$, which is a bit higher than $y^{S\lambda}$.

q	exp	$W_c^{O\lambda}$	$\nu^{O\lambda}$	$y^{O\lambda}$	N_{df}	χ^2	$n_r n_{ir} n_\varrho n_\eta$
-1	α^{ens}	16.547 (16.520..16.572)	1.617 (1.579..1.670)	1.897 (1.758..2.052)	170	182	4 3 1 0
	α^{typ}	16.533 (16.520..16.549)	1.606 (1.587..1.624)	1.833 (1.765..1.901)	172	187	3 2 1 0
	D^{ens}	16.535 (16.517..16.551)	1.609 (1.582..1.639)	1.832 (1.744..1.917)	171	183	4 2 1 0
	D^{typ}	16.526 (16.513..16.538)	1.600 (1.583..1.617)	1.795 (1.731..1.856)	171	187	4 2 1 0
-0.75	α^{ens}	16.537 (16.520..16.553)	1.609 (1.576..1.646)	1.844 (1.745..1.964)	170	179	4 3 1 0
	α^{typ}	16.527 (16.512..16.542)	1.602 (1.580..1.620)	1.810 (1.744..1.881)	171	187	4 2 1 0
	D^{ens}	16.529 (16.511..16.544)	1.598 (1.573..1.621)	1.797 (1.714..1.881)	171	184	4 2 1 0
	D^{typ}	16.525 (16.508..16.537)	1.596 (1.577..1.615)	1.783 (1.704..1.856)	171	186	4 2 1 0
-0.5	α^{ens}	16.529 (16.514..16.546)	1.603 (1.582..1.627)	1.802 (1.736..1.878)	171	183	4 2 1 0
	α^{typ}	16.525 (16.512..16.540)	1.599 (1.585..1.618)	1.791 (1.728..1.872)	171	188	4 2 1 0
	D^{ens}	16.526 (16.509..16.538)	1.595 (1.576..1.617)	1.767 (1.660..1.853)	171	185	4 2 1 0
	D^{typ}	16.525 (16.511..16.539)	1.592 (1.574..1.609)	1.771 (1.694..1.835)	171	185	4 2 1 0
-0.25	α^{ens}	16.525 (16.512..16.538)	1.593 (1.574..1.613)	1.765 (1.692..1.832)	171	185	4 2 1 0
	α^{typ}	16.524 (16.511..16.539)	1.592 (1.574..1.611)	1.765 (1.685..1.850)	171	186	4 2 1 0
	D^{ens}	16.525 (16.514..16.537)	1.589 (1.574..1.610)	1.745 (1.668..1.829)	171	184	4 2 1 0
	D^{typ}	16.523 (16.509..16.540)	1.591 (1.569..1.611)	1.741 (1.664..1.848)	171	184	4 2 1 0
0	$\alpha^{ens/typ}$	16.523 (16.504..16.540)	1.591 (1.570..1.609)	1.712 (1.599..1.824)	171	181	4 2 1 0
0.1	D^{ens}	16.524 (16.505..16.540)	1.590 (1.569..1.611)	1.706 (1.601..1.820)	171	180	4 2 1 0
	D^{typ}	16.521 (16.506..16.539)	1.589 (1.566..1.616)	1.688 (1.593..1.796)	171	180	4 2 1 0
0.25	α^{ens}	16.520 (16.500..16.541)	1.600 (1.568..1.632)	1.599 (1.460..1.755)	171	170	4 2 1 0
	α^{typ}	16.523 (16.499..16.545)	1.598 (1.566..1.627)	1.605 (1.438..1.778)	171	171	4 2 1 0
	D^{ens}	16.523 (16.506..16.542)	1.590 (1.573..1.613)	1.680 (1.554..1.810)	171	177	4 2 1 0
	D^{typ}	16.524 (16.501..16.543)	1.589 (1.558..1.620)	1.685 (1.537..1.834)	171	177	4 2 1 0
0.5	D^{ens}	16.522 (16.502..16.540)	1.597 (1.568..1.623)	1.636 (1.503..1.773)	171	173	4 2 1 0
	D^{typ}	16.523 (16.504..16.540)	1.595 (1.572..1.625)	1.637 (1.500..1.778)	171	174	4 2 1 0
0.6	α^{ens}	16.524 (16.511..16.538)	1.598 (1.576..1.616)	1.763 (1.679..1.842)	172	176	3 2 1 0
	α^{typ}	16.526 (16.511..16.538)	1.605 (1.590..1.626)	1.758 (1.650..1.855)	172	178	3 2 1 0
0.75	α^{ens}	16.522 (16.501..16.542)	1.599 (1.572..1.618)	1.642 (1.521..1.798)	171	170	4 2 1 0
	α^{typ}	16.523 (16.502..16.547)	1.600 (1.572..1.625)	1.648 (1.509..1.823)	171	172	4 2 1 0
	D^{ens}	16.520 (16.500..16.544)	1.600 (1.568..1.630)	1.579 (1.438..1.741)	171	175	4 2 1 0
	D^{typ}	16.524 (16.502..16.547)	1.598 (1.572..1.627)	1.600 (1.442..1.766)	171	176	4 2 1 0
0.9	D^{ens}	16.524 (16.500..16.551)	1.602 (1.567..1.640)	1.578 (1.440..1.780)	171	178	4 2 1 0
	D^{typ}	16.526 (16.500..16.551)	1.600 (1.564..1.635)	1.587 (1.402..1.809)	171	179	4 2 1 0
1	$\alpha^{ens/typ}$	16.525 (16.495..16.551)	1.604 (1.569..1.642)	1.569 (1.362..1.808)	171	180	4 2 1 0
1.25	α^{ens}	16.533 (16.470..16.570)	1.617 (1.565..1.685)	1.564 (1.173..1.897)	172	187	3 2 1 0
	α^{typ}	16.522 (16.485..16.554)	1.619 (1.568..1.667)	1.488 (1.263..1.748)	171	178	4 2 1 0
	D^{ens}	16.527 (16.483..16.562)	1.610 (1.564..1.661)	1.528 (1.269..1.771)	171	185	4 2 1 0
	D^{typ}	16.524 (16.494..16.551)	1.608 (1.555..1.654)	1.533 (1.324..1.745)	171	180	4 2 1 0
1.5	α^{ens}	16.542 (16.485..16.597)	1.635 (1.542..1.737)	1.604 (1.068..2.167)	171	184	4 2 1 0
	α^{typ}	16.521 (16.478..16.568)	1.629 (1.579..1.685)	1.435 (1.165..1.751)	171	171	4 2 1 0
	D^{ens}	16.532 (16.481..16.570)	1.612 (1.573..1.664)	1.555 (1.210..1.901)	172	186	3 2 1 0
	D^{typ}	16.526 (16.483..16.564)	1.621 (1.582..1.676)	1.516 (1.271..1.825)	172	179	3 2 1 0
1.75	α^{ens}	16.561 (16.454..16.614)	1.631 (1.529..1.774)	1.772 (0.924..2.573)	171	181	4 2 1 0
	α^{typ}	16.526 (16.463..16.583)	1.642 (1.580..1.720)	1.409 (1.051..1.835)	171	166	3 2 2 0
	D^{ens}	16.531 (16.488..16.576)	1.611 (1.546..1.671)	1.514 (1.150..1.916)	172	186	3 2 1 0
	D^{typ}	16.520 (16.480..16.558)	1.628 (1.582..1.685)	1.454 (1.198..1.688)	172	174	3 2 1 0
2	α^{ens}	16.574 (16.372..16.624)	1.634 (1.535..1.883)	1.762 (0.567..3.029)	171	181	4 2 1 0
	α^{typ}	16.518 (16.463..16.571)	1.643 (1.582..1.695)	1.363 (1.081..1.768)	171	164	4 2 1 0
	D^{ens}	16.545 (16.500..16.592)	1.606 (1.548..1.686)	1.648 (1.212..2.273)	171	182	4 2 1 0
	D^{typ}	16.518 (16.473..16.551)	1.629 (1.573..1.682)	1.420 (1.167..1.696)	171	171	4 2 1 0

Table 4.2: Resulting parameters of the MFSS at fixed $\lambda = 0.1$ for the orthogonal class and parameters of the fit method. The results are visible in Figure 4.2.

q	exp	$W_c^{U\lambda}$	$\nu^{U\lambda}$	$y^{U\lambda}$	N_{df}	χ^2	$n_r n_{ir} n_\varrho n_\eta$
-1	α^{ens}	18.378 (18.348..18.398)	1.460 (1.431..1.494)	1.473 (1.282..1.591)	198	201	4 2 1 0
	α^{typ}	18.348 (18.334..18.361)	1.448 (1.433..1.461)	1.354 (1.290..1.427)	198	212	4 2 1 0
	D^{ens}	18.372 (18.359..18.384)	1.439 (1.413..1.459)	1.541 (1.433..1.654)	198	197	4 2 1 0
	D^{typ}	18.362 (18.350..18.375)	1.433 (1.419..1.449)	1.491 (1.409..1.578)	198	204	4 2 1 0
-0.75	α^{ens}	18.370 (18.353..18.387)	1.444 (1.419..1.477)	1.501 (1.371..1.619)	198	198	4 2 1 0
	α^{typ}	18.356 (18.342..18.368)	1.439 (1.423..1.457)	1.433 (1.356..1.508)	198	211	4 2 1 0
	D^{ens}	18.371 (18.356..18.386)	1.433 (1.416..1.452)	1.573 (1.460..1.679)	198	195	4 2 1 0
	D^{typ}	18.366 (18.355..18.379)	1.430 (1.415..1.444)	1.543 (1.457..1.639)	198	200	4 2 1 0
-0.5	α^{ens}	18.369 (18.355..18.386)	1.436 (1.415..1.457)	1.548 (1.440..1.681)	198	196	4 2 1 0
	α^{typ}	18.366 (18.356..18.378)	1.432 (1.418..1.447)	1.531 (1.464..1.614)	198	206	4 2 1 0
	D^{ens}	18.371 (18.360..18.382)	1.426 (1.412..1.443)	1.595 (1.504..1.692)	198	192	4 2 1 0
	D^{typ}	18.369 (18.358..18.378)	1.426 (1.408..1.443)	1.579 (1.496..1.656)	198	195	4 2 1 0
-0.25	α^{ens}	18.370 (18.358..18.383)	1.427 (1.410..1.444)	1.596 (1.479..1.699)	198	192	4 2 1 0
	α^{typ}	18.370 (18.357..18.383)	1.428 (1.411..1.443)	1.592 (1.497..1.679)	198	196	4 2 1 0
	D^{ens}	18.371 (18.358..18.383)	1.425 (1.410..1.442)	1.609 (1.507..1.722)	198	187	4 2 1 0
	D^{typ}	18.372 (18.360..18.383)	1.424 (1.409..1.440)	1.613 (1.516..1.726)	198	188	4 2 1 0
0	$\alpha^{ens/typ}$	18.373 (18.358..18.386)	1.424 (1.407..1.436)	1.633 (1.516..1.751)	198	179	4 2 1 0
0.1	D^{ens}	18.374 (18.361..18.388)	1.426 (1.409..1.445)	1.636 (1.521..1.763)	198	176	4 2 1 0
	D^{typ}	18.374 (18.362..18.387)	1.423 (1.407..1.440)	1.642 (1.514..1.774)	198	175	4 2 1 0
0.25	α^{ens}	18.375 (18.358..18.391)	1.427 (1.408..1.449)	1.639 (1.496..1.776)	198	159	4 2 1 0
	α^{typ}	18.377 (18.361..18.393)	1.425 (1.400..1.451)	1.653 (1.495..1.824)	198	159	4 2 1 0
	D^{ens}	18.374 (18.361..18.387)	1.421 (1.404..1.438)	1.633 (1.520..1.768)	198	170	4 2 1 0
	D^{typ}	18.375 (18.362..18.387)	1.423 (1.408..1.441)	1.649 (1.527..1.764)	198	169	4 2 1 0
0.5	D^{ens}	18.376 (18.360..18.391)	1.424 (1.406..1.441)	1.640 (1.476..1.777)	198	164	4 2 1 0
	D^{typ}	18.375 (18.360..18.393)	1.425 (1.405..1.447)	1.635 (1.468..1.821)	198	164	4 2 1 0
0.6	α^{ens}	18.375 (18.362..18.388)	1.441 (1.417..1.462)	1.680 (1.579..1.796)	197	204	4 3 1 0
	α^{typ}	18.373 (18.360..18.385)	1.442 (1.415..1.467)	1.660 (1.527..1.763)	197	215	4 3 1 0
0.75	α^{ens}	18.374 (18.362..18.387)	1.429 (1.411..1.448)	1.631 (1.510..1.749)	198	162	4 2 1 0
	α^{typ}	18.376 (18.363..18.390)	1.426 (1.407..1.448)	1.650 (1.521..1.807)	198	164	4 2 1 0
	D^{ens}	18.377 (18.362..18.390)	1.421 (1.398..1.446)	1.637 (1.497..1.785)	198	169	4 2 1 0
	D^{typ}	18.377 (18.360..18.395)	1.421 (1.397..1.445)	1.641 (1.485..1.804)	198	171	4 2 1 0
0.9	D^{ens}	18.375 (18.355..18.392)	1.425 (1.397..1.450)	1.610 (1.431..1.795)	198	174	4 2 1 0
	D^{typ}	18.378 (18.360..18.393)	1.422 (1.394..1.447)	1.634 (1.471..1.799)	198	176	4 2 1 0
1	$\alpha^{ens/typ}$	18.376 (18.352..18.396)	1.422 (1.396..1.447)	1.608 (1.372..1.825)	198	177	4 2 1 0
1.25	α^{ens}	18.372 (18.346..18.396)	1.428 (1.383..1.473)	1.535 (1.275..1.797)	198	168	4 2 1 0
	α^{typ}	18.370 (18.342..18.393)	1.430 (1.384..1.468)	1.497 (1.279..1.739)	198	166	4 2 1 0
	D^{ens}	18.376 (18.351..18.399)	1.425 (1.389..1.463)	1.577 (1.366..1.820)	198	173	4 2 1 0
	D^{typ}	18.374 (18.354..18.392)	1.428 (1.396..1.458)	1.547 (1.365..1.723)	198	170	4 2 1 0
1.5	α^{ens}	18.365 (18.322..18.399)	1.433 (1.363..1.500)	1.452 (1.085..1.781)	198	165	4 2 1 0
	α^{typ}	18.360 (18.331..18.384)	1.437 (1.393..1.480)	1.374 (1.150..1.599)	198	165	4 2 1 0
	D^{ens}	18.372 (18.343..18.394)	1.424 (1.388..1.469)	1.542 (1.311..1.761)	198	165	4 2 1 0
	D^{typ}	18.372 (18.344..18.395)	1.430 (1.403..1.460)	1.511 (1.274..1.714)	198	165	4 2 1 0
1.75	α^{ens}	18.359 (18.293..18.420)	1.448 (1.375..1.534)	1.430 (0.962..2.151)	198	171	4 2 1 0
	α^{typ}	18.354 (18.308..18.391)	1.439 (1.373..1.499)	1.303 (1.029..1.590)	197	171	4 3 1 0
	D^{ens}	18.366 (18.330..18.403)	1.426 (1.380..1.470)	1.482 (1.124..1.906)	198	162	4 2 1 0
	D^{typ}	18.366 (18.338..18.394)	1.435 (1.398..1.483)	1.436 (1.212..1.697)	198	163	4 2 1 0
2	α^{ens}	18.355 (18.271..18.407)	1.482 (1.382..1.565)	1.431 (0.756..2.069)	198	175	4 2 1 0
	α^{typ}	18.352 (18.297..18.389)	1.439 (1.371..1.494)	1.264 (0.947..1.530)	197	176	4 3 1 0
	D^{ens}	18.364 (18.322..18.393)	1.435 (1.379..1.495)	1.455 (1.052..1.788)	198	163	4 2 1 0
	D^{typ}	18.365 (18.337..18.391)	1.434 (1.387..1.478)	1.421 (1.152..1.644)	198	164	4 2 1 0

Table 4.3: Resulting parameters of the MFSS at fixed $\lambda = 0.1$ for the unitary class and parameters of the fit method. The results are visible in Figure 4.2.

q	exp	$W_c^{S\lambda}$	$\nu^{S\lambda}$	$y^{S\lambda}$	N_{df}	χ^2	$n_r n_{ir} n_\varrho n_\eta$
-1	α^{ens}	19.818 (19.709..19.899)	1.409 (1.184..1.674)	1.153 (0.650..1.693)	172	185	3 2 1 0
	α^{typ}	19.767 (19.717..19.806)	1.440 (1.347..1.555)	0.960 (0.813..1.103)	172	170	3 2 1 0
	D^{ens}	19.821 (19.771..19.858)	1.371 (1.273..1.474)	1.285 (1.029..1.558)	171	169	4 2 1 0
	D^{typ}	19.813 (19.781..19.844)	1.383 (1.301..1.470)	1.253 (1.112..1.427)	171	160	4 2 1 0
-0.75	α^{ens}	19.817 (19.765..19.861)	1.370 (1.257..1.491)	1.217 (0.924..1.531)	172	174	3 2 1 0
	α^{typ}	19.796 (19.760..19.833)	1.415 (1.339..1.502)	1.136 (1.008..1.295)	172	166	3 2 1 0
	D^{ens}	19.831 (19.797..19.863)	1.366 (1.289..1.447)	1.387 (1.175..1.610)	172	162	3 2 1 0
	D^{typ}	19.824 (19.795..19.852)	1.385 (1.328..1.462)	1.352 (1.195..1.521)	171	157	4 2 1 0
-0.5	α^{ens}	19.827 (19.790..19.858)	1.369 (1.272..1.459)	1.342 (1.138..1.548)	172	163	3 2 1 0
	α^{typ}	19.818 (19.789..19.843)	1.389 (1.327..1.472)	1.302 (1.165..1.466)	171	160	4 2 1 0
	D^{ens}	19.836 (19.796..19.866)	1.363 (1.280..1.426)	1.454 (1.178..1.729)	171	155	4 2 1 0
	D^{typ}	19.831 (19.806..19.855)	1.376 (1.318..1.449)	1.431 (1.249..1.596)	171	154	4 2 1 0
-0.25	α^{ens}	19.837 (19.806..19.865)	1.365 (1.290..1.437)	1.476 (1.240..1.704)	171	154	4 2 1 0
	α^{typ}	19.835 (19.808..19.866)	1.376 (1.304..1.445)	1.459 (1.264..1.687)	171	154	4 2 1 0
	D^{ens}	19.842 (19.817..19.865)	1.366 (1.294..1.461)	1.535 (1.364..1.772)	171	151	4 2 1 0
	D^{typ}	19.838 (19.812..19.869)	1.369 (1.305..1.430)	1.508 (1.309..1.743)	171	151	4 2 1 0
0	$\alpha^{ens/typ}$	19.845 (19.812..19.873)	1.364 (1.306..1.435)	1.580 (1.297..1.832)	171	149	4 2 1 0
0.1	D^{ens}	19.845 (19.816..19.869)	1.369 (1.299..1.458)	1.577 (1.341..1.797)	171	149	4 2 1 0
	D^{typ}	19.847 (19.805..19.875)	1.369 (1.285..1.475)	1.598 (1.277..1.876)	171	148	4 2 1 0
0.25	α^{ens}	19.849 (19.812..19.882)	1.388 (1.293..1.471)	1.630 (1.290..2.017)	171	150	4 2 1 0
	α^{typ}	19.848 (19.808..19.877)	1.375 (1.275..1.473)	1.626 (1.276..1.952)	171	146	4 2 1 0
	D^{ens}	19.846 (19.813..19.881)	1.376 (1.300..1.458)	1.603 (1.314..1.962)	171	149	4 2 1 0
	D^{typ}	19.846 (19.817..19.872)	1.367 (1.283..1.465)	1.588 (1.306..1.899)	171	147	4 2 1 0
0.5	D^{ens}	19.844 (19.791..19.880)	1.383 (1.310..1.468)	1.579 (1.202..1.910)	171	149	4 2 1 0
	D^{typ}	19.844 (19.807..19.881)	1.369 (1.281..1.453)	1.580 (1.249..1.993)	171	147	4 2 1 0
0.6	α^{ens}	19.850 (19.824..19.872)	1.358 (1.294..1.417)	1.651 (1.412..1.874)	171	155	4 2 1 0
	α^{typ}	19.852 (19.829..19.875)	1.352 (1.272..1.433)	1.676 (1.459..1.917)	171	154	4 2 1 0
0.75	α^{ens}	19.848 (19.811..19.877)	1.376 (1.301..1.459)	1.619 (1.337..1.874)	171	149	4 2 1 0
	α^{typ}	19.846 (19.807..19.879)	1.366 (1.266..1.447)	1.604 (1.286..1.949)	171	147	4 2 1 0
	D^{ens}	19.850 (19.812..19.887)	1.383 (1.287..1.472)	1.621 (1.297..2.010)	171	150	4 2 1 0
	D^{typ}	19.843 (19.795..19.881)	1.381 (1.282..1.483)	1.564 (1.188..1.988)	171	148	4 2 1 0
0.9	D^{ens}	19.839 (19.772..19.880)	1.394 (1.275..1.484)	1.523 (1.060..1.904)	171	150	4 2 1 0
	D^{typ}	19.842 (19.782..19.876)	1.385 (1.290..1.492)	1.550 (1.110..1.953)	171	149	4 2 1 0
1	$\alpha^{ens/typ}$	19.836 (19.790..19.880)	1.376 (1.248..1.499)	1.475 (1.100..1.891)	171	150	4 2 1 0
1.25	α^{ens}	19.825 (19.724..19.887)	1.383 (1.188..1.549)	1.417 (0.810..2.082)	171	151	4 2 1 0
	α^{typ}	19.843 (19.795..19.888)	1.411 (1.254..1.578)	1.501 (1.097..1.901)	171	155	4 2 1 0
	D^{ens}	19.828 (19.756..19.885)	1.400 (1.238..1.566)	1.407 (0.931..1.975)	171	151	4 2 1 0
	D^{typ}	19.833 (19.757..19.883)	1.412 (1.223..1.519)	1.456 (0.944..1.889)	171	153	4 2 1 0
1.5	α^{ens}	19.786 (19.597..19.893)	1.358 (0.914..1.748)	1.174 (0.331..2.282)	171	151	4 2 1 0
	α^{typ}	19.833 (19.765..19.890)	1.418 (1.281..1.568)	1.409 (0.962..1.871)	171	158	4 2 1 0
	D^{ens}	19.819 (19.732..19.872)	1.400 (1.197..1.561)	1.356 (0.762..1.934)	171	151	4 2 1 0
	D^{typ}	19.831 (19.745..19.887)	1.411 (1.267..1.550)	1.424 (0.890..1.918)	171	155	4 2 1 0
1.75	α^{ens}	19.756 (19.610..19.905)	1.428 (0.766..1.984)	1.054 (0.406..2.252)	170	151	4 2 2 0
	α^{typ}	19.826 (19.733..19.900)	1.432 (1.284..1.582)	1.341 (0.808..1.947)	172	161	3 2 1 0
	D^{ens}	19.778 (19.602..19.872)	1.514 (1.084..1.886)	1.146 (0.481..1.848)	170	150	4 2 2 0
	D^{typ}	19.829 (19.736..19.884)	1.407 (1.266..1.562)	1.388 (0.867..1.891)	172	158	3 2 1 0
2	α^{ens}	19.752 (19.568..19.898)	1.195 (0.591..2.195)	1.029 (0.223..2.544)	171	150	4 2 1 0
	α^{typ}	19.836 (19.760..19.912)	1.414 (1.247..1.614)	1.382 (0.896..2.041)	172	161	3 2 1 0
	D^{ens}	19.769 (19.631..19.872)	1.488 (1.022..1.746)	1.091 (0.526..1.932)	170	150	4 2 2 0
	D^{typ}	19.829 (19.763..19.893)	1.426 (1.258..1.570)	1.378 (0.947..1.896)	172	159	3 2 1 0

Table 4.4: Resulting parameters of the MFSS at fixed $\lambda = 0.1$ for the symplectic class and parameters of the fit method. The results are visible in Figure 4.2.

4.4 Results of the MFSS at varying λ

As mentioned in Section 2.3, GMFEs obtained by *typical* averaging are equal with *ensemble*-averaged GMFEs only in a range of q, $q_- < q < q_+$. Since we intend to compute the MFEs also, we restrict our analysis to *ensemble* averaged GMFEs, and drop the label *ens* from the notations.

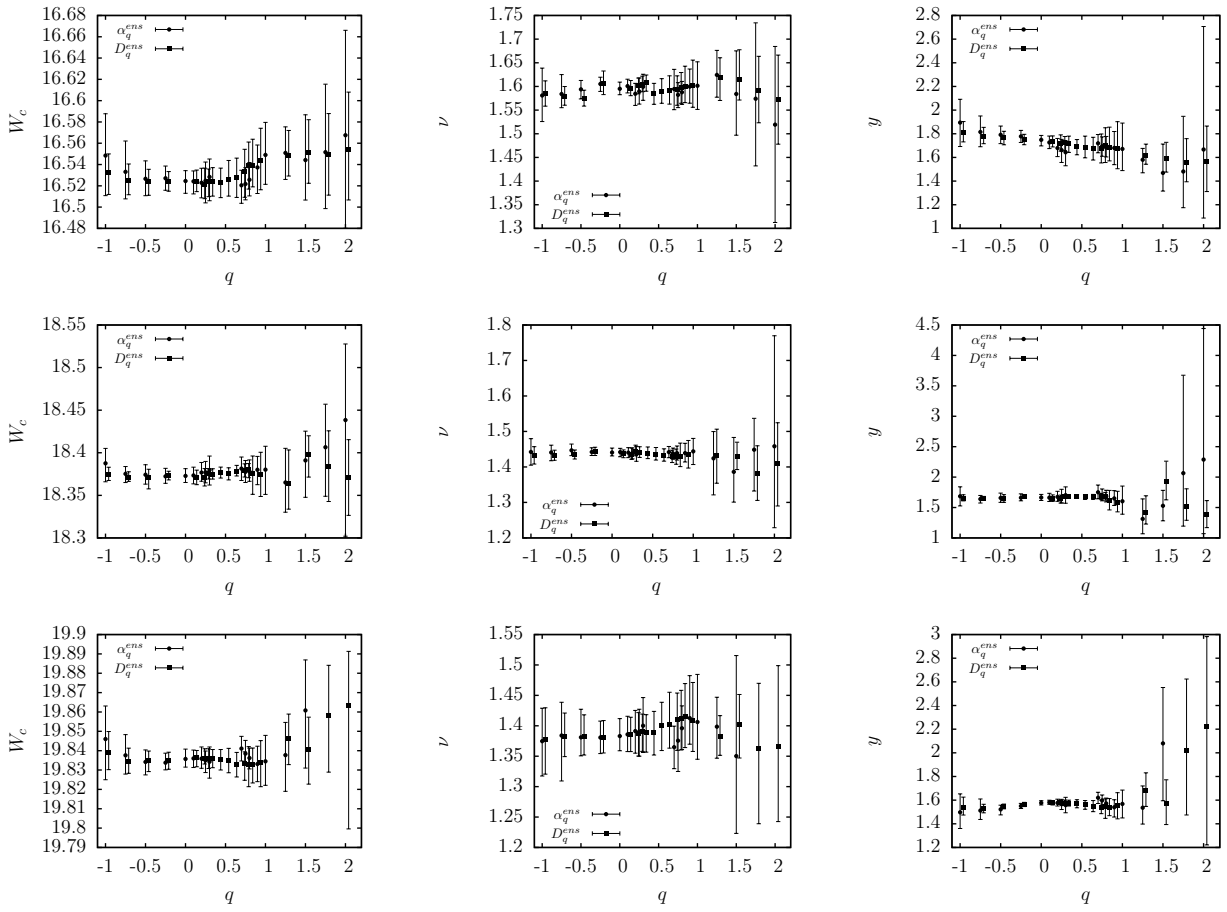

Figure 4.3: Critical parameters of the Anderson models in WD classes obtained by twovariable MFSS with varying λ. First row corresponds to the orthogonal class, second row corresponds to the unitary class, and third row corresponds to the symplectic class. The corresponding numerical values are listed in Table 4.6–4.8 alongside with the parameters of the fit method.

We fit the formula Eq. (3.19) to the raw data. To do that, we have to choose a range of box size ℓ, which is used for the MFSS. We always use the widest range of ℓ that results in convergence, $\chi^2/(N_{df}-1) \approx 1$. We find that for our dataset for different values of q for α_q or D_q different ranges of ℓ were the best. We use minimal box sizes $\ell_{min} = 2$ or $\ell_{min} = 3$ and maximal box sizes corresponding to $\lambda_{max} = 0.1$ or $\lambda_{max} = 0.066$. At $\alpha_{0.4}$ and $\alpha_{0.6}$ the fitting method sometimes suffered from convergence troubles and resulted in large error bars, because these points are close to the special case of $q = 0.5$ where by definition $\alpha_{0.5} = d$. Artifacts from this regime were also reported in Ref. [32], therefore

we decided not to take into account these points for α. We tried several combinations of ℓ_{min}, λ_{max} and expansion orders in the *symplectic* class for $\alpha_{1.75}$ and α_2, but none of them resulted in stable fit parameters. Therefore values computed from these points are also missing from our final results, which are listed in Tables 4.6–4.8, and visualized in Figure 4.3.

The results are independent of q and the GMFE we used, similar to the fixed λ method. In Section 4.3 we already saw that according to the arguments of Section 2.3 error bars get bigger, if q grows above 1. This phenomenon is more amplified here, especially for values coming from fits for α_q, but larger error bars on values corresponding to D_q are present on a moderate level also. Since Figure 8 of Ref. [32] shows results for this regime only for values corresponding to Δ_q, which is a linear transform of D_q, we can compare their results only to ours corresponding to D_q. One can see that our error bars are similar, even though there are differences probably due to the fact that they used system sizes up to $L = 120$, which was not possible for us, mainly because of the long runtime and large memory usage for the symplectic model. They also use $\ell_{min} = 1$ and $\ell_{min} = 2$, while $\ell_{min} = 1$ was never suitable for our dataset. We do not know the precise origin of this behavior, but we have a few possible explanations. We experience that larger system sizes allow a wider range of ℓ to be used. We have smaller system sizes than Ref. [32], and fewer samples for the largest systems sizes. Noise also gets bigger as ℓ decreases, because of the smoothing effect of boxing described in Section 3.2.5, which can also explain partly our experience. Another important difference is that in Eq. (37) of Ref. [32] the authors use an expression in the expansion of the scaling function, which is proportional to the square of the irrelevant term, $(\eta\ell^{-y})^2$. According to our experience the inclusion of this term produced no improvement in the scaling analysis, therefore we used the scaling function described in Eq. 3.19. Such a difference might be explained again by our different dataset.

As written in Section 4.3, the results for different values of q are strongly correlated, therefore we chose one of them with the lowest error bars that represents well the results for that universality class. The critical parameters listed in Table 4.5 are in a very nice agreement with our previous results for the fixed $\lambda = 0.1$ method, see Section 4.3, and also with the results of Refs. [32][38][39]. Comparing the critical parameters for the orthogonal case with the results of Rodriguez *et al.* [32] obtained by the same method, $W_{c\ Rod}^{O} = 16.530$ (16.524..16.536), $\nu_{Rod}^{O} = 1.590$ (1.579..1.602), we see a nice agreement again. Moreover these results are more accurate with this method compared to the fixed λ method, leading to (for y^O and y^U only almost) significantly different critical exponents and irrelevant exponents for the different WD classes, $\nu^O > \nu^U > \nu^S$ and $y^O \geq y^U > y^S$.

class	exp	W_c	ν	y
ort	$\tilde{\alpha}_0$	16.524 (16.513..16.534)	1.595 (1.582..1.609)	1.749 (1.697..1.786)
uni	$\tilde{D}_{0.1}$	18.371 (18.363..18.380)	1.437 (1.426..1.448)	1.651 (1.601..1.707)
sym	$\tilde{\alpha}_0$	19.836 (19.831..19.841)	1.383 (1.359..1.412)	1.577 (1.559..1.595)

Table 4.5: Critical parameters of the Anderson models in the WD symmetry classes obtained by two-variable MFSS with varying λ.

q	exp	W_c	ν	y	N_{df}	χ^2	$n_r n_{ir} n_\varrho n_\eta$
-1	α	16.548 (16.511..16.588)	1.581 (1.526..1.639)	1.894 (1.692..2.092)	239	246	4 1 1 0
	D	16.533 (16.512..16.550)	1.584 (1.558..1.612)	1.812 (1.731..1.903)	241	260	3 2 1 0
-0.75	α	16.533 (16.508..16.562)	1.584 (1.555..1.625)	1.815 (1.691..1.951)	241	262	3 2 1 0
	D	16.525 (16.512..16.541)	1.580 (1.560..1.600)	1.777 (1.716..1.854)	236	246	4 2 1 0
-0.5	α	16.527 (16.511..16.543)	1.594 (1.574..1.613)	1.791 (1.717..1.865)	271	274	3 2 1 0
	D	16.524 (16.511..16.535)	1.574 (1.558..1.592)	1.766 (1.707..1.821)	236	256	4 2 1 0
-0.25	α	16.527 (16.516..16.539)	1.605 (1.589..1.619)	1.778 (1.726..1.829)	240	250	3 2 2 0
	D	16.524 (16.515..16.533)	1.607 (1.583..1.633)	1.750 (1.707..1.795)	232	249	4 3 1 0
0	α	16.524 (16.513..16.534)	1.595 (1.582..1.609)	1.749 (1.697..1.786)	241	267	3 2 1 0
0.1	α	16.524 (16.512..16.534)	1.601 (1.586..1.615)	1.727 (1.675..1.781)	241	253	3 2 1 0
	D	16.524 (16.515..16.535)	1.597 (1.580..1.612)	1.739 (1.689..1.782)	241	260	3 2 1 0
0.2	α	16.523 (16.509..16.537)	1.585 (1.560..1.607)	1.679 (1.607..1.760)	236	204	4 2 1 0
	D	16.521 (16.508..16.537)	1.602 (1.584..1.618)	1.715 (1.653..1.791)	241	254	3 2 1 0
0.25	α	16.525 (16.504..16.542)	1.589 (1.563..1.618)	1.662 (1.557..1.753)	236	195	4 2 1 0
	D	16.524 (16.510..16.536)	1.604 (1.589..1.622)	1.723 (1.655..1.777)	241	252	3 2 1 0
0.3	α	16.528 (16.506..16.545)	1.599 (1.571..1.626)	1.644 (1.530..1.741)	236	187	4 2 1 0
	D	16.524 (16.510..16.537)	1.608 (1.590..1.624)	1.718 (1.643..1.780)	241	249	3 2 1 0
0.4	D	16.523 (16.509..16.537)	1.585 (1.562..1.607)	1.690 (1.622..1.751)	236	202	4 2 1 0
0.5	D	16.526 (16.510..16.544)	1.590 (1.564..1.617)	1.681 (1.596..1.780)	236	193	4 2 1 0
0.6	D	16.528 (16.509..16.546)	1.591 (1.563..1.622)	1.677 (1.578..1.770)	236	188	4 2 1 0
0.7	α	16.520 (16.504..16.535)	1.594 (1.551..1.636)	1.720 (1.639..1.794)	232	235	4 3 1 0
	D	16.533 (16.509..16.554)	1.594 (1.560..1.623)	1.677 (1.553..1.798)	236	189	4 2 1 0
0.75	α	16.522 (16.507..16.537)	1.582 (1.555..1.608)	1.694 (1.610..1.774)	236	233	4 2 1 0
	D	16.539 (16.517..16.561)	1.599 (1.564..1.629)	1.701 (1.557..1.851)	236	192	4 2 1 0
0.8	α	16.526 (16.511..16.542)	1.588 (1.562..1.611)	1.683 (1.604..1.777)	236	201	4 2 1 0
	D	16.539 (16.519..16.564)	1.601 (1.566..1.643)	1.683 (1.571..1.856)	236	195	4 2 1 0
0.9	α	16.537 (16.513..16.558)	1.600 (1.565..1.637)	1.680 (1.539..1.819)	236	192	4 2 1 0
	D	16.544 (16.516..16.574)	1.603 (1.556..1.656)	1.679 (1.504..1.902)	236	203	4 2 1 0
1	α	16.549 (16.521..16.580)	1.602 (1.551..1.652)	1.672 (1.488..1.890)	236	212	4 2 1 0
1.25	α	16.551 (16.526..16.575)	1.624 (1.577..1.676)	1.580 (1.470..1.676)	361	398	3 2 1 0
	D	16.548 (16.529..16.572)	1.619 (1.570..1.661)	1.618 (1.542..1.712)	361	387	4 2 1 0
1.5	α	16.544 (16.507..16.587)	1.584 (1.497..1.675)	1.469 (1.316..1.713)	356	393	3 2 1 0
	D	16.551 (16.522..16.582)	1.615 (1.571..1.677)	1.587 (1.476..1.728)	361	393	3 2 1 0
1.75	α	16.552 (16.499..16.616)	1.574 (1.432..1.734)	1.481 (1.175..1.948)	361	383	3 2 1 0
	D	16.549 (16.511..16.588)	1.592 (1.523..1.664)	1.554 (1.394..1.758)	361	386	3 2 1 0
2	α	16.568 (16.480..16.666)	1.519 (1.313..1.685)	1.667 (1.087..2.707)	361	375	3 2 1 0
	D	16.554 (16.507..16.608)	1.573 (1.478..1.666)	1.562 (1.311..1.865)	361	380	3 2 1 0

Table 4.6: Resulting parameters of the MFSS at varying λ for the orthogonal class and parameters of the fit method. The results are visible in Figure 4.3.

q	exp	W_c	ν	y	N_{df}	χ^2	$n_r n_{ir} n_\varrho n_\eta$
-1	α	18.388 (18.366..18.405)	1.442 (1.405..1.480)	1.684 (1.526..1.841)	418	476	3 2 1 0
	D	18.375 (18.367..18.383)	1.431 (1.408..1.457)	1.651 (1.608..1.710)	413	390	4 2 1 0
-0.75	α	18.375 (18.365..18.384)	1.441 (1.418..1.461)	1.638 (1.574..1.698)	413	427	4 2 1 0
	D	18.372 (18.366..18.378)	1.432 (1.419..1.447)	1.651 (1.623..1.682)	413	383	4 2 1 0
-0.5	α	18.374 (18.363..18.386)	1.447 (1.432..1.465)	1.658 (1.585..1.737)	275	275	4 2 1 0
	D	18.371 (18.358..18.381)	1.435 (1.422..1.448)	1.651 (1.585..1.711)	275	219	4 2 1 0
-0.25	α	18.372 (18.364..18.382)	1.442 (1.432..1.454)	1.661 (1.610..1.725)	275	287	4 2 1 0
	D	18.373 (18.368..18.378)	1.444 (1.432..1.456)	1.675 (1.660..1.691)	413	420	4 2 1 0
0	α	18.373 (18.365..18.381)	1.441 (1.431..1.453)	1.665 (1.616..1.715)	275	289	4 2 1 0
0.1	α	18.373 (18.363..18.383)	1.442 (1.429..1.452)	1.663 (1.600..1.734)	275	290	4 2 1 0
	D	18.371 (18.363..18.380)	1.437 (1.426..1.448)	1.651 (1.601..1.707)	275	232	4 2 1 0
0.2	α	18.377 (18.367..18.389)	1.440 (1.426..1.454)	1.675 (1.602..1.767)	275	282	4 2 1 0
	D	18.371 (18.361..18.381)	1.436 (1.421..1.453)	1.646 (1.573..1.705)	275	235	4 2 1 0
0.25	α	18.377 (18.365..18.390)	1.438 (1.423..1.454)	1.668 (1.576..1.799)	275	272	4 2 1 0
	D	18.375 (18.369..18.381)	1.444 (1.432..1.461)	1.681 (1.661..1.702)	413	423	4 2 1 0
0.3	α	18.380 (18.362..18.396)	1.436 (1.416..1.458)	1.703 (1.571..1.838)	278	286	4 1 1 0
	D	18.375 (18.369..18.381)	1.442 (1.427..1.457)	1.678 (1.654..1.701)	413	424	4 2 1 0
0.4	D	18.376 (18.370..18.383)	1.438 (1.424..1.456)	1.681 (1.655..1.710)	413	423	4 2 1 0
0.5	D	18.376 (18.368..18.382)	1.436 (1.419..1.455)	1.674 (1.633..1.707)	413	419	4 2 1 0
0.6	D	18.378 (18.373..18.385)	1.433 (1.416..1.451)	1.681 (1.634..1.715)	413	415	4 2 1 0
0.7	α	18.381 (18.367..18.395)	1.442 (1.426..1.458)	1.750 (1.643..1.870)	275	261	4 2 1 0
	D	18.379 (18.372..18.387)	1.430 (1.412..1.447)	1.682 (1.629..1.732)	413	414	4 2 1 0
0.75	α	18.378 (18.365..18.391)	1.438 (1.422..1.453)	1.700 (1.610..1.805)	275	278	4 2 1 0
	D	18.380 (18.371..18.387)	1.429 (1.408..1.450)	1.688 (1.621..1.749)	413	413	4 2 1 0
0.8	α	18.378 (18.366..18.392)	1.439 (1.420..1.459)	1.684 (1.592..1.783)	275	277	4 2 1 0
	D	18.375 (18.351..18.396)	1.430 (1.401..1.467)	1.618 (1.460..1.782)	414	414	4 2 1 0
0.9	α	18.380 (18.363..18.396)	1.439 (1.414..1.467)	1.650 (1.534..1.777)	275	253	4 2 1 0
	D	18.375 (18.349..18.401)	1.435 (1.397..1.475)	1.587 (1.428..1.767)	275	203	4 2 1 0
1	α	18.380 (18.351..18.408)	1.444 (1.407..1.481)	1.603 (1.390..1.852)	275	251	4 2 1 0
1.25	α	18.365 (18.330..18.405)	1.424 (1.321..1.500)	1.313 (1.068..1.642)	275	248	4 2 1 0
	D	18.363 (18.334..18.403)	1.433 (1.354..1.506)	1.413 (1.227..1.692)	275	203	4 2 1 0
1.5	α	18.391 (18.348..18.425)	1.386 (1.301..1.483)	1.529 (1.282..1.782)	386	392	4 3 1 0
	D	18.398 (18.371..18.420)	1.430 (1.393..1.470)	1.923 (1.625..2.262)	413	395	4 2 1 0
1.75	α	18.407 (18.349..18.457)	1.449 (1.332..1.537)	2.064 (1.194..3.674)	417	450	3 2 2 0
	D	18.384 (18.343..18.426)	1.382 (1.306..1.460)	1.522 (1.290..1.808)	390	360	4 2 1 0
2	α	18.438 (18.302..18.528)	1.458 (1.229..1.770)	2.288 (1.071..4.442)	420	454	3 1 2 0
	D	18.370 (18.326..18.415)	1.409 (1.290..1.525)	1.390 (1.169..1.613)	395	392	3 2 1 0

Table 4.7: Resulting parameters of the MFSS at varying λ for the unitary class and parameters of the fit method. The results are visible in Figure 4.3.

q	exp	W_c	ν	y	N_{df}	χ^2	$n_r n_{ir} n_\varrho n_\eta$
-1	α	19.848 (19.821..19.870)	1.370 (1.230..1.508)	1.518 (1.318..1.694)	356	385	4 2 1 0
	D	19.839 (19.830..19.850)	1.377 (1.321..1.430)	1.541 (1.474..1.626)	361	384	3 2 1 0
-0.75	α	19.838 (19.828..19.848)	1.384 (1.309..1.439)	1.512 (1.437..1.610)	356	384	4 2 1 0
	D	19.835 (19.828..19.841)	1.383 (1.349..1.421)	1.531 (1.492..1.565)	361	372	3 2 1 0
-0.5	α	19.834 (19.828..19.840)	1.381 (1.351..1.427)	1.522 (1.475..1.558)	356	365	4 2 1 0
	D	19.835 (19.829..19.840)	1.383 (1.352..1.418)	1.549 (1.527..1.567)	361	348	3 2 1 0
-0.25	α	19.834 (19.830..19.839)	1.381 (1.354..1.408)	1.551 (1.530..1.572)	361	345	3 2 1 0
	D	19.835 (19.830..19.839)	1.381 (1.355..1.409)	1.565 (1.546..1.582)	361	335	3 2 1 0
0	α	19.836 (19.831..19.841)	1.383 (1.359..1.412)	1.577 (1.559..1.595)	361	352	3 2 1 0
0.1	α	19.836 (19.831..19.840)	1.386 (1.358..1.416)	1.581 (1.565..1.599)	361	372	3 2 1 0
	D	19.836 (19.832..19.840)	1.385 (1.358..1.414)	1.580 (1.559..1.597)	361	358	3 2 1 0
0.2	α	19.836 (19.831..19.842)	1.391 (1.355..1.425)	1.577 (1.550..1.608)	361	375	3 2 1 0
	D	19.836 (19.833..19.841)	1.387 (1.350..1.422)	1.578 (1.561..1.601)	361	368	3 2 1 0
0.25	α	19.835 (19.829..19.840)	1.390 (1.350..1.427)	1.565 (1.520..1.607)	361	370	3 2 1 0
	D	19.836 (19.831..19.841)	1.391 (1.358..1.419)	1.576 (1.555..1.601)	356	368	4 2 1 0
0.3	α	19.834 (19.826..19.842)	1.400 (1.356..1.446)	1.558 (1.493..1.624)	361	366	3 2 1 0
	D	19.836 (19.831..19.841)	1.388 (1.357..1.418)	1.575 (1.551..1.600)	361	371	3 2 1 0
0.4	D	19.835 (19.830..19.841)	1.389 (1.352..1.424)	1.571 (1.535..1.604)	361	369	3 2 1 0
0.5	D	19.835 (19.829..19.841)	1.400 (1.359..1.439)	1.560 (1.523..1.596)	361	366	3 2 1 0
0.6	D	19.833 (19.826..19.839)	1.403 (1.363..1.455)	1.546 (1.503..1.596)	361	365	3 2 1 0
0.7	α	19.841 (19.835..19.847)	1.365 (1.329..1.399)	1.620 (1.572..1.667)	356	359	4 2 1 0
	D	19.833 (19.825..19.839)	1.410 (1.360..1.454)	1.542 (1.486..1.600)	361	367	3 2 1 0
0.75	α	19.838 (19.833..19.845)	1.376 (1.325..1.413)	1.598 (1.558..1.644)	356	364	4 2 1 0
	D	19.833 (19.821..19.842)	1.411 (1.360..1.458)	1.542 (1.446..1.610)	361	369	3 2 1 0
0.8	α	19.836 (19.831..19.841)	1.396 (1.361..1.433)	1.572 (1.536..1.617)	356	363	3 2 1 0
	D	19.833 (19.823..19.841)	1.415 (1.364..1.469)	1.540 (1.469..1.614)	413	371	3 2 1 0
0.9	α	19.833 (19.824..19.842)	1.413 (1.370..1.482)	1.540 (1.457..1.603)	356	363	3 2 1 0
	D	19.834 (19.821..19.845)	1.409 (1.358..1.471)	1.554 (1.442..1.663)	361	374	3 2 1 0
1	α	19.834 (19.822..19.848)	1.406 (1.345..1.484)	1.568 (1.449..1.685)	361	381	3 2 1 0
1.25	α	19.838 (19.819..19.855)	1.399 (1.347..1.447)	1.536 (1.398..1.720)	361	369	3 2 1 0
	D	19.846 (19.833..19.859)	1.382 (1.351..1.417)	1.683 (1.547..1.831)	361	373	3 2 1 0
1.5	α	19.861 (19.831..19.887)	1.350 (1.223..1.515)	2.080 (1.595..2.552)	361	356	3 2 1 0
	D	19.841 (19.823..19.857)	1.402 (1.347..1.452)	1.573 (1.393..1.772)	361	363	3 2 1 0
1.75	α	no stability					
	D	19.858 (19.829..19.884)	1.364 (1.239..1.470)	2.016 (1.475..2.624)	361	355	3 2 1 0
2	α	no stability					
	D	19.864 (19.800..19.891)	1.365 (1.243..1.499)	2.223 (1.222..2.982)	361	352	3 2 1 0

Table 4.8: Resulting parameters of the MFSS at varying λ for the symplectic class and parameters of the fit method. The results are visible in Figure 4.3.

4.5 Analysis of the multifractal exponents

MFSS for varying λ provided us the MFEs in all WD classes, which are listed in Table 4.10, and depicted in Figure 4.4. For the orthogonal class one can find matching results with the listed MFE-s in Ref. [32]. Since the precise values of the MFEs in three dimensions were determined first in Ref. [32] for the orthogonal class only, the lack of reliable analytical and numerical results for the other symmetry classes makes our results more important. The most conspicuous thing in Figure 4.4 is that curves for different symmetry classes are very close to each other, they are almost indistinguishable at first sight. This shows that the broken time-reversal or spin rotational symmetry has a very small effect on the

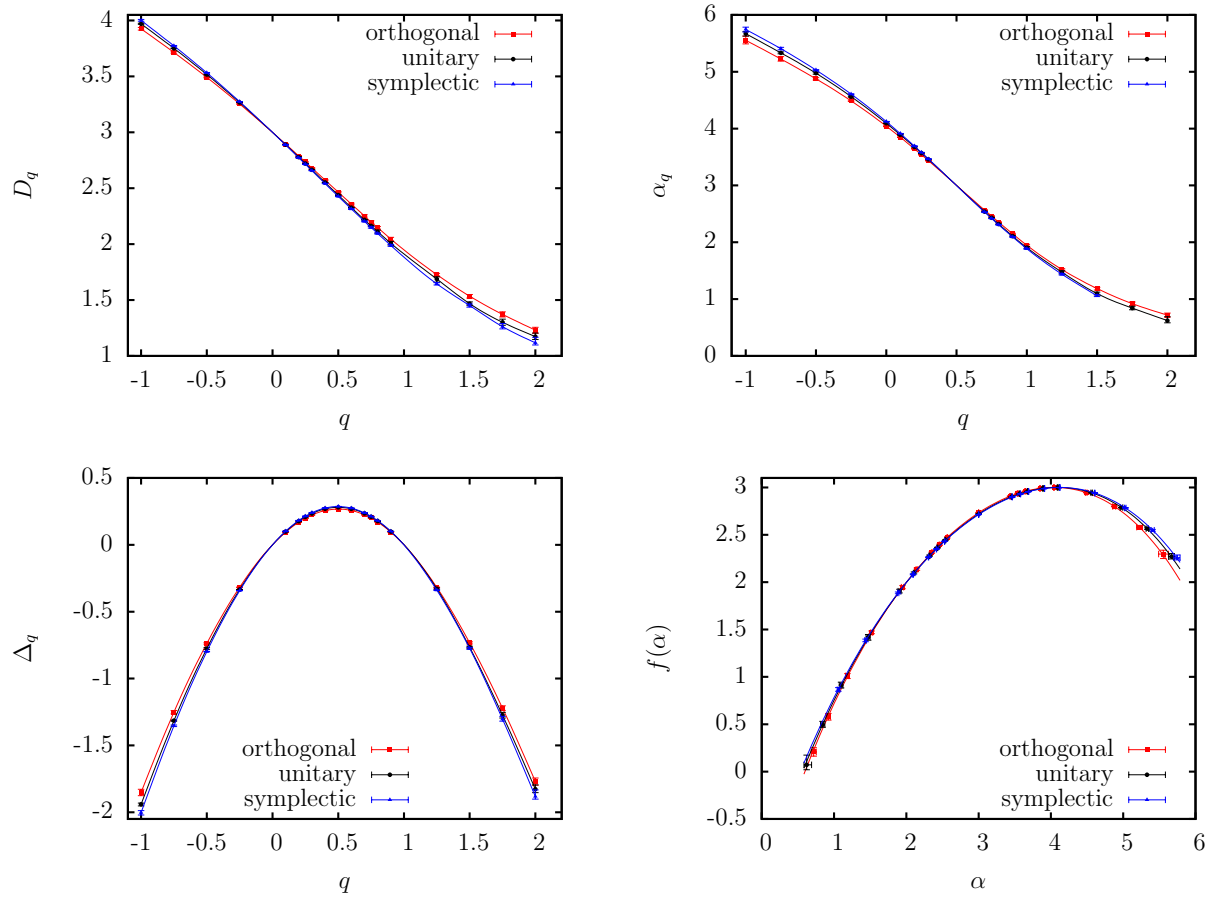

Figure 4.4: MFEs of the Anderson models in the WD universality classes. Corresponding data are listed in Table 4.10.

MFEs in three dimensions. Taking a closer look (or from Table 4.10) one can see that curve of D_q and α_q is the steepest in the symplectic class, the second steepest in the unitary class, and the less steep in the orthogonal class. From Table 4.10 it is also clear that at most of the q values there is a significant difference between the MFEs of different symmetry classes.

There are no critical states in the two dimensional orthogonal class [5], but one can find values of α_0 for the two dimensional unitary class (Integer Quantum Hall), $\alpha^U_{0\,2D} = 2.2596 \pm 0.0004$ [29], and symplectic class, $\alpha^S_{0\,2D} = 2.172 \pm 0.002$ [28]. Comparing the difference between these exponents in two dimensions we get $\alpha^U_{0\,2D} - \alpha^S_{0\,2D} = 0.0876 \pm 0.0024$, while our result for three dimensions is $\alpha^U_{0\,3D} - \alpha^S_{0\,3D} = -0.03 \pm 0.015$. There is about a factor of 3 between the magnitude of these values, and even their sign is opposite, which shows very different effect of presence or absence of spin rotational symmetry in different dimensions.

We tested the symmetry relation Eq. (2.12) for α_q and Δ_q, the results are listed in Table 4.10 and depicted in Figure 4.5. The symmetry relation is fulfilled in the range $-0.25 \leq q \leq 1.25$ (in the *symplectic* class only for $-0.25 \leq q \leq 1$), and small deviations are visible outside this interval. In this regime error bars are growing very large, coming

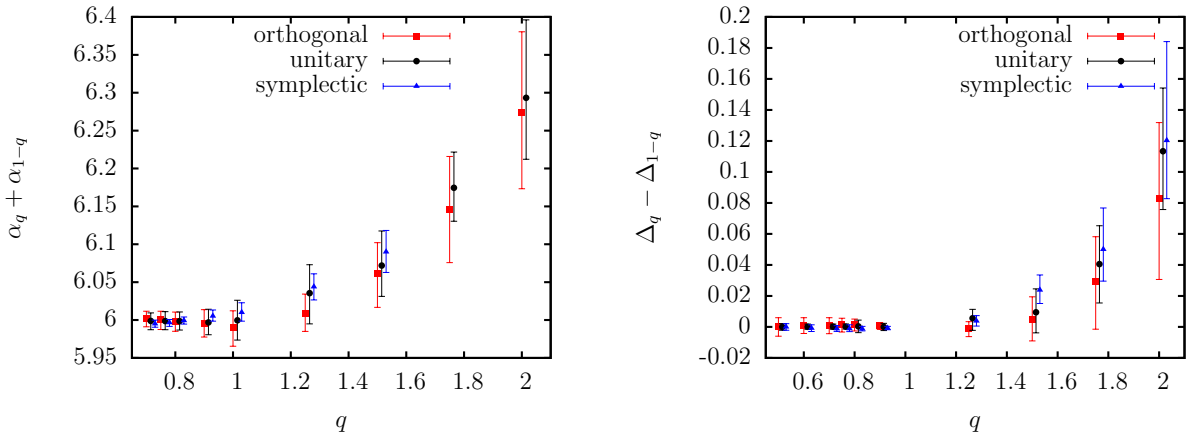

Figure 4.5: Test for symmetry relation Eq. (2.12) in the WD symmetry classes. Points are shifted horizontally a little bit for better visualization. Only the $q \geq 0.5$ range is visible because expression $\alpha_q + \alpha_{1-q}$ ($\Delta_q - \Delta_{1-q}$) is symmetric (antisymmetric) to $q = 0.5$.

mainly from the large errors of $\alpha_{q\geq 1.5}$ and $D_{q\geq 1.5}$. Similar effects were already seen for the critical parameters in Figure 4.3. It is really hard to estimate the correct error bars in this large q case, and the deviation from the symmetry are small, therefore we believe that differences appear only because of slightly underestimated error bars of $\alpha_{q\geq 1.5}$ and $D_{q\geq 1.5}$. All in all we find numerical results basically matching Eq. (2.12).

Assuming that Δ_q is an analytic function of q, and using the symmetry relation, Eq. (2.12), one can expand Δ_q in Taylor series around $q = \frac{1}{2}$:

$$\begin{aligned} \Delta_q &= \sum_{k=0}^{\infty} c_k \left(q - \frac{1}{2}\right)^{2k} = \sum_{k=0}^{\infty} c_k \left(q(q-1) + \frac{1}{4}\right)^{k} = \\ &= \sum_{k=0}^{\infty} c_k \sum_{i=0}^{k} \binom{k}{i} \left(q(q-1)\right)^{i} \left(\frac{1}{4}\right)^{k-i} = \sum_{k=1}^{\infty} d_k \left(q(1-q)\right)^{k}, \end{aligned} \tag{4.6}$$

where the condition $\Delta_0 = \Delta_1 = 0$ enforced by the definition of Δ_q (see Eq. (2.8)) was used in the last step, leading to $k = 1$ as lower bound for the summation. Similar expression can be derived for α_q by using the connection $\alpha_q = d + \frac{d}{dq}\Delta_q$ derived from Eqs. (2.7)–(2.8):

$$\alpha_q = d + (1-2q) \sum_{k=1}^{\infty} a_k \left(q(1-q)\right)^{k-1}, \tag{4.7}$$

where $a_k = k d_k$, and $a_1 = d_1 = \alpha_0 - d$. One can obtain the d_k and a_k coefficients by fitting the expressions Eqs. (4.6)–(4.7). We used only the range $q \leq 1.25$, because beyond this regime error bars grow extremely large, and moreover there are small deviations from the symmetry relation Eq.(2.12) also. We plotted $\frac{\Delta(q)}{q(1-q)}$ and $\frac{\alpha(q)-d}{1-2q}$ in Figure 4.6 to make the presence of higher-order terms of the expansion visible.

We fit expressions Eq. (4.6)–(4.7)up to third order in all cases, the resulting expansion coefficients are listed in Table 4.9. From the listed data one can see that the expansion

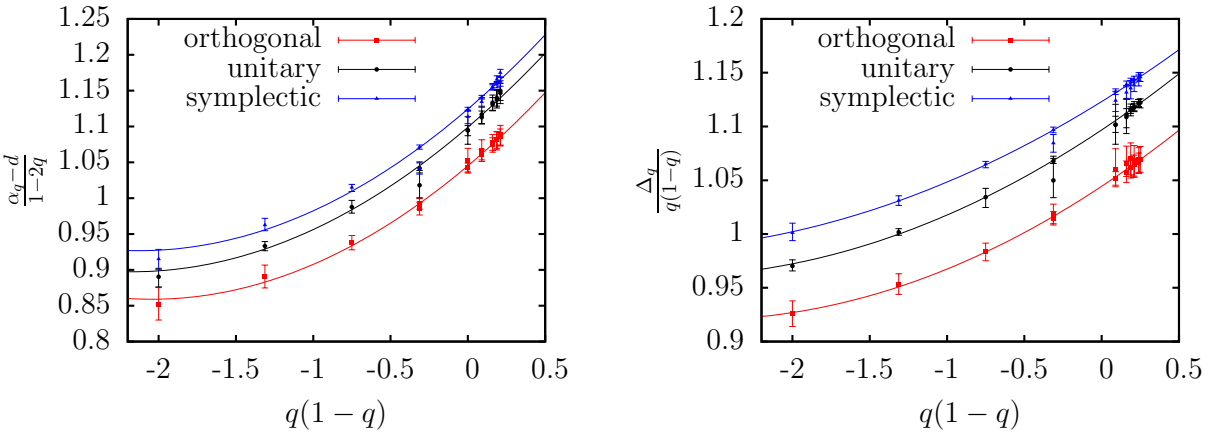

Figure 4.6: Dots and error bars are numerical values for the corresponding quantities, $\frac{\alpha(q)-d}{1-2q}$ and $\frac{\Delta(q)}{q(1-q)}$, for the WD symmetry classes. Lines are the best fits. Several points are shifted horizontally a bit for better viewing.

class	ort	uni	sym
d_1	1.044 (1.041..1.047)	1.097 (1.095..1.098)	1.123 (1.122..1.125)
d_2	0.095 (0.085..0.105)	0.096 (0.091..0.100)	0.088 (0.084..0.093)
d_3	0.018 (0.011..0.025)	0.017 (0.014..0.020)	0.014 (0.010..0.017)
a_1	1.045 (1.042..1.048)	1.099 (1.096..1.102)	1.124 (1.123..1.126)
a_2	0.182 (0.168..0.195)	0.185 (0.174..0.197)	0.185 (0.179..0.191)
a_3	0.044 (0.035..0.053)	0.043 (0.035..0.050)	0.044 (0.038..0.049)

Table 4.9: Expansion coefficients of Eqs. (4.6)–(4.7) obtained by a fit depicted in Figure 4.6.

coefficients fulfill the relation $a_k = kd_k$. However, α_q and Δ_q were obtained from the same wave-functions, they are results of completely independent fit-procedures. Therefore the fact that they satisfy the equation $a_k = kd_k$ further confirms our result for their value listed in Table 4.10 for $q \leq 1.25$ and shows the consistency of the MFSS.

As one would expect for expansion coefficients, d_k and a_k show decreasing behavior as k grows. Only d_1 and a_1 are significantly different for the different symmetry classes, while d_2, d_3, a_2, and a_3 are the same within error bars. Their real value is probably different, but the relative error of the expansion coefficients naturally increases as k grows, leading to indistinguishable values for the different symmetry classes for $k \geq 2$.

Wegner computed analytically [43] the value of Δ_q with ε expansion using nonlinear σ-model up to fourth-loop order for the orthogonal and the unitary symmetry class,

resulting an expansion in dimensions $d = 2 + \varepsilon$ for $\varepsilon \ll 1$ [5]:

$$\Delta_q^O = q(1-q)\varepsilon + \frac{\zeta(3)}{4} q(q-1)(q^2-q+1)\varepsilon^4 + \mathcal{O}(\varepsilon^5) \tag{4.8}$$

$$= \left(\varepsilon - \frac{\zeta(3)}{4}\varepsilon^4\right) q(1-q) + \frac{\zeta(3)}{4}\varepsilon^4 (q(1-q))^2 + \mathcal{O}(\varepsilon^5) \tag{4.9}$$

$$\Delta_q^U = \sqrt{\frac{\varepsilon}{2}} q(1-q) - \frac{3}{8}\zeta(3)\varepsilon^2 (q(1-q))^2 + \mathcal{O}(\varepsilon^{\frac{5}{2}}) \tag{4.10}$$

Even though $\varepsilon \ll 1$ should hold, one can try to extrapolate to three-dimensions by inserting $\varepsilon = 1$. This leads to $d_1^O \approx 0.699$, $d_2^O \approx 0.301$, $d_1^U \approx 0.707$ and $d_2^U \approx -0.451$. As one can see, these values are rather far from our numerical results, but this is not surprising for an ε-expansion at $\varepsilon = 1$. These results capture well the tendency at least that d_1^O is slightly smaller, than d_1^U. On the other hand it leads to d_2^O and d_2^U having opposite sign, which is highly inconsistent with our numerical results. It is interesting to mention that the first-loop term, which is proportional to ε and leads to parabolic Δ_q, results in $d_1^O = 1$ and $a_1^O = \alpha_0 - d = 1$, which are very close to our numerically measured values. In this sense parabolic approximation is better for the orthogonal class, as compared to the fourth-loop order approximation. If higher-order terms were obtained, or if Δ_q were expanded by using another approach, our coefficients could provide relatively accurate values as compared with analytical results.

q	class	α_q	D_q	$f(\alpha_q)$	$\alpha_q+\alpha_{1-q}$	$\Delta_q-\Delta_{1-q}$
	ort	5.555 (5.490..5.626)	3.926 (3.914..3.938)	2.297 (2.338..2.250)	6.275 (6.042..6.661)	−0.102 (−0.218..0.000)
−1	uni	5.671 (5.629..5.707)	3.970 (3.966..3.976)	2.269 (2.303..2.245)	6.331 (6.215..6.444)	−0.130 (−0.195..−0.062)
	sym	5.751 (5.690..5.799)	4.001 (3.994..4.010)	2.251 (2.298..2.222)	6.379 (6.197..6.584)	−0.134 (−0.237..−0.063)
	ort	5.225 (5.187..5.267)	3.715 (3.708..3.722)	2.582 (2.599..2.564)	6.153 (5.988..6.353)	−0.035 (−0.094..0.032)
−0.75	uni	5.333 (5.317..5.349)	3.751 (3.749..3.754)	2.565 (2.573..2.557)	6.176 (6.131..6.239)	−0.062 (−0.098..−0.025)
	sym	5.406 (5.387..5.430)	3.773 (3.770..3.777)	2.549 (2.558..2.537)	6.221 (6.113..6.349)	−0.060 (−0.114..−0.023)
	ort	4.876 (4.856..4.896)	3.492 (3.488..3.496)	2.800 (2.803..2.796)	6.061 (5.959..6.149)	−0.008 (−0.045..0.025)
−0.5	uni	4.975 (4.958..4.994)	3.517 (3.512..3.521)	2.788 (2.789..2.785)	6.103 (6.000..6.167)	−0.009 (−0.025..0.004)
	sym	5.030 (5.019..5.039)	3.532 (3.531..3.534)	2.784 (2.787..2.781)	6.103 (6.039..6.206)	−0.019 (−0.041..−0.001)
	ort	4.488 (4.477..4.499)	3.254 (3.252..3.255)	2.945 (2.946..2.944)	6.016 (5.951..6.094)	0.000 (−0.012..0.010)
−0.25	uni	4.563 (4.553..4.574)	3.267 (3.266..3.268)	2.943 (2.945..2.941)	6.037 (5.998..6.081)	−0.006 (−0.011..0.002)
	sym	4.607 (4.603..4.611)	3.274 (3.274..3.275)	2.941 (2.941..2.941)	6.033 (5.997..6.072)	−0.004 (−0.011..0.003)
	ort	4.043 (4.035..4.049)	3 (3..3)	3 (3..3)	5.991 (5.965..6.012)	0 (0..0)
0	uni	4.094 (4.087..4.101)	3 (3..3)	3 (3..3)	6.000 (5.974..6.026)	0 (0..0)
	sym	4.124 (4.121..4.127)	3 (3..3)	3 (3..3)	6.010 (5.999..6.023)	0 (0..0)
	ort	3.849 (3.843..3.855)	2.895 (2.894..2.895)	2.990 (2.989..2.991)	5.995 (5.978..6.014)	−0.001 (−0.003..0.002)
0.1	uni	3.890 (3.883..3.897)	2.890 (2.889..2.891)	2.990 (2.988..2.991)	5.997 (5.981..6.014)	0.000 (−0.002..0.002)
	sym	3.913 (3.911..3.915)	2.887 (2.886..2.887)	2.989 (2.989..2.990)	6.005 (5.998..6.013)	0.001 (−0.000..0.002)
	ort	3.645 (3.638..3.651)	2.789 (2.786..2.790)	2.960 (2.957..2.962)	5.998 (5.985..6.011)	−0.001 (−0.005..0.003)
0.2	uni	3.678 (3.673..3.684)	2.778 (2.777..2.780)	2.958 (2.956..2.961)	5.999 (5.987..6.011)	−0.000 (−0.004..0.004)
	sym	3.693 (3.691..3.695)	2.772 (2.772..2.773)	2.956 (2.955..2.957)	5.999 (5.995..6.004)	0.001 (−0.000..0.003)
	ort	3.541 (3.534..3.547)	2.734 (2.733..2.737)	2.936 (2.933..2.939)	6.000 (5.987..6.012)	−0.001 (−0.006..0.003)
0.25	uni	3.569 (3.563..3.575)	2.721 (2.720..2.722)	2.933 (2.931..2.935)	5.999 (5.987..6.011)	−0.000 (−0.002..0.001)
	sym	3.579 (3.577..3.581)	2.715 (2.714..2.715)	2.931 (2.930..2.932)	5.997 (5.992..6.001)	0.001 (−0.001..0.003)
	ort	3.436 (3.430..3.441)	2.681 (2.678..2.684)	2.907 (2.903..2.911)	6.001 (5.991..6.012)	−0.001 (−0.006..0.004)
0.3	uni	3.459 (3.453..3.464)	2.665 (2.664..2.666)	2.903 (2.900..2.905)	5.999 (5.987..6.010)	−0.000 (−0.002..0.001)
	sym	3.465 (3.462..3.467)	2.657 (2.656..2.658)	2.899 (2.898..2.901)	5.995 (5.991..6.000)	0.001 (−0.001..0.003)
	ort	–	2.573 (2.570..2.577)	–	–	−0.001 (−0.006..0.004)
0.4	uni	–	2.551 (2.550..2.553)	–	–	−0.000 (−0.002..0.002)
	sym	–	2.542 (2.540..2.543)	–	–	0.001 (−0.001..0.003)
	ort	3 (3..3)	2.466 (2.459..2.471)	2.733 (2.730..2.736)	6 (6..6)	0 (0..0)
0.5	uni	3 (3..3)	2.439 (2.437..2.441)	2.719 (2.719..2.721)	6 (6..6)	0 (0..0)
	sym	3 (3..3)	2.427 (2.425..2.429)	2.714 (2.712..2.715)	6 (6..6)	0 (0..0)
	ort	–	2.358 (2.352..2.366)	–	–	0.001 (−0.004..0.006)
0.6	uni	–	2.327 (2.325..2.329)	–	–	0.000 (−0.002..0.002)
	sym	–	2.314 (2.311..2.317)	–	–	−0.001 (−0.003..0.001)
	ort	2.566 (2.561..2.571)	2.252 (2.242..2.263)	2.472 (2.466..2.479)	6.001 (5.991..6.012)	0.001 (−0.004..0.006)
0.7	uni	2.540 (2.535..2.545)	2.217 (2.214..2.220)	2.443 (2.438..2.448)	5.999 (5.987..6.010)	0.000 (−0.001..0.002)
	sym	2.530 (2.528..2.532)	2.203 (2.199..2.207)	2.432 (2.429..2.435)	5.995 (5.991..6.000)	−0.001 (−0.003..0.001)
	ort	2.459 (2.454..2.465)	2.198 (2.186..2.209)	2.394 (2.387..2.401)	6.000 (5.987..6.012)	0.001 (−0.003..0.006)
0.75	uni	2.430 (2.424..2.436)	2.163 (2.159..2.168)	2.363 (2.358..2.369)	5.999 (5.987..6.011)	0.000 (−0.001..0.002)
	sym	2.417 (2.415..2.419)	2.148 (2.143..2.156)	2.350 (2.347..2.353)	5.997 (5.992..6.001)	−0.001 (−0.003..0.001)
	ort	2.354 (2.347..2.360)	2.147 (2.135..2.157)	2.312 (2.304..2.319)	5.998 (5.985..6.011)	0.001 (−0.003..0.005)
0.8	uni	2.320 (2.314..2.326)	2.111 (2.099..2.125)	2.278 (2.271..2.286)	5.999 (5.987..6.011)	0.000 (−0.004..0.004)
	sym	2.307 (2.304..2.309)	2.095 (2.090..2.100)	2.264 (2.261..2.267)	5.999 (5.995..6.004)	−0.001 (−0.003..0.000)
	ort	2.146 (2.135..2.159)	2.046 (2.029..2.060)	2.136 (2.124..2.149)	5.995 (5.978..6.014)	0.001 (−0.002..0.003)
0.9	uni	2.107 (2.097..2.117)	2.009 (1.991..2.025)	2.097 (2.087..2.108)	5.997 (5.981..6.014)	−0.000 (−0.002..0.002)
	sym	2.092 (2.088..2.099)	1.988 (1.981..1.997)	2.082 (2.077..2.088)	6.005 (5.998..6.013)	−0.001 (−0.002..0.000)
	ort	1.948 (1.930..1.963)	α_1	α_1	5.991 (5.965..6.012)	0 (0..0)
1	uni	1.905 (1.886..1.925)	α_1	α_1	6.000 (5.974..6.026)	0 (0..0)
	sym	1.886 (1.877..1.896)	α_1	α_1	6.010 (5.999..6.023)	0 (0..0)
	ort	1.520 (1.508..1.535)	1.727 (1.715..1.738)	1.477 (1.418..1.551)	6.009 (5.985..6.034)	−0.001 (−0.006..0.003)
1.25	uni	1.473 (1.442..1.499)	1.688 (1.660..1.708)	1.422 (1.391..1.457)	6.036 (5.995..6.073)	0.006 (−0.002..0.011)
	sym	1.437 (1.424..1.450)	1.644 (1.634..1.655)	1.371 (1.338..1.409)	6.044 (6.027..6.061)	0.004 (0.001..0.007)
	ort	1.185 (1.161..1.206)	1.534 (1.518..1.550)	1.007 (0.912..1.079)	6.061 (6.017..6.102)	0.005 (−0.009..0.019)
1.5	uni	1.096 (1.073..1.124)	1.468 (1.453..1.483)	0.958 (0.836..1.017)	6.072 (6.031..6.118)	0.009 (−0.004..0.025)
	sym	1.060 (1.044..1.080)	1.450 (1.437..1.465)	0.889 (0.827..1.011)	6.090 (6.063..6.118)	0.024 (0.015..0.034)
	ort	0.920 (0.889..0.949)	1.372 (1.349..1.395)	0.590 (0.422..0.818)	6.145 (6.076..6.216)	0.029 (−0.001..0.058)
1.75	uni	0.841 (0.814..0.873)	1.301 (1.273..1.329)	0.479 (0.459..0.529)	6.175 (6.130..6.222)	0.041 (0.015..0.065)
	sym	no stability	1.262 (1.242..1.290)			0.050 (0.030..0.077)
	ort	0.719 (0.683..0.754)	1.231 (1.203..1.256)	0.190 (−0.068..0.727)	6.274 (6.173..6.380)	0.083 (0.031..0.132)
2	uni	0.622 (0.583..0.690)	1.173 (1.147..1.205)	0.131 (0.039..0.230)	6.293 (6.212..6.396)	0.113 (0.076..0.154)
	sym	no stability	1.118 (1.099..1.167)			0.120 (0.083..0.184)

Table 4.10: MFE α_q, D_q and $f(\alpha_q)$, and values for the corresponding symmetry relation Eq. (2.12) obtained for the WD symmetry classes.

4.6 Finite-size scaling for the Anderson model in the orthogonal class at fixed $\ell = 1$

Our further goal in Section 5 is to investigate the quantum percolation problem without broken time-reversal and spin-rotational symmetry. Percolation is a kind of disorder, therefore the model is expected to behave similar to the orthogonal Anderson model. In this model a fraction of lattice points is missing, therefore when performing a coarse graining, defined in Eq. 2.13, immediate difficulties arise. It is not clear how the ℓ-sized boxes have to be made, or how the boxes containing different number of filled sites should be compared. One way to resolve this problem is to choose $\ell = 1$, meaning that a box contains only one site. Even though this choice eventually opens the possibility to extend the MFSS method for irregular lattices or even for graphs and networks in the future, there is also a huge cost to be paid: the smoothing effect of the coarse graining is lost, and only the more complicated method of fixed-ℓ technique described in Section 3.2.4 remains. In this section we would like to test and also verify this technique for the Anderson model. Since we would like to investigate the multifractal exponents also, we will use *ensemble* averaged quantities only as in Section 4.4.

As mentioned in Section 2.3, there is always some numerical noise on the data, which becomes even more relevant for the smallest wave-function components. In case of negative q these uncertain small values are dominating the sums in R_q and S_q (see Eq. (2.6)). As written in Section 2.3 coarse graining clearly suppresses this effect, while at fixed $\ell = 1$ the smoothing effect of coarse graining is missing, thus for $q < 0$ the numerically obtained $\tilde{D}_q$ and $\tilde{\alpha}_q$ values are very noisy, see Figure 4.7(a). This makes every attempt to get results for negative q very hard if not impossible.

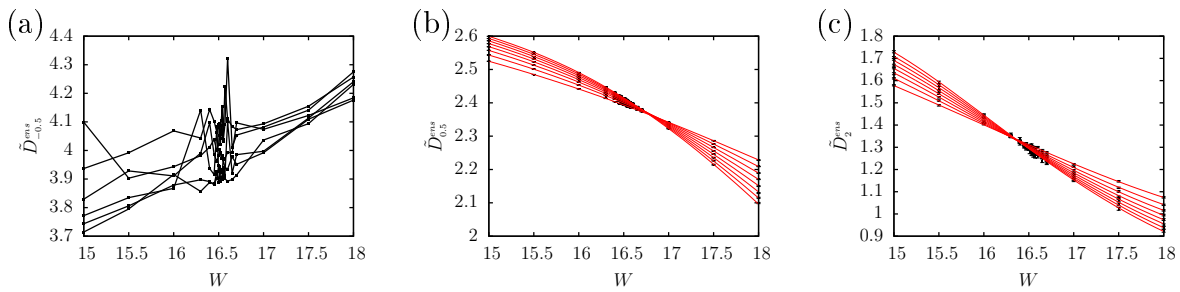

Figure 4.7: $\tilde{D}_q^{ens}(W, L, \ell = 1)$ at (a) $q = -0.5$ (b) $q = 0.5$ (c) $q = 2$ without coarse graining for fixed $\ell = 1$. Dots are raw data, solid black lines on (a) connect data points having the same system size as a guide for the eye, while solid red line on (b) and (c) shows the best fit obtained by MFSS.

The other problem is that the scaling law becomes more complicated, the leading number of fit parameters grow as $\sim n_{rel/irrel}^2$ for fixed $\ell = 1$, instead of $\sim n_{rel/irrel}$ as for fixed λ, while the amount of data is the same.

Performing the MFSS another problem appeared with Eq. (3.23). During the fit the irrelevant exponent, y, converged to very small $(10^{-3} - 10^{-5})$ or very large $(10^2 - 10^3)$ values. In the first case the irrelevant term can be merged with the relevant one, since

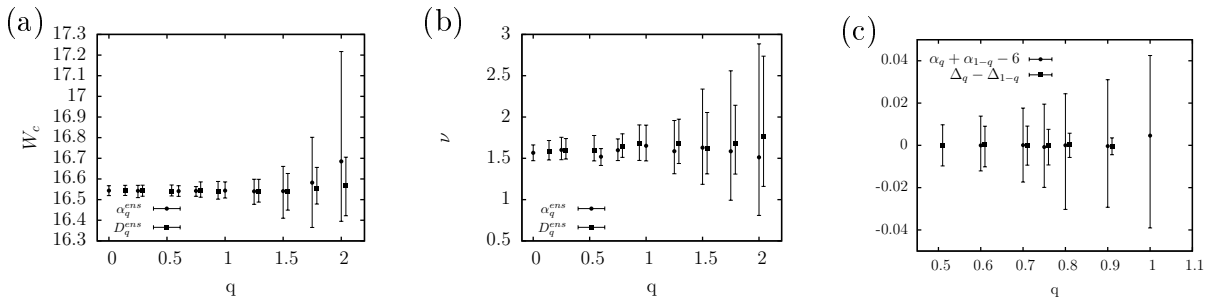

Figure 4.8: (a) The critical point, W_c, (b) the critical exponent, ν, (c) and the symmetry relation Eq. 2.12 for the 3D Anderson model obtained by MFSS at fixed $\ell = 1$. Error bars are 95% confidence levels. On subfigure (c) the $q \geq 0.5$ range is depicted, because of the symmetry of the depicted quantities for this point.

η is in most cases constant. In the second case L^{-y} suppresses the irrelevant part. This caused really large error in the b_{ij}, and it rendered the whole irrelevant part meaningless.

To find out whether this is just a numerical problem or if there is also some systematic physical meaning behind this behavior, we modeled the above problem: First a dataset was made by evaluating the expression Eq. (3.23) at system sizes and disorder we used before, with some expansion parameter values similar to ones provided by previous MFSS procedures. Of course fitting Eq. (3.23) to this dataset gave a perfect fit. Now adding some small random noise to the initial dataset started to shift the resulting fit parameters a little. By increasing the noise to the order of the standard deviation of our original dataset for the Anderson model the fit showed the expected phenomenon: The irrelevant exponent, y, converged to either large or small values. This shows that this is just a numerical artifact. There is a shift on the $\tilde{D}_q(W, L)$ curves for different system sizes, see Figure 4.7(b). This comes mostly from the $1/\ln L$ term of Eq. (3.23), and if noise is present it is numerically hard to determine the effect of the L^{-y} irrelevant part. All in all, however, in a finite system irrelevant variables are always present, considering an irrelevant term only will increase the error of the fit parameters. Therefore it seems to be useful to drop the irrelevant part, and keep the relevant one only. This way the fitting function reads as

$$\tilde{G}_q(W, L) = g_q + \frac{1}{\ln L}\left(\sum_{i=0}^{n_{rel}} \sum_{j=0}^{i} a_{ij} \varrho^i L^{\frac{j}{\nu}}\right). \tag{4.11}$$

We performed MFSS in the range $0 \leq q \leq 2$ with the criteria described in Section 3.2.5. The resulting critical point and exponent is visible in Figure 4.8. As we have already seen in Section 4.4, error bars are growing large beyond $q = 1$. The reason behind this is that increasing q increases the numerical and statistical errors through the μ_k^q expression. As mentioned above, increasing error on the data makes really difficult to get acceptable results from the MFSS. Therefore it is worth investigate the range $0 \leq q \leq 1$ only approximately.

As a result the critical point, W_c, and the critical exponent, ν, is consistent with our results at fixed $\lambda = 0.1$ (see Section 4.3) and also with the varying λ method (see Section 4.4). The resulting MFEs also agree with the results listed in Table 4.10 and with high precision results of Rodriguez *et al.* [32].

A test for the symmetry relation Eq. (2.12) is depicted in Figure 4.8(c). Eq. (2.12) is clearly fulfilled in the $0 \leq q \leq 1$ range.

4.7 Summary

In this chapter we examined the three-dimensional Anderson models belonging to the conventional WD symmetry classes with the help of multifractal finite-size scaling using two methods: a simpler method for fixed λ leading to a single-variable scaling function, and a more complicated one for varying λ resulting in a two-variable scaling function. Both methods confirmed the presence of multifractality in all three symmetry classes, and we obtained critical parameters in agreement with each other and with previous results known from the literature. The more complicated varying λ method provided more precise values for the critical parameters, listed in Table 4.5, and significantly different critical exponents for the different WD symmetry classes.

Applying the method of varying λ we also calculated the multifractal exponents, which basically fulfill the expected symmetry relation Eq. (2.12), small deviations were detected for large values of q probably due to slightly underestimated error bars. In Figure 4.4 one can see that the MFEs of different symmetry classes are very close to each other, but Figure 4.6 or Table 4.10 shows significant differences between them for most of the values of q. We compared the difference of α_0 in the unitary and symplectic class to available results in two dimensions, and we found completely different relation between the two and three-dimensional cases. We expanded the MFEs in terms of the variable $q(1-q)$, and determined the expansion coefficients up to third order numerically. The expansion coefficients of Eq. (4.6)–(4.7) fulfill the expected relation $a_k = kd_k$ giving a further confirmation for the validity of our results for the MFEs listed in Table 4.10. We also compared the numerical results to available analytical estimates, and found in some cases similar, but in other cases opposite qualitative behavior for expansion coefficients for the orthogonal and the unitary classes. Nevertheless, we believe that the numerical precision of our results should be used as tests for future renormalization or other type of expansion approximations. Therefore our results await analytical comparison.

We also performed MFSS at fixed $\ell = 1$, to develop the method applicable for irregular lattices, or even for graphs in the future. We found that due to growing error bars, the range $0 \leq q \leq 1$ is worth to investigate. We found matching results for the critical point, critical exponent and multifractal exponents with our previous results at fixed λ and varying λ, what verifies this method.

Chapter 5

Quantum percolation model

5.1 Introduction

Beside diagonal disorder resembling substitutional disorder the other main cause of irregularity in condensed systems is structural disorder. For the investigation of topological and structural disorder percolation is one of the most important and widely used models. Percolation in general has a wide applicability in many fields of physics [44]. In the Bernoulli site-percolation problem every site is filled with probability p and is empty with probability $1-p$ independently. The main goal of classical percolation is to tell for a given p whether an infinite cluster of filled sites may exist in the thermodynamic limit or not. It turns out that there is such a critical probability, p_c^C, below which ($p < p_c^C$) there is no infinite cluster but above which ($p > p_c^C$) there is. On a hypercubic lattice in one dimension [45] $p_c^C = 1$, in two dimensions [46] $p_c^C = 0.592746216 \pm 0.00000013$, in three dimensions [47] $p_c^C = 0.3116077 \pm 0.0000002$. In the $p > p_c^C$ case the existence of an infinite cluster ensures that the system can be treated as a conductor, since classical particles can travel through the whole system. On the other hand if $p < p_c^C$, the system consists of a set of disjoint, finite clusters, and as a consequence, it behaves as an insulator, since no particle can escape from its initial finite cluster.

For the electric conduction properties of a sample the electrons are responsible, therefore to examine the most simple model, we shall investigate spinless non–interacting electrons on a percolated lattice without magnetic field, this is called the quantum percolation model. The corresponding Hamiltonian is

$$\mathcal{H} = \sum_{i \in A} \varepsilon a_i^\dagger a_i - \sum_{\substack{\langle i,j \rangle \\ i,j \in A}} \left(a_i^\dagger a_j + a_j^\dagger a_i \right), \tag{5.1}$$

where A is the set of filled sites, ε is a constant on–site energy, whose value can be safely set to zero without loss of generality. Setting the hopping elements to 1 is equivalent to choosing the energy unit. Note that the pure site–percolation problem is equivalent to a binary Anderson model [48, 49, 50] with constant ε_A and ε_B but taking the limit $\varepsilon_B \to \infty$:

$$\mathcal{H} = \sum_{i \in A} \varepsilon_A a_i^\dagger a_i + \sum_{i \in B} \varepsilon_B a_i^\dagger a_i - \sum_{\langle i,j \rangle} \left(a_i^\dagger a_j + a_j^\dagger a_i \right) \tag{5.2}$$

This Hamiltonian could describe an alloy of a perfect metal consisting of atoms A and a perfect insulator consisting of atoms B only. All A sites are equivalent, and the B sites cannot be reached due to their infinite on-site energy, therefore B sites behave as if they were empty. This suggests that quantum percolation behaves similar to the Anderson model. In this chapter we shall show many similarities between quantum percolation and the original Anderson problem. The most important similarity with the Anderson problem is the existence of a metal–insulator transition for the quantum percolation model too, however, here p, or strictly speaking $(1-p)$, plays the role of disorder: For $p < p_c^C$ every state is localized onto finite, connected islands, thus the sample is an insulator. Increasing p beyond p_c^C, however, a classical particle can travel through the sample, the electron wave-functions are localized due to strong interference effects caused by disorder, the sample still remains an insulator. For p values slightly below 1 states are perturbed Bloch-states, the sample is a metal. In between there exists a mobility edge, $p_c^Q(E)$, an energy–dependent quantum critical point, below which electronic eigenstates are Anderson-localized giving rise to an insulator, and above which they are extended forming a metal. Along the mobility edge, $p_c^Q(E)$, the states are supposed to be multifractals, see Figure 1.4 for the phenomenon and similarities between the two models. In Section 5.4.2 we argue that the corresponding Anderson model and the quantum percolation model belong to the same universality class.

Conductivity is possible through an infinite cluster only, therefore only the infinite cluster should be investigated, thus $p_c^Q > p_c^C$, so only the $p > p_c^C$ regime is interesting for us. Since numerically we can deal with a finite lattice only, we restricted our work on the largest finite cluster, which was found by a Hoshen-Kopelman algorithm [51].

Electronic conduction is only possible on an infinite cluster, so $p_c^Q > p_c^C$ is expected, therefore the infinite cluster should be investigated, therefore only the $p > p_c^C$ regime is interesting for us. Since numerically one can deal with a finite lattice only, we restricted our work on the largest finite cluster found by a Hoshen-Kopelman algorithm [51].

At first let us take a glance at the density of states (DOS) because for the quantum percolation problem it deserves a special attention.

5.2 Density of states

The DOS of the giant cluster has itself an unusual form. The evolution of this function with p is depicted in Figure 5.1. With increasing disorder, in the present case this means decreasing p, more and more sharp peaks appear in the spectrum. These peaks correspond to special, so-called "molecular states", which are localized on a few sites [48]. These states are non-zero on a few sites only and exactly zero on every other one due to exact destructive interference. Therefore they are not localized in the sense of Anderson localization, there is no exponential decay in the wave-function envelope. Typical few-site structures and corresponding energies are given on the right side of Figure 5.1. Since the value $E = 0$ appears for most clusters as an eigenvalue, the highest peak of the DOS is at the middle of the band, and there is also a pseudo–gap around it.

Considering other few-site clusters there is no reason for the eigenvalues to avoid any part of the band, therefore peaks in the DOS corresponding to molecular states should appear densely in the thermodynamic limit. The energy of a molecular state is a strict

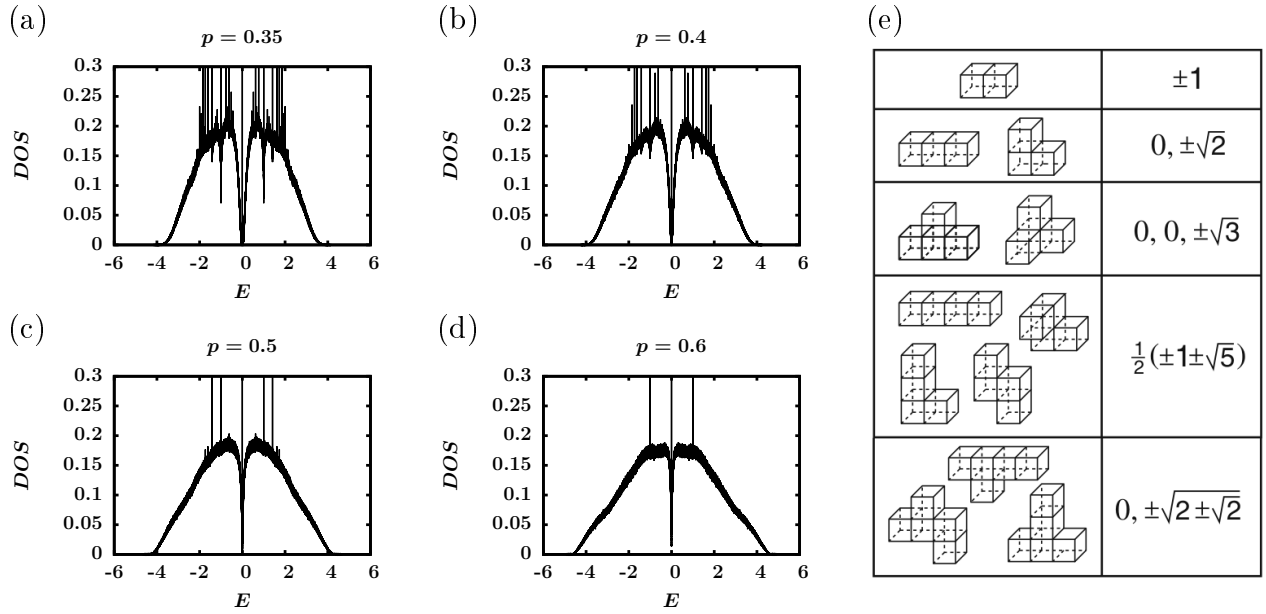

Figure 5.1: Left side: Density of states of quantum percolation model at different site-filling probabilities, (a) $p = 0.35$, (b) $p = 0.4$, (c) $p = 0.5$, (d) $p = 0.6$. Panel (e): Small clusters corresponding to special energies taken from the review of Schubert and Fehske [52].

value, thus the peaks in the DOS appear as a series of Dirac-deltas. As we can see, the spectrum consists of two parts: a dense point spectrum due to molecular states, and a continuous one due to all other states [48]. This statement has been rigorously proven recently in the case of a 2D square lattice, and for tree graphs corresponding to an effective infinite dimension, therefore it is conjectured to be true in any dimension [53].

5.3 The role of chirality

In Figure 5.2 two states are visible from the band center. Figure 5.2(a) looks like a molecular state from Figure 5.1(e), but in Figure 5.2(b) and (c) one can see that states at the band center can extend over rather large regions also. This suggests that not only strogly localized molecular states are present at the band center. Looking more carefully one can notice a chessboard pattern on Figure 5.2(c). To see this effect better in Figure 5.3 we present wave-functions also in two dimensions, where this effect is visible more clear.

The cubic lattice is a bipartite lattice and the Hamiltonian (5.1) couples nearest neighbors only, therefore from one sublattice, α, it is possible to hop to the other sublattice, β, only. The chessboard pattern resembles to chiral states living on sublattices of bipartite lattices. In fact introducing the $i = xL^2 + yL + z$ index, the matrix

$$C_{ii} = \begin{cases} 1 \text{ if } i \text{ is even } (\alpha \text{ sublattice}) \\ -1 \text{ if } i \text{ is odd } (\beta \text{ sublattice}) \end{cases} \tag{5.3}$$

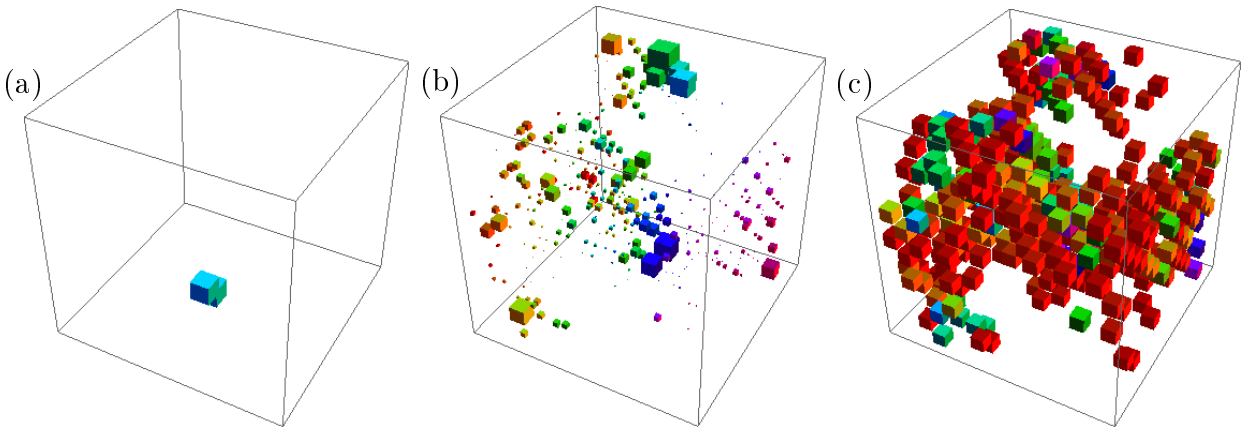

Figure 5.2: Wave-functions at $p = 0.5$, $E = 0$: On (a) and (b) the size of a cube is proportional to $\sqrt{|\Psi_i|^2}$, coloring is due to x coordinate, on (c) size is uniform, but coloring is due to $\sqrt{|\Psi_i|^2}$.

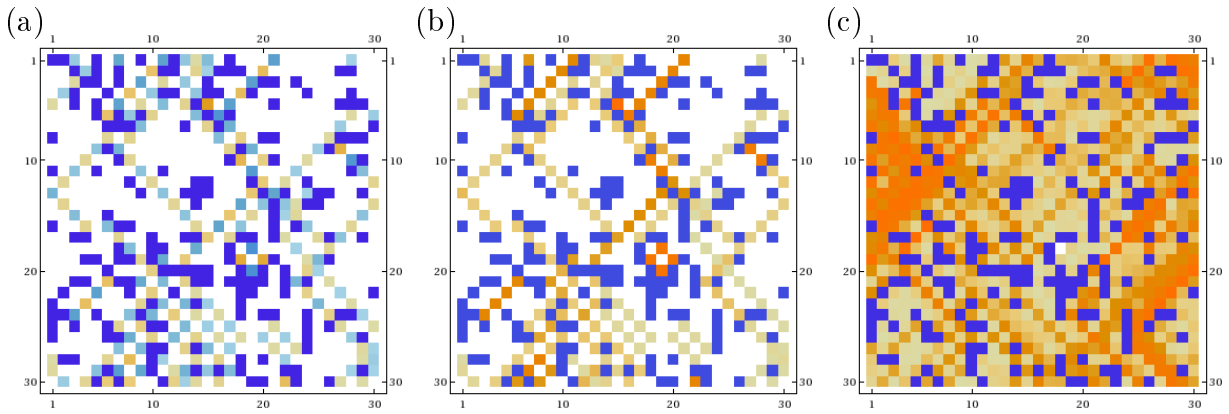

Figure 5.3: Wave-function in two dimensions at $p = 0.8$ (a) $E = 0$, square of the wave-function at (b) E=0, (c) $E = 0.02$. Coloring is due to Ψ_i on (a) and $|\Psi_i|^2$ on (b) and (c), blue squares are empty sites.

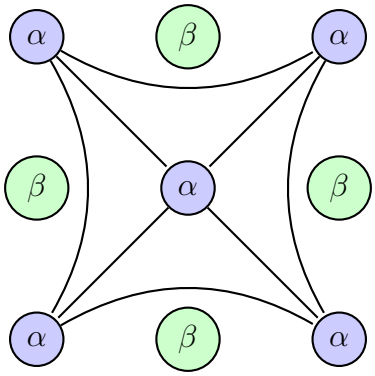

Figure 5.4: Hopping elements in the „renormalized" Hamiltonian, $\mathcal{H}^2$

anticommutes with the Hamiltonian in Eq. (5.1), thus C acts as a chirality transformation [54]. Therefore the quantum percolation model is a chiral model. In the low (high) energy range the states have antibonding (bonding) character. In the middle of the band, around $E = 0$, chessboard-like chiral states appear. These chiral states exactly at $E = 0$ are eigenfunctions of C, as well, therefore they are protected against off-diagonal disorder.

In other words the lattice is bipartite, and it can be decoupled into two sublattices, α, β. Let us introduce the projections to the sublattices:

$$P_\alpha = \sum_{i\in\alpha} |i\rangle \langle i| \qquad P_\beta = \sum_{j\in\beta} |j\rangle \langle j| \qquad C = P_\alpha - P_\beta. \tag{5.4}$$

Since the lattice is bipartite

$$\mathcal{H}P_\alpha |\Psi\rangle = EP_\beta |\Psi\rangle \qquad \mathcal{H}P_\beta |\Psi\rangle = EP_\alpha |\Psi\rangle \tag{5.5}$$

holds, therefore the square of the Hamiltonian decouples the two sublattices:

$$\mathcal{H}^2P_\alpha |\Psi\rangle = E^2P_\alpha |\Psi\rangle \qquad \mathcal{H}^2P_\beta |\Psi\rangle = E^2P_\beta |\Psi\rangle \tag{5.6}$$

Now one can „renormalize" the square of the Hamiltonian, see [54]. This Hamiltonian has hopping elements depicted in Figure 5.4.

In order to understand the sub gap appearing around the middle of the band, $E = 0$, we invoke the arguments of Ref. [54]. The vicinity of $E = 0$ belongs to the low-energy regime of the spectrum of $\mathcal{H}^2$, therefore here antibonding states should appear, which are more or less visible in the alternating light blue and orange squares of Figure 5.3(a), if the white parts corresponding to the β sublattice is removed. But the hopping elements to the diagonal-lying second neighbors in Figure 5.4 introduce triangles. Triangles and the antibonding nature together lead to frustration. Based on the frustration of the states around zero energy Naumis *et al.* [54] showed in two dimensions, that the width of the pseudogap around zero energy, Δ, is connected to the peak at $E = 0$:

$$\Delta \sim \sqrt{\rho_0}, \tag{5.7}$$

where ρ_0 stands for the weight of the zero energy states in the spectra. They also showed that the width of the pseudogap tends to zero in the non-disordered limit, $\lim_{p\to 1} \Delta = 0$.

The extension of these arguments to three dimensions should be valid, since the most important ingredient of their calculation is the coordination number of the lattice, and not the dimensionality itself explicitly.

The states close to $E = 0$ belong to the edge of the spectrum of $\mathcal{H}^2$, which is a disordered Hamiltonian. Therefore the pseudogap might be qualitatively interpreted as the Lifshitz tail (see Section 1.2) of $\mathcal{H}^2$, leading to localized states close $E = 0$.

5.4 Finite size scaling for the 3D quantum percolation model using MFEs

5.4.1 Numerical calculations

In this section our goal is to find the mobility edge and the critical exponent of the 3D quantum percolation model, and investigate the multifractal properties of the critical wave-functions. Since molecular states are strongly localized, they cannot contribute to conduction. Therefore we restrict our investigation to the continuous part of the spectrum only. Since the Hamiltonian Eq. 5.1 is symmetric for $E \leftrightarrow -E$ exchange, the $E \geq 0$ interval is investigated only. With the numerical method described in Section 4.2 we are computed one single eigenstate of the Hamiltonian having an eigenenergy close to a given value of E. In Figure 5.1 it is shown that in a finite system molecular states appear frequently at few special energies only, e.g. $E = 0, \pm 1, \pm\sqrt{2} \ldots$, therefore for our purpose we have chosen energy windows avoiding the peaks in the DOS. Beside that, to cover the most interesting regions of the band we chose the following energies: $E = 0.001,\ 0.01,\ 0.1,\ 0.3,\ 0.7,\ 1.1,\ 1.5,\ 2.1,\ 3.1,\ 4.1$. For averaging we considered only one wave-function per realization with the eigenvalue closest to the chosen energy E to avoid correlations. We only used an eigenfunction if its energy was in a $\Delta E = 0.01$ wide interval around E, except for $E = 0.001$ and $E = 0.01$, where $\Delta E = 0.00001$ and $\Delta E = 0.001$ were used.

Our ΔE energy intevals are so small that it completely excludes the effect of molecular states. We ran a test after the finite-size scaling was performed: Molecular states have strict energy value, therefore at fixed system size, L, disorder, p, and energy, E, we left out from our raw dataset all the wave-functions with the same energy value (at most 2% of the original raw dataset). Note that these states are not necessarily molecular states, they can be regular ones too, having the same energy within numerical precision. We redid our whole finite-size scaling procedure (as described in Section 5.4.2), but this additional refinement had no effect on the results. This test ensures that we filtered out the molecular states very effectively, and if they were present in our raw dataset, their effect would be negligible.

At every energy we searched for the p_c^Q point. From the approximately $\Delta p = 0.01$ wide neighborhood around p_c^Q we picked about 20 values of p. For the higher p_c^Q values at fixed system size, L, there are more sites in the giant cluster, thus the Hamiltonian matrix is larger, and takes more time to find the closest eigenvalue to the given energy. On the other hand R_q and S_q are calculated from more data, thus they are more precise. Considering these arguments we investigated system sizes and number of samples visible in Table 5.1. All in all 45 045 000 wave-functions were calculated.

system size (L)	number of samples	
	$p_c^Q < 0.41$	$p_c^Q > 0.41$
20	50000	50000
30	50000	50000
40	50000	50000
60	50000	25000
80	20000	10000
100	10000	5000
120	5000	
140	4000	

Table 5.1: System sizes and number of samples of the simulation for the 3D quantum percolation model.

5.4.2 Finite size scaling at fixed $\ell = 1$

The method we use here has been described in Section 4.6 for the orthogonal Anderson model. As written in Section 4.6 error bars are very large for $q > 1$, thus we investigate the range $0 \leq q \leq 1$ only. Since we would like to investigate the MFEs also, we use only the *ensemble* averaged GMFEs. The typical behavior of these exponents is depicted in Figure 5.5, note that curves do not have a common crossing point due to the $1/\ln L$ term in Eq. 4.11.

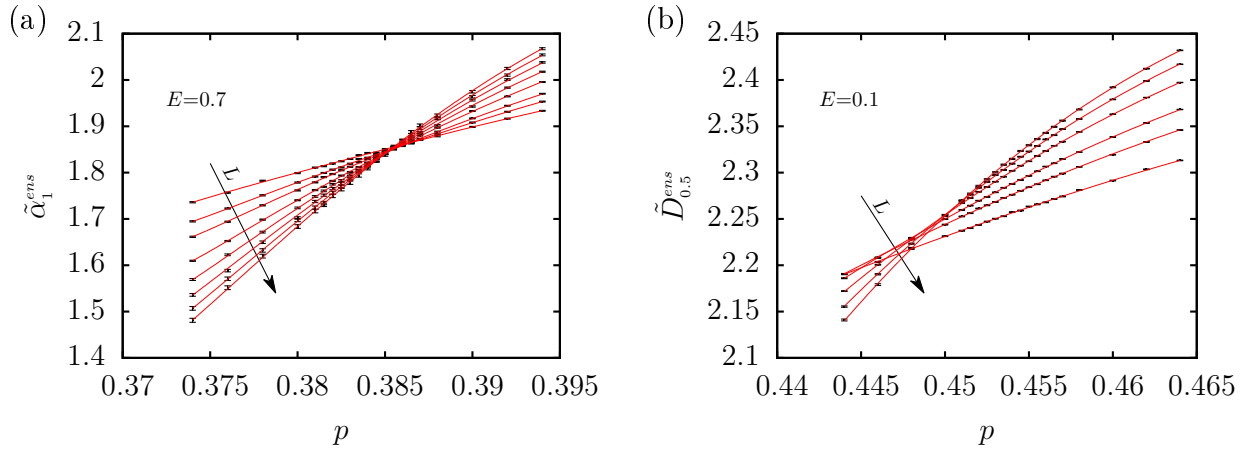

Figure 5.5: The generalized multifractal exponents (a) $\tilde{\alpha}_1^{ens}(p, L, \ell = 1)$ at $E = 0.7$ and (b) $\tilde{D}_{0.5}^{ens}(p, L, \ell = 1)$ at $E = 0.1$ for the 3D quantum percolation model. Points with error bars are the raw data, red solid lines are the best fits of the function Eq. 4.11 as a function of disorder, p, at different system sizes, L.

The MFSS at fixed $\ell = 1$ for the range $0 \leq q \leq 1$ provided critical points, critical exponents and MFEs for every q value at every chosen energy, E. For fixed energy the critical points and critical exponents should be q-independent, which can be fulfilled within the 95% confidence level, see Figure 5.6. To achieve the q-independence we had to limit the minimal system size at $L_{min} = 30$ or $L_{min} = 40$ in some cases.

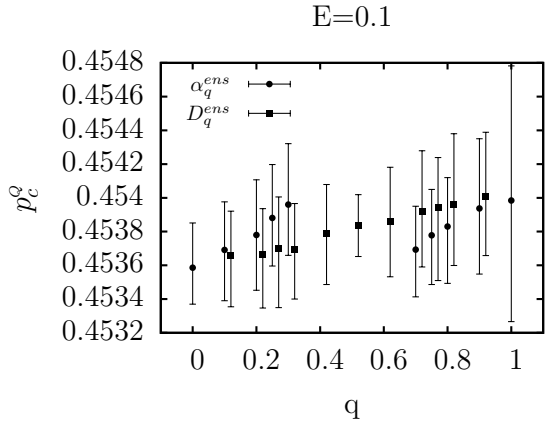

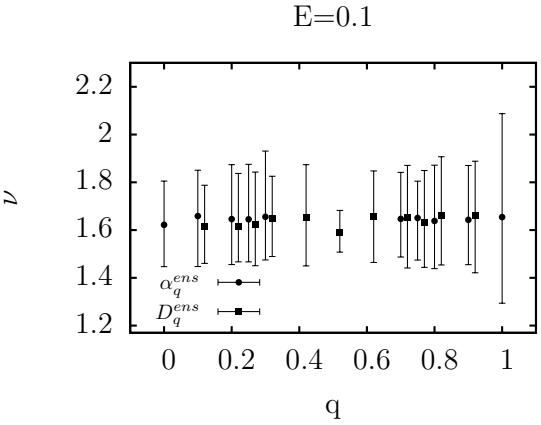

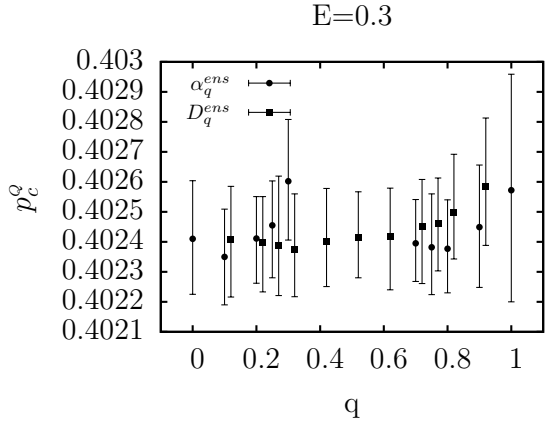

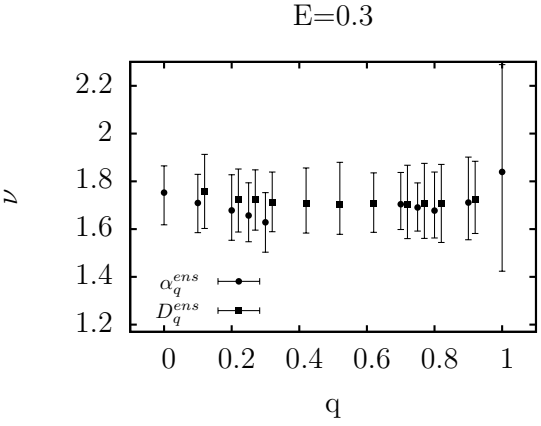

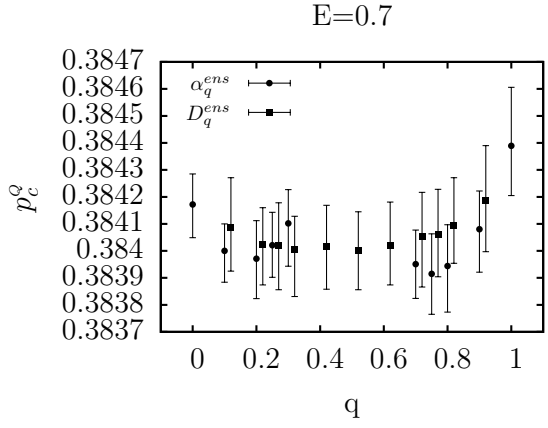

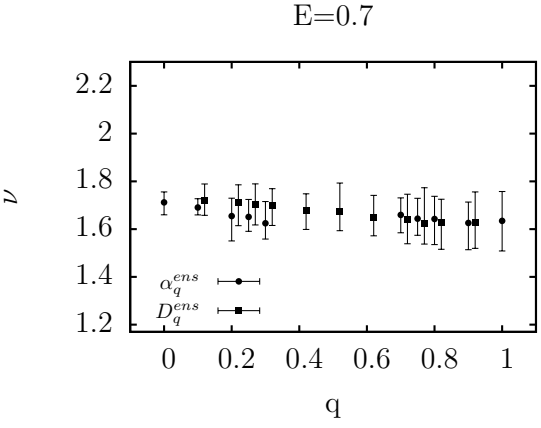

Continued on next page

Continued from previous page

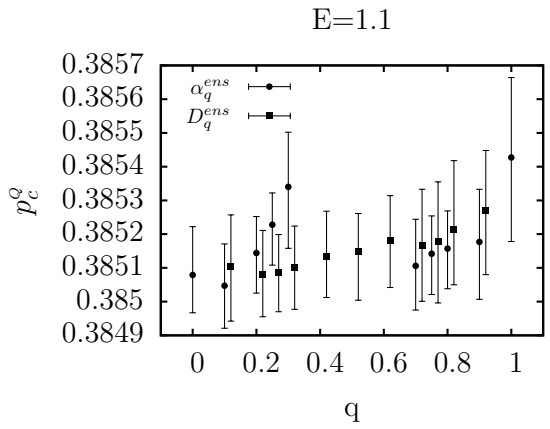

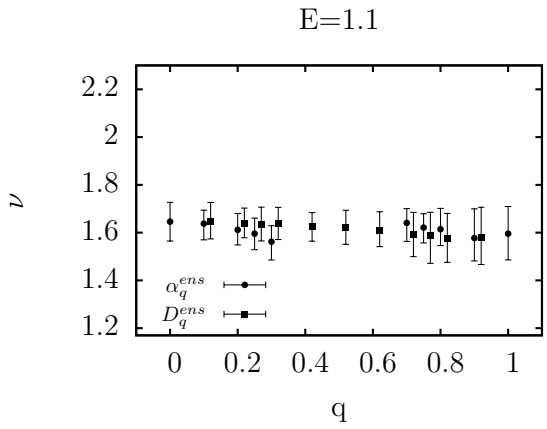

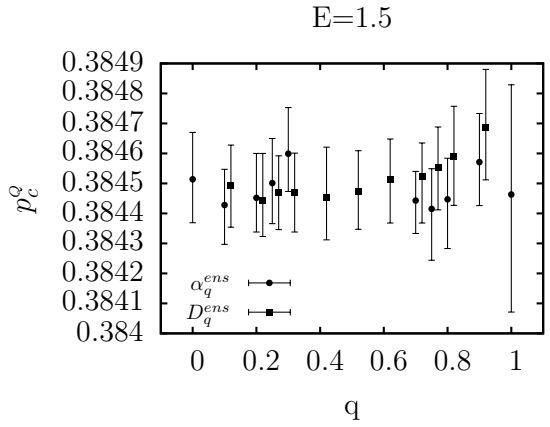

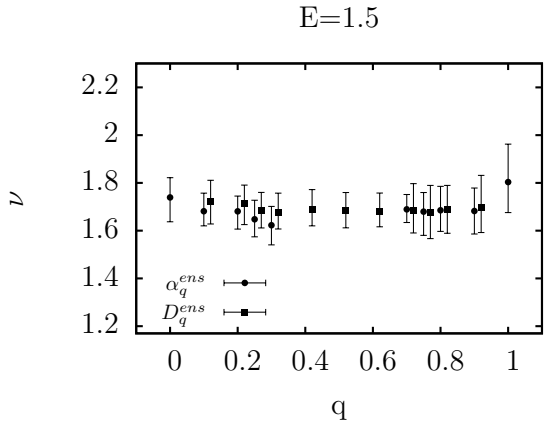

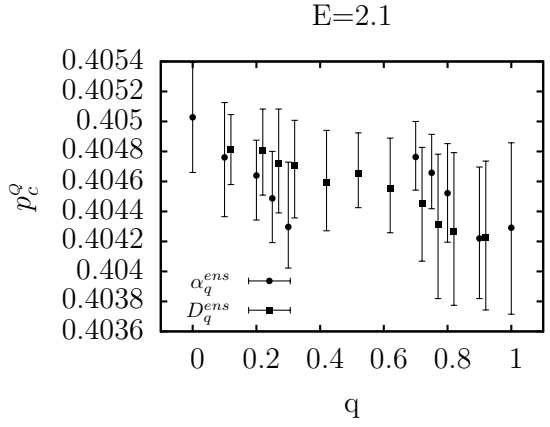

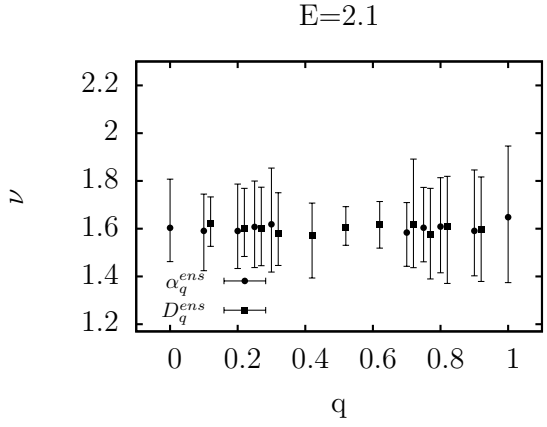

Continued on next page

Continued from previous page

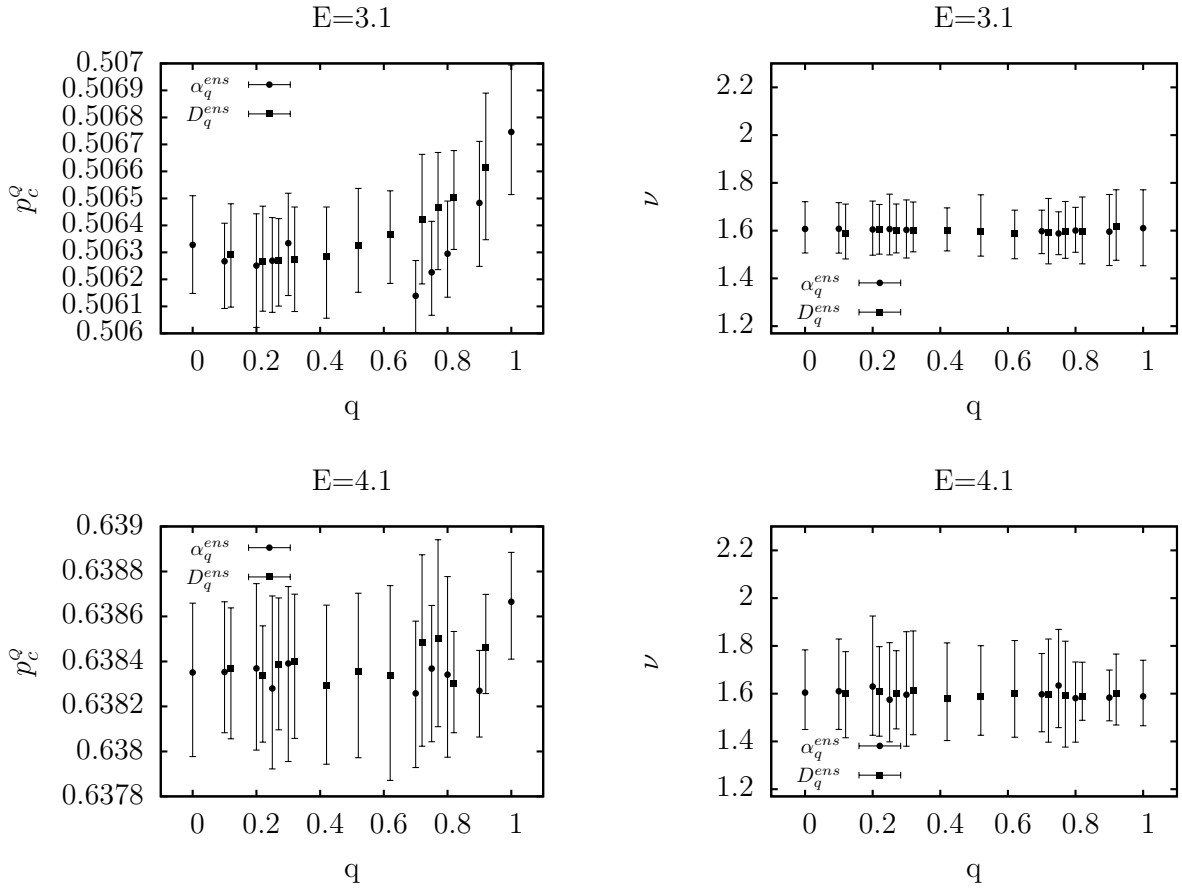

Figure 5.6: Critical point (left column) and critical exponent (right column) of the 3D quantum percolation model at different energies. Error bars are 95% confidence levels.

The critical point, p_c^Q, shifts in most cases, but the shift is within the 95% confidence band. An interesting feature is that p_c^Q obtained from α_q for $q \leq 0.5$ and $q \geq 0.5$ shifts in the opposite direction. For $\alpha_{0.4}$ and $\alpha_{0.6}$ the MFSS mostly did not converge since $\alpha_{0.5} = d$ and close to the $q = 0.5$ point $\tilde{\alpha}$ curves have similar steepness close to the critical point, therefore it is numerically hard to determine a well–defined crossing point after scaling out the $\ln L$ shift, see Figure 5.7. Therefore these data are not presented in Figure 5.6, similarly to Section4.4.

For $E = 0.001$ and $E = 0.01$ the MFSS showed severe convergence troubles, and even if it converged, provided fit parameters with very large error. The reason behind this behavior is presumably the close vicinity of the pseudogap at $E = 0$ in the DOS, and it is very hard even to find eigenvalues close enough to the desired energies $E = 0.001$ or $E = 0.01$. Another difficulty in this case is that the mobility edge becomes anomalous approaching $E = 0$, see Figure 5.8(a). Therefore only a narrow energy-band is permitted for averaging around $E = 0.001$ or $E = 0.01$, which decreases further the possible number of eigenstates. For these reasons parameters coming from MFSS at $E = 0.001$ and

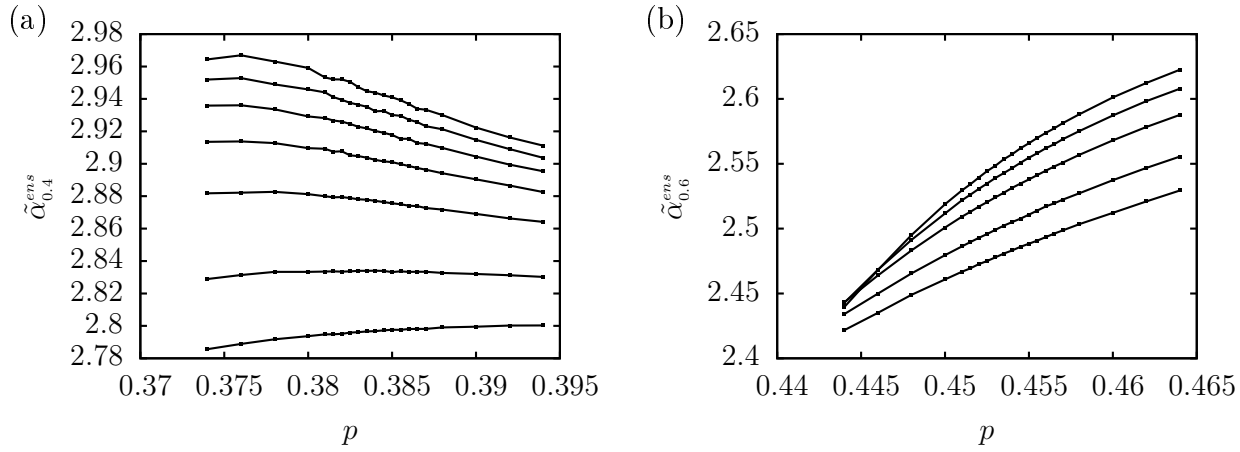

Figure 5.7: The generalized multifractal dimensions (a) $\tilde{\alpha}^{ens}_{0.4}(p, L, \ell = 1)$ at $E = 1.5$ and (b) $\tilde{\alpha}^{ens}_{0.6}(p, L, \ell = 1)$ at $E = 0.1$ for the 3D quantum percolation model. Dots are raw data, solid lines connect data points having the same system size as a guide for the eye.

E	MFE	p_c^Q	ν	N_{df}	χ^2	L_{min}	n_{rel}	n_ϱ
0.1	$D_{0.5}$=2.421 (2.416..2.426)	0.45384 (0.45365..0.45402)	1.591 (1.508..1.682)	136	113	20	3	1
0.3	$D_{0.5}$=2.397 (2.393..2.402)	0.40241 (0.40228..0.40257)	1.705 (1.578..1.879)	157	123	20	3	1
0.7	$D_{0.6}$=2.271 (2.265..2.278)	0.38402 (0.38387..0.38418)	1.645 (1.572..1.741)	181	150	20	4	1
1.1	$D_{0.6}$=2.262 (2.257..2.268)	0.38518 (0.38504..0.38531)	1.609 (1.542..1.688)	243	155	20	3	1
1.5	$D_{0.8}$=2.027 (2.020..2.035)	0.38459 (0.38443..0.38476)	1.688 (1.589..1.789)	144	154	20	3	2
2.1	$D_{0.5}$=2.439 (2.431..2.448)	0.40466 (0.40443..0.40492)	1.606 (1.530..1.692)	127	116	40	2	2
3.1	$D_{0.4}$=2.542 (2.538..2.546)	0.50628 (0.50606..0.50647)	1.603 (1.515..1.695)	138	113	20	3	1
4.1	$\alpha_{0.9}$=2.108 (2.101..2.114)	0.63827 (0.63806..0.63845)	1.584 (1.486..1.699)	128	113	20	3	1

Table 5.2: Resulting data along the mobility edge. These q values were chosen to compute ν and obtain the mobility edge depicted in Figure 5.8.

$E = 0.01$ were only used to plot the mobility edge, these two points are denoted with empty squares in Figure 5.8(a).

At fixed energy we picked one q point that represents well the results for that energy. The p_c^Q values are leading to a mobility edge, see Figure 5.8(a). The ν values are independent, and due to universality they should not depend on the energy. Thus they can be averaged, providing a more precise critical exponent, $\nu = 1.622$ (1.587..1.658), see Figure 5.8(b). To derive the average, the data points were weighted by their inverse variance, the error bar is twice the standard deviation of the mean, which is about the 95% confidence band for a Gaussian.

In the literature there are previous works showing a mobility edge [49, 50, 52, 55], see Figure 5.9. The shapes of these curves are very similar: a steep decrease around $E = 0$, then a plateau resulting in a global quantum percolation threshold for the system, and finally an increasing behavior with growing energy. The curves are in good qualitative agreement with each other, beyond $E = 3$ quantitative agreement is also present. Curves of Soukoulis [50] and Schubert [52] have jumps at $E = 1$ and $E = \sqrt{2}$ (only Ref. [52]) due to the most frequent molecular states probably. Our curve is in really good agreement with recent result of Travenec [55] obtained by transfer matrix methods; curves are

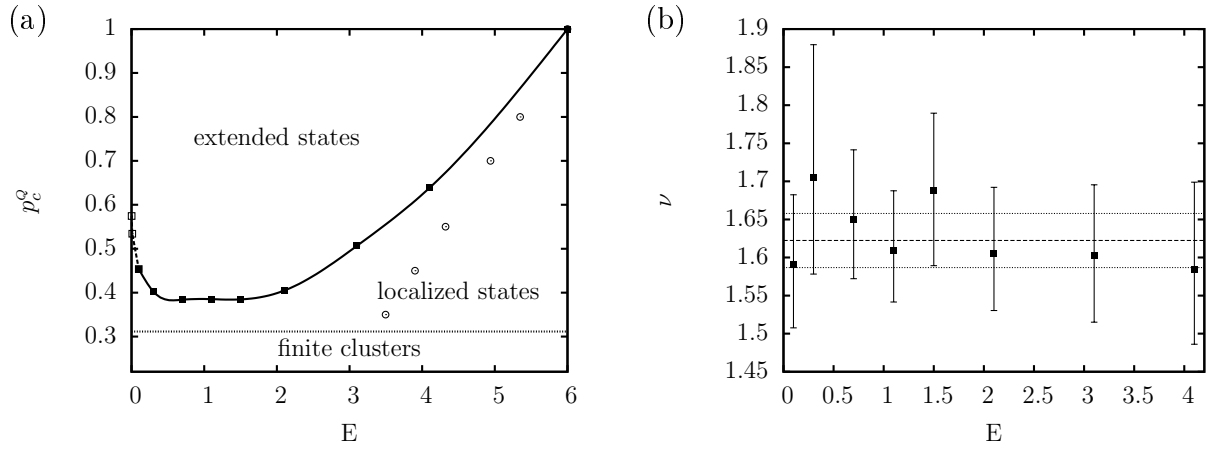

Figure 5.8: (a) Mobility edge for the 3D quantum percolation model, dotted line denotes the classical percolation threshold, $p_c^C = 0.3116077 \pm 0.0000002$ [47]. Circles are approximate values of the bandwidth, beyond them only the Lifshitz-tail is present. Squares are results from MFSS, line is a spline to guide for the eye. Empty squares and dashed lines are for approximate data obtained from MFSS at $E = 0.001$ and $E = 0.01$ (b) Critical exponent for the 3D quantum percolation model. Error bars are for 95% confidence band. Dashed line is the average, dotted lines note the 95% confidence band around the average. The resulting critical exponent is $\nu = 1.622$ (1.587..1.658). Corresponding data is listed in Table 5.2.

almost covering each other. His critical exponent is also in good agreement with ours, see Table 5.3.

At low p values the bandwidth is small, but increasing p results in a wider band. In the Lifshitz-tail only localized states are present, therefore the mobility edge curve should be above the curve of the bandwidth. As a result the mobility edge curve increases at high energies in Figure 5.8(a). Reaching the edge of the band, $E \to 6$, the mobility edges drawn from the data points of different authors seem to converge to 1. Therefore we put a point in the right-top corner of Figure 5.9; however, at $p = 1$ the sample is a perfect crystal, and wave-functions are completely extended Bloch-functions over the whole band.

Exactly at the center of the band, $E = 0$, on the other hand, extremely localized molecular states disturb the picture, in addition close to the band center a pseudogap forms in the DOS (see Section 5.2 and Figure 5.1), therefore this regime is really hard to investigate numerically. Even though the localized molecular states at $E = 0$ belong to the point spectrum, it is still not clear, what is the $E \to 0$ limit of the mobility edge, describing the continuous spectrum. The question arises: Does the very steep increase of the mobility edge approaching $E = 0$ result in a $\lim_{E\to 0} p_c^Q(E) = 1$ or the limit is lower than one? Based on the arguments in Section 5.3 our guess is that at any finite disorder, $p < 1$, there are localized states near $E = 0$, resulting a limit of unity for the mobility edge, $\lim_{E\to 0} p_c^Q(E) = 1$.

Some values of the critical exponent can also be found in the literature. In Table 5.3 we collected these values ranging from 1.2 to 1.95. Because of the more limited

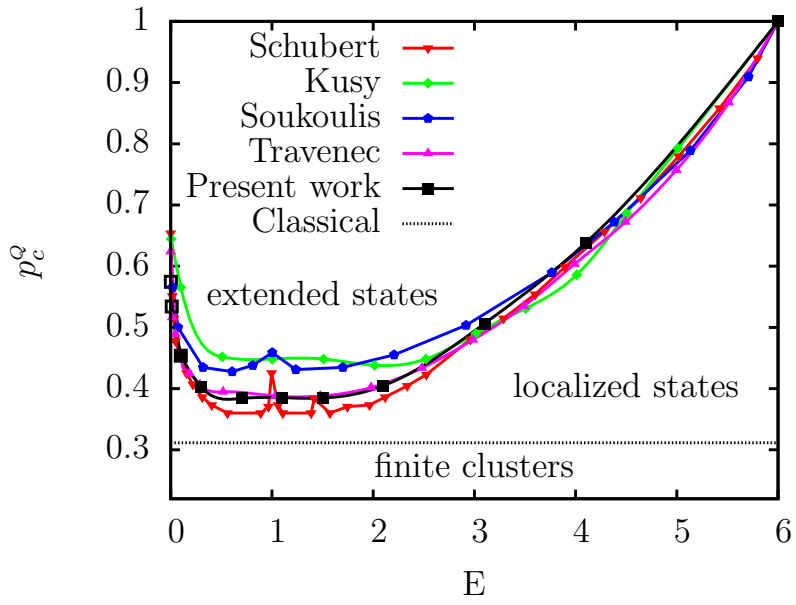

Figure 5.9: Mobility edge of the 3D quantum percolation model in the literature [52][49][50][55][47].

computational efforts, previous works used much smaller system sizes compared to our possibilities, leading to much bigger finite size effects, affecting their FSS. Conductivity or transfer matrix methods used to overestimate, while level statistics and Green-function techniques used to underestimate the critical exponent, ν. Our critical exponent is practically in the center of the interval of previous results $1.2 \leq \nu \leq 1.95$. Our exponent, $\nu = 1.622$ (1.587..1.658) is in very good agreement with the most recent study of Travenec[55] similarly to the mobility edge. Furthermore the critical exponent is within confidence band with our most precise previous result for the orthogonal Anderson model ($\nu = 1.595$ (1.582..1.609)) obtained by the varying λ method, see Table 4.5, or with the high precision value ($\nu = 1.590$ (1.579..1.602)) of Rodriguez *et al.* [32], however our result seems to be a bit higher. As written in Section 1.3, chiral and non-chiral Anderson models are very similar to each other in the bulk of the spectrum. Therefore our matching critical exponent provides further evidence to previous conjectures and statements, saying that the chiral orthogonal Anderson model and the 3D quantum percolation model belong to the same universality class.

5.5 Analysis of MFEs

MFSS provided us the points of the $D_q(E)$ and $\alpha_q(E)$ surface at the investigated energies and q values. By inversion of the mobility edge curve, $p_c^Q(E)$ one can derive the MFEs as a function of p_c^Q and of q, see Figure 5.10. Since $D_0 = d$, at small q values, i.e. $q \to 0$, the results for D_q are p_c^Q-independent, but for larger values of q the D_q starts to shift down with decreasing p_c^Q, which shows up in the lower right corner of Figure 5.10(a). In the lower regime of Figure 5.10(c) this shift is visibly significant. The same phenomenon

Author	Year	ν	Method	Sytem size
Root-Bauer-Skinner[56]	1988	1.8 ± 0.11	conductivity	$L = 3 - 9$
Koslowski-von Niessen[57]	1991	1.95 ± 0.12	conductivity	$L = 6 - 9$
Berkovits-Avishai[58]	1996	1.35 ± 0.1	level statistics	$L = 7 - 15$
Kusy *et al.*[49]	1997	1.2 ± 0.2	Green-function	$L = 4 - 8$
Kaneko-Ohtsuki[59]	1999	1.46 ± 0.09	level statistics	$L = 12 - 21$
Travenec[55]	2008	1.6 ± 0.1	conductivity	$L = 14 - 20$
Present work	2014	1.622 ± 0.035	multifractality	$L = 20 - 140$

Table 5.3: Critical exponent of the 3D quantum percolation model in the literature.

can be detected for α_q. This suggests that D_q and α_q seem not to behave as universal quantities.

At relatively larger values of p_c^Q, D_q and α_q fulfill the symmetry relation Eq. (2.12), see Figure 5.11 (a), (b), (e) and (f). However, at the bottom of the mobility edge, where p_c^Q is smaller, meaning that the lattice is more diluted or more irregular, deviations from the symmetry law seem to be prominent. The D_q and α_q values remain the same at small q, i.e. when $q \to 0$, but drop down as q increases. Resulting in a conclusion that the symmetry relation, Eq, (2.12), is violated in this regime, see for example Figure 5.11 in range $0.3 \leq E \leq 2.1$.

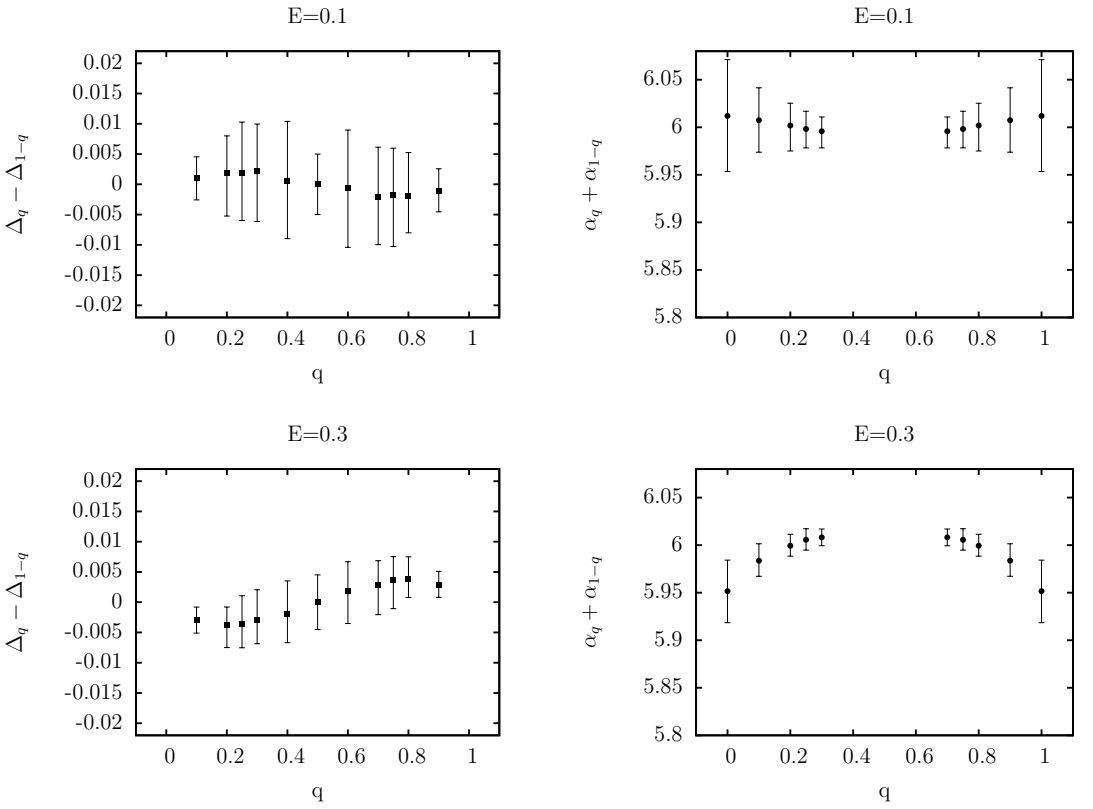

Continued on next page

Continued from previous page

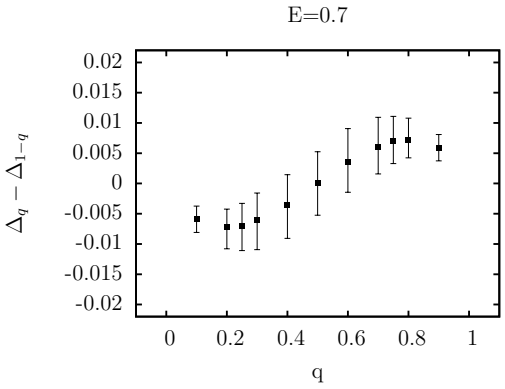

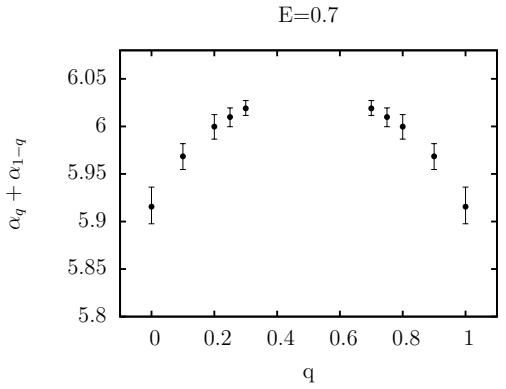

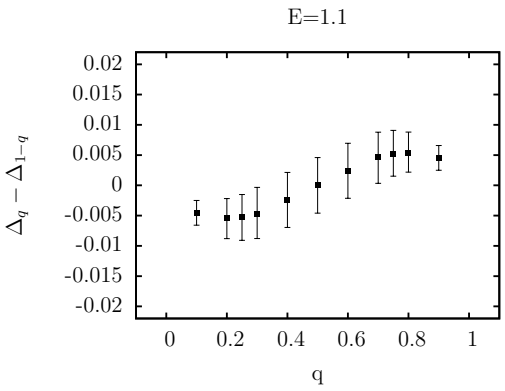

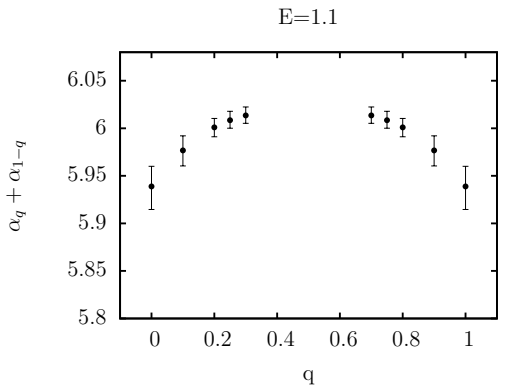

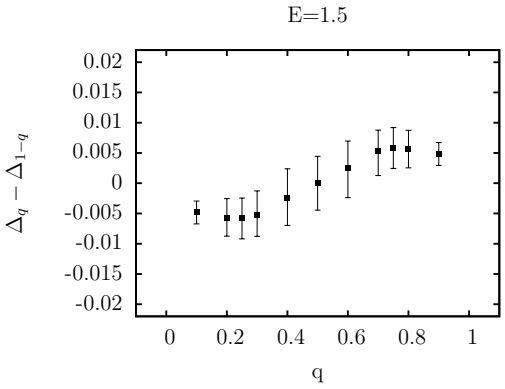

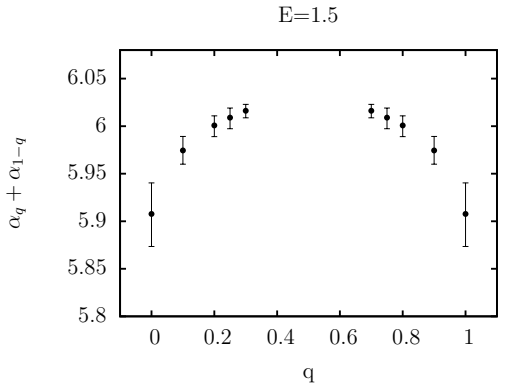

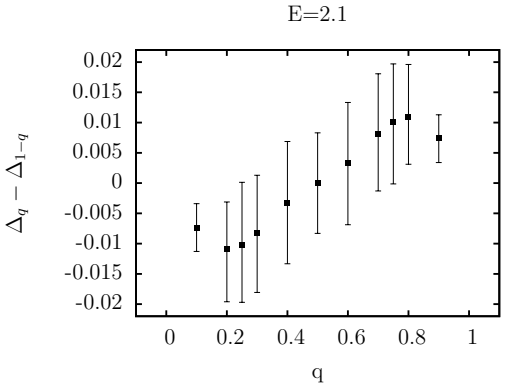

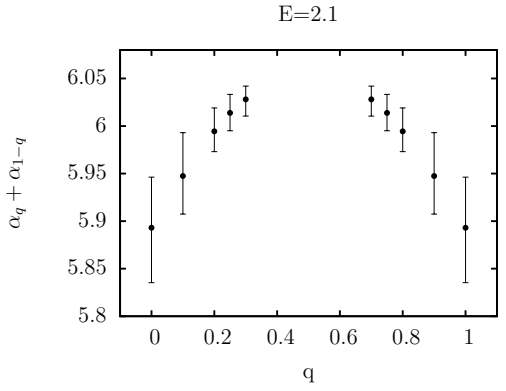

Continued on next page

Continued from previous page

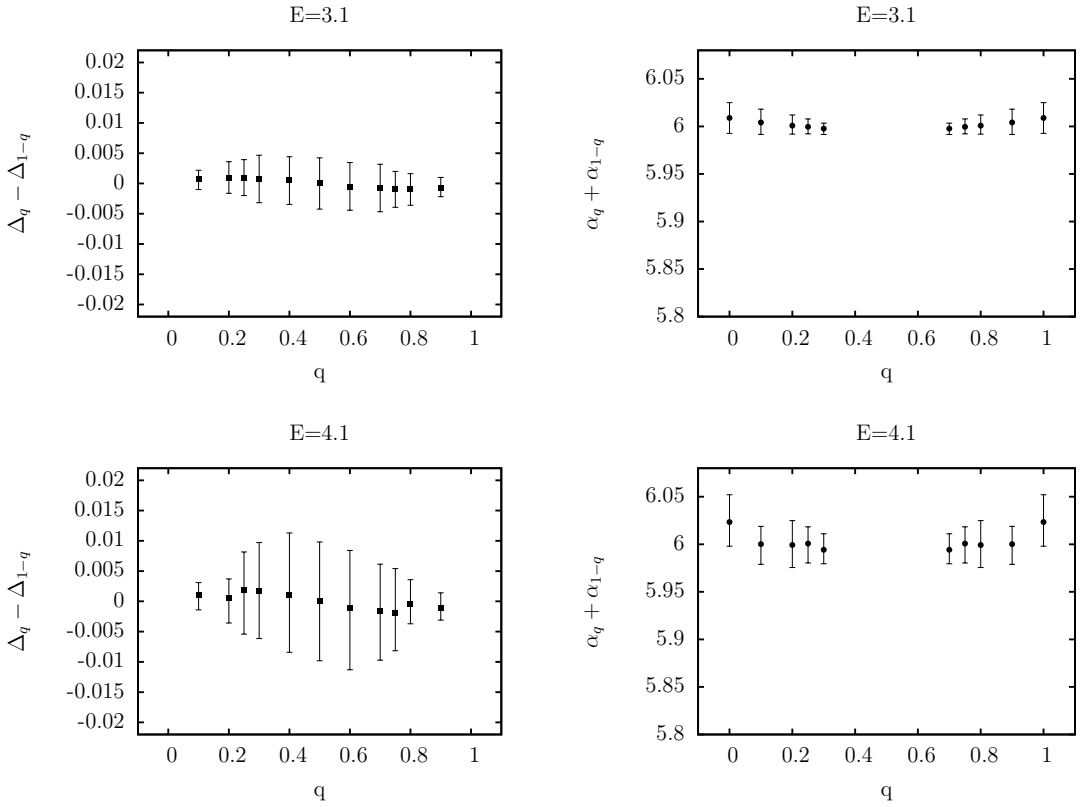

Figure 5.11: Symmetry relation of Δ_q (left column) and α_q (right column) of the 3D quantum percolation model at different energies. Error bars are 95% confidence levels. Points are naturally symmetric (antisymmetric) for $q = 0.5$ for Δ_q (α_q) because of the subtraction (addition) of terms corresponding to q and $1 - q$.

The non-universality of D_q and α_q would automatically imply the non-universality of τ_q, as well. On the other hand with a Legendre-transform for τ_q, $f(\alpha)$ can be obtained, describing the scaling of the probability distribution of the wave-function amplitudes. This distribution should be universal, therefore $f(\alpha)$ should be universal, too. From the α_q and D_q exponents presented in Figure 5.10(a) and (b) we computed the $f(\alpha)$ curve using Eq. 2.10, which is depicted in Figure 5.12. The values from different regimes of the mobility edge seem to form a unique curve, but this is mostly due to the scale on the axis. The upper inset of Figure 5.12 shows significant differences between data points at different energies. The approximate shape of the curve is a parabola, however, a quartic curve fits the data points slightly better.

According to Eq. (2.10) $q = 1$ corresponds to the fixed point of the $f(\alpha)$ function, $f(\alpha_1) = \alpha_1$. For different values of p_c^Q the exponent α_1 is not unique, leading to a linear regime of the $f(\alpha)$ function, see the lower inset of Figure 5.12. This makes the whole Legendre-transformation difficult, since it needs strict convexity. Conversely an $f(\alpha)$ that is not strictly convex would lead to ill-defined τ_q, D_q and α_q, like in our case, which contradicts universality again. A possible resolution of this contradiction could be that

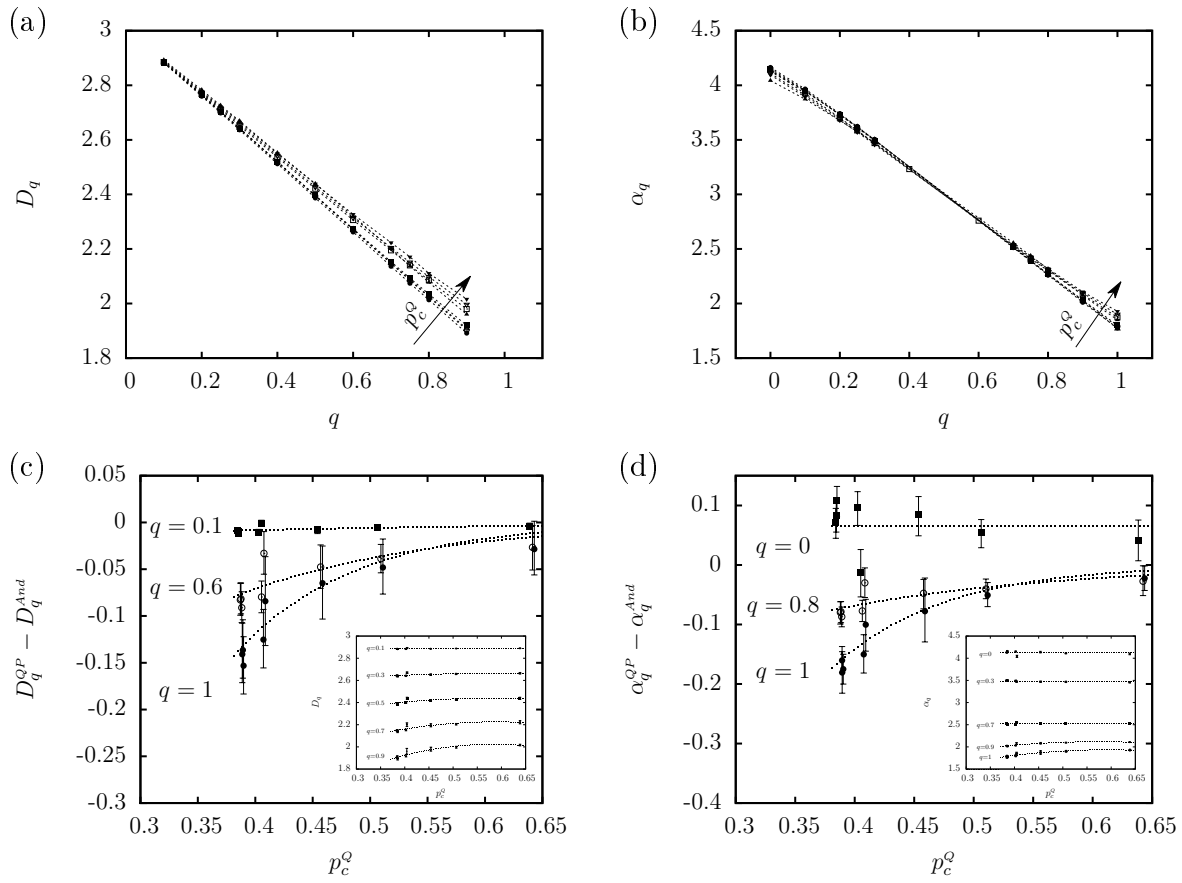

Figure 5.10: First row: (a) D_q (b) α_q as a function of q at different energies, E. Second row: MFEs shifted by their value for the Anderson model, (a) $D_q^{QP} - D_q^{And}$ (b) $\alpha_q^{QP} - \alpha_q^{And}$ as a function of p_c^Q at different q values. Dotted lines are guides for the eye, error bars represent a 95% confidence band on (c) and (d). Insets are the same, but without the shift.

our result for the MFEs is just simply not complete, perhaps a p-dependent phenomenon has not been taken into account affecting the results. Since the problem appeared at the bottom of the mobility edge, closest to the classical percolation threshold, one possible candidate for such phenomenon is the existence of an additional length scale, namely the correlation length of the classical percolation. In order to test it we added this length scale to the fitting function leading to a 3-variable function with number of fit parameters $\sim n_{rel}^3$, but we could not fit so many parameters to our dataset. There is only a small difference between the values of the MFEs for the quantum percolation model and for the orthogonal Anderson model, see Figure 5.10, and the symmetry relation (2.12) is almost valid within the error bar at the bottom of the mobility edge, too, see Figure 5.11. Therefore another explanation would be that somehow we underestimated the error bars of the MFEs. In the $p \to 1$ limit, our exponents seem to be close to their value for the orthogonal Anderson model, that together with our former claim in the Section 5.4.2 saying that quantum percolation belongs to the chiral orthogonal Anderson class, corroborate this possibility further. We believe that there is a unique and universal

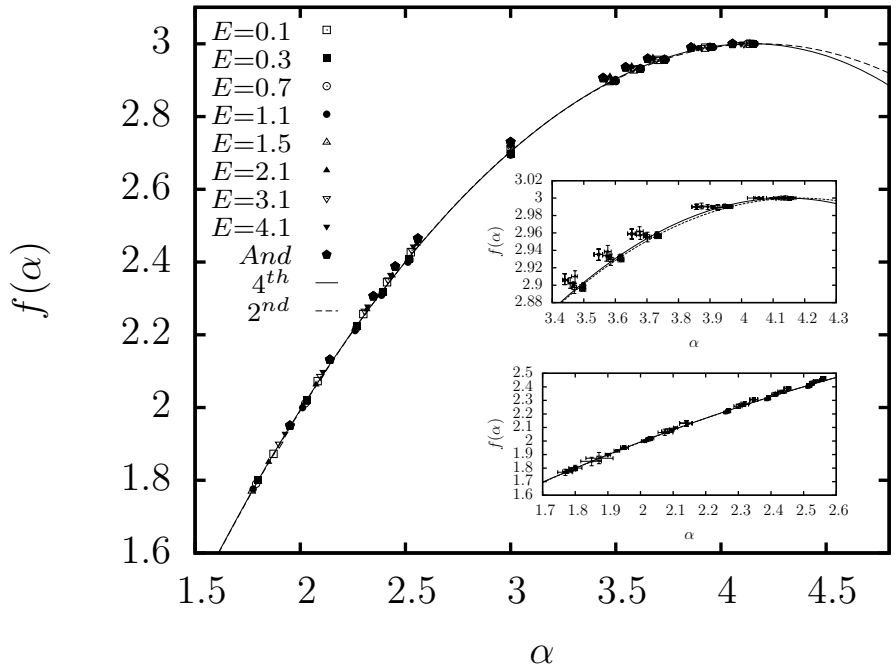

Figure 5.12: $f(\alpha)$ obtained from D_q and α_q computed at different energies, meaning different p_c^Q. Pentagons are the results for the Anderson model, solid line is a 4th order polynomial, dashed line is a 2nd order polynomial. Insets are magnified parts of the curve.

D_q, α_q and $f(\alpha)$ curve for the quantum percolation model, and it is identical with the one for the orthogonal Anderson model that fulfills the symmetry relation (2.12).

As a conclusion the present coherent set of data with a coherent technology in deriving multifractal exponents fulfill our expectations for larger values of $p_c^Q \geq 0.5$ but unfortunately unexpected deviations occur for lower values, i.e. $p_c^Q \leq 0.5$.

5.6 Summary

In this chapter we have numerically investigated the quantum percolation model in 3D, and discussed its non-trivial DOS along with the role of chirality. In order to describe the localization transition we used the MFSS method described in Section4.6, and we found q-independent results. We numerically determined the mobility edge of the system, confirming previous calculations. We also gave an explanation for the behavior of the mobility edge near $E = 0$ and at high energy. For the critical exponent we got energy-independent values within 95% confidence level. The average of these values is the same as the critical exponent of the orthogonal Anderson model, implying that quantum percolation belongs to the chiral orthogonal Anderson universality class. We also determined the MFEs D_q and α_q along the mobility edge, and for larger values of p_c^Q we found no significant difference from the Anderson model confirming the statement of the universality class further. In this regime the symmetry relation (2.12) is fulfilled. On

the other hand in the case of lower $p_c^{\mathcal{Q}}$ regime the exponents started to deviate violating universality and (2.12), probably caused by some unexpected p-dependent phenomenon. This behavior deserves further attention.

Chapter 6

Anderson localization at large disorder

6.1 Introduction

In the present chapter we investigate the properties of the eigenstates of the orthogonal Anderson-model, defined in Eq. (1.1), close to the band-edge in the strongly localized regime, $W \gg W_c$. The spatial extent of the eigenstates is commonly characterized by the inverse participation ratio (IPR), R_2 [5, 60],

$$R_2 = \sum_{i=1}^{N} |\Psi_i|^4 \quad . \tag{6.1}$$

This is equivalent to the definition in Eq. 2.6 at $\ell = 1$. For a state extending homogeneously over k sites $R_2 = k^{-1}$, thus $1/R_2$ tells us the effective number of sites a state extends to, hence the name. A state localized on one single site would give $R_2 = 1$, but extending over the whole system of size N, $R_2 = 1/N$. Therefore any states will have an R_2 value between these two cases, $1/N < R_2 < 1$. In summary the R_2, is a measure of localization, its inverse a measure of extension.

For strong disorder the states are expected to extend over a few sites only, therefore one expects IPR values typically of the order of $R_2 \approx 1$, hence finite size effects will not disturb our numerical simulations and in addition relatively small systems can be used. We employed periodic boundary conditions, and linear system sizes $L = 512$ in $d = 1$, $L = 20$ in $d = 2$ and $L = 8$ in $d = 3$. We computed the eigenvalues and the eigenvectors of the Hamiltonian Eq. (1.1), and the IPR for every state. We made statistical averaging over $M = 12500$ realizations, the results of the one dimensional (1D) case are shown in Figure 6.1 for disorder strength $W = 32$. In Figure 6.1(a) it is shown that the dots are distributed symmetrically around the band center, $E = 0$, due to $E \leftrightarrow -E$ exchange symmetry on average. In Figure 6.1 we may also see that the distribution of the IPR is broad but many of the states seem to have values close to unity, $R_2 \approx 1$, and there is a considerable amount of them around $R_2 = 1/2$, as well. As a function of energy we can see that moving away from the band-center the average IPR, $\langle R_2 \rangle$, first increases in accordance with our expectation of increasing localization towards the band edge. However, beyond a certain energy to be discussed later,

$$E_0 = \sqrt{1 + \left(\frac{W}{2}\right)^2} \quad , \tag{6.2}$$

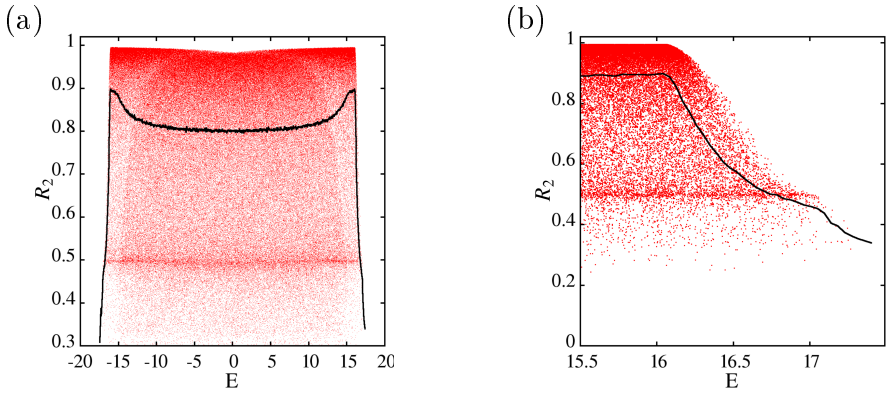

Figure 6.1: (a) IPR of the states as a function of energy for $W = 32$. The red dots correspond to the states, the black curve is the average. (b) The same as (a) but zoomed to the band edge.

the average IPR decreases again, even though the localization length (not shown here) should further increase undisturbed over this energy scale. This phenomenon has been recently noticed and presented in Ref. [61]. This means that at the band edge the effective size of a state becomes larger, even if the localization length decreases. Our main aim in this chapter is to understand and give an analytic explanation for the behavior of Figure 6.1 especially its part (b), showing an empty region of the IPR for large value of the energy together with a decrease of the average IPR, $\langle R_2 \rangle$.

A qualitative explanation of the existence of this region is as follows. If the energy of an eigenstate is bigger than $W/2$ then it must extend at least over two sites, because the on-site energies are bounded by $|\varepsilon| \leq W/2$, hence for large energies beyond the potential energy the states should have some additional kinetic energy which can be obtained by allowing their extension over more than one site. This is the reason why close to the band edge the states become more extended and hence the IPR has an upper bound. A similar argument can be found in [61].

In order to understand the behavior of the sates at large disorder, first we have to start with the asymptotic behavior, i.e. as $W \to \infty$. In that limit all the states are localized to a single site and hopping, i.e. kinetic energy, plays no role. In this case the system is a kind of sum of independent sites, therefore from the point of view of a probabilistic description, it is enough to take into account just one site with a random on-site energy and one electron on it. The probability distribution for E and IPR of this one-site system is the same as for a large system due to the independence of sites. The energy is just the random potential energy, thus the model gives us a W wide band, which is very close to reality (see Figure 6.1), for large enough disorder. Since every state is localized to one site, for every state $R_2 = 1$ and that also becomes a increasingly better approximation as W increases. But as mentioned above, for finite disorder there is an interesting inner structure in the figures that this one-site model cannot capture. Thus we tried to find a better model. For large enough W the states are strongly localized and extend over a few sites, which can be seen in Figure 6.1. For example at $W = 32$ most of the IPRs are larger than $1/2$, in other words most of the states extend approximately over two sites, so a two- or three-site model should be enough - at least qualitatively - to describe this strongly localized system.

6.2 The two-site model

As mentioned above, an improvement to the asymptotic, large disorder limit where the one-site model works, is the so-called two-site model. We show here that it gives us the main physics of Anderson model at large disorder. For such a model the Hamiltonian reads as

$$\mathcal{H} = \begin{pmatrix} \varepsilon_1 & -1 \\ -1 & \varepsilon_2 \end{pmatrix} \quad , \tag{6.3}$$

where ε_1 and ε_2 are uncorrelated random numbers drawn with uniform distribution, $p(\varepsilon_1, \varepsilon_2) = W^{-2}$ from the interval $[-\frac{W}{2}, \frac{W}{2}]$. Consequently the support of the probability distribution is a square, which is shown in Figure 6.2(a).

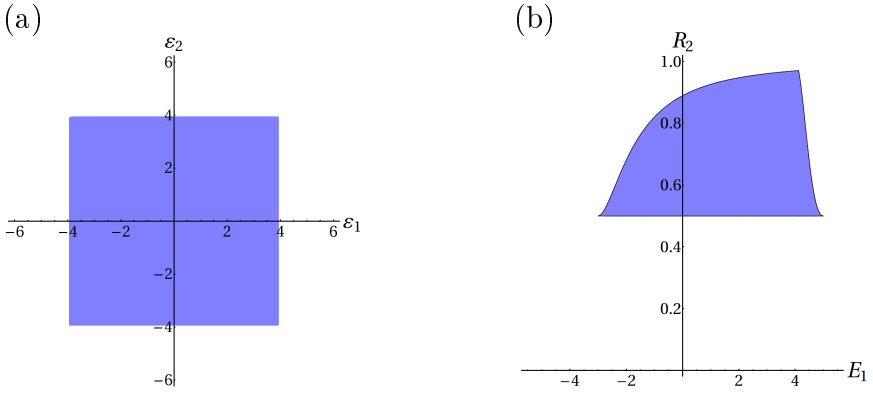

Figure 6.2: The domain of (a): $p(\varepsilon_1, \varepsilon_2)$, (b): $p(E_1, I)$ for $W = 8$.

The eigenvalues and the unnormalized eigenvectors of the Hamiltonian (6.3) are

$$E_{1,2} = \frac{\varepsilon_1 + \varepsilon_2}{2} \pm \sqrt{1 + \left(\frac{\varepsilon_1 - \varepsilon_2}{2}\right)^2} \quad , \tag{6.4}$$

$$v_{1,2} = \begin{pmatrix} -\frac{\varepsilon_1 - \varepsilon_2}{2} \mp \sqrt{1 + \left(\frac{\varepsilon_1 - \varepsilon_2}{2}\right)^2} \\ 1 \end{pmatrix} \quad . \tag{6.5}$$

Changing ε_1 and ε_2 to new variables, $t = \frac{1}{2}(\varepsilon_1 + \varepsilon_2)$ and $u = \frac{1}{2}(\varepsilon_1 - \varepsilon_2)$, the probability distribution function is still constant, but on a square rotated with 45°, $p(t, u) = 2/W^2$. Using these transformed variables the eigenenergies and the IPRs can be writen the following way

$$E_{1,2} = t \pm \sqrt{1 + u^2} \quad , \tag{6.6}$$

$$R_2 = \frac{1 + 2u^2}{2 + 2u^2} \quad . \tag{6.7}$$

At this point we take the larger eigenvalue, E_1, and express t with E_1 and u, and then express u using R_2. After these two transformations the probability density function of E_1 and R_2 become

$$p(E_1, R_2) = \frac{2}{W^2} \frac{1}{\sqrt{2(1 - 2R_2)(R_2 - 1)^3}} \quad , \tag{6.8}$$

whose support is quite non trivial:

$$\frac{1}{2} \leq R_2 \leq 1 - \frac{1}{2}\left(1 + \left[\frac{\left(E_1 + \frac{W}{2}\right)^2 - 1}{W + 2E_1}\right]^2\right)^{-1} \tag{6.9}$$

if $-\frac{W}{2} + 1 \leq E_1 \leq E_0$ and

$$\frac{1}{2} \leq R_2 \leq 1 - \frac{1}{2}\left(1 + \left[\frac{\left(E_1 - \frac{W}{2}\right)^2 - 1}{W - 2E_1}\right]^2\right)^{-1} \tag{6.10}$$

if $E_0 \leq E_1 \leq 1 + \frac{W}{2}$ using E_0 the energy border defined in Eq. (6.2) and appearing in Figure 6.1. This domain is shown in Figure 6.2(b).

The probability distribution function $p(E_1, R_2)$ is obtained for the larger eigenvalue, E_1. For the smaller eigenvalue, E_2 the result is identical, except E_1 must be replaced by $-E_2$. Thus the probability density function describing the whole system is $p(E, R_2) = p(E_1, R_2) + p(E_2, R_2) = p(E_1, R_2) + p(-E_1, R_2)$, which is shown in Figure 6.3(a). If we compare this analytic function to Figure 6.3(b), the probability density function obtained numerically on a system with linear size $L = 512$, the qualitative similarity is obvious. In Figure 6.1 one can clearly see that the function is symmetric, and it is a sum of two components. In our case these two components are the two eigenvalues. This simple two-site model also explains the behavior of the IPR as a function of energy close to the band-edge. Eq.(6.10) is responsible for the decrease of the IPR depicted on the right side of Figure 6.2(b). Another feature of the two-site model is the peak in $p(E, R_2)$ at $R_2 \approx 1/2$. However, there are some differences between the model and the numerical results. First of all in a two site model $R_2 \geq 1/2$, because the state can extend maximum to two sites, but in a bigger system there exist a few states extending over more than two sites. Therefore in the low-R_2 regime the two-site model naturally underestimates the reality. Nevertheless both distributions are normalized, therefore if somewhere there is an underestimation, elsewhere there must be an overestimation, which gives us the hump at high R_2 values in Figure 6.3(c). Looking at Figure 6.3(d) it is clear that the two-site model captures very well the shape of the domain of definition for the two components, we see a little overestimation for high values of the IPR. From $p(E, R_2)$ we calculated the average of IPR, $\langle R_2 \rangle$ as a function of the energy, E, which can be seen in Figure 6.5(b). The analytic curve shows a qualitative agreement with the numerical function: moving away from the band-center we see an increase in $\langle R_2 \rangle$, and beyond E_0 it decreases, showing a little shoulder. Quantitatively in the band-center the model overestimates $\langle R_2 \rangle$, but in the decreasing regime the two site model becomes a good approximation (see the inset of Figure 6.5(b). In addition the two-site model has a band of $\left[-\frac{W}{2} - 1, \frac{W}{2} + 1\right]$ but obviously the real band extends beyond these limits.

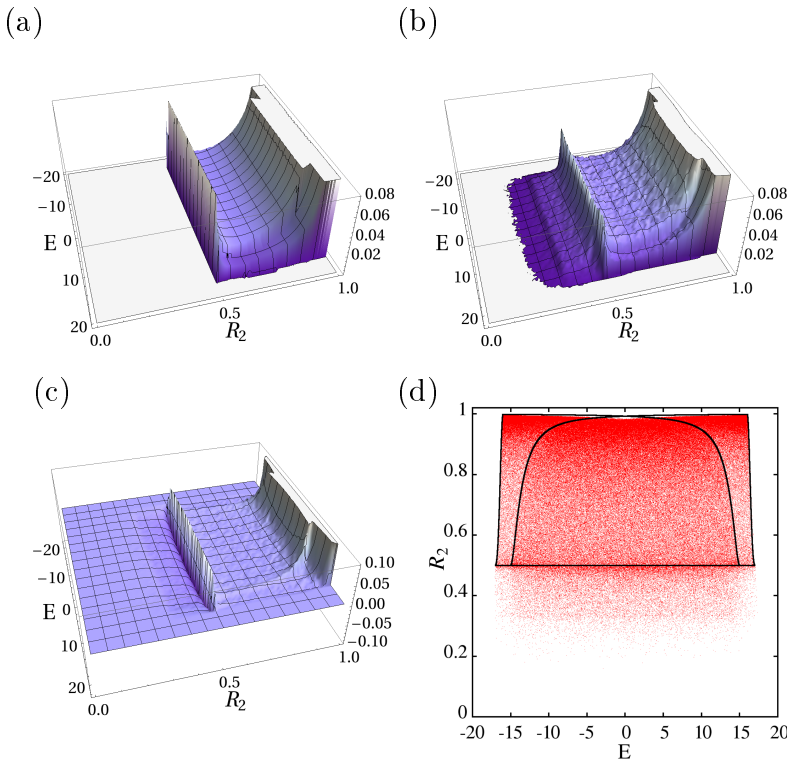

Figure 6.3: $p(E, R_2)$ (a) The analytic result of the two-site model, (b) numerical result for system size $L = 512$, (c) the difference between (a) and (b). (d) Red points are the numerically obtained E and R_2 values at system size $L = 512$, black curve is the domain of the two eigenstate in the framework of the two-site model.

6.3 The three-site model

The two-site model introduced in Section 6.2 seems to give a qualitatively correct explanation for the numerically obtained distributions but as pointed out there are deficiencies. In the present subsection we outline the generalization of this model to a three-site model, and we investigate how the results change. The Hamiltonian incorporating three-sites reads as

$$\mathcal{H} = \begin{pmatrix} \varepsilon_1 & -1 & 0 \\ -1 & \varepsilon_2 & -1 \\ 0 & -1 & \varepsilon_3 \end{pmatrix} \tag{6.11}$$

In the three-site model the domain of the probability density function is a cube (see Figure 6.4(a)), and the function is constant, $p(\varepsilon_1, \varepsilon_2, \varepsilon_3) = W^{-3}$. As in the two-site model, the eigenvectors and IPRs should not depend on the average energy, therefore it seems helpful to introduce new variables: $\varepsilon_1 = t + u$, $\varepsilon_2 = t + v$, $\varepsilon_3 = t - u - v$. This transformation changes the domain to a parallelepiped, and the probability density function remains constant, because the transformation is linear, $p(t, u, v) = 3/W^3$. It is easy and straightforward to compute the eigenvalues and eigenvectors of Eq. (6.11), but the expressions are very long, so we do not list here the exact expression, instead we only present their support. Every eigenvalue has the form $E_i = t + \chi_i(u, v)$, with $i = 1, 2, 3$. Similarly to the two-site case, the size of the eigenvectors, i.e. the IPRs

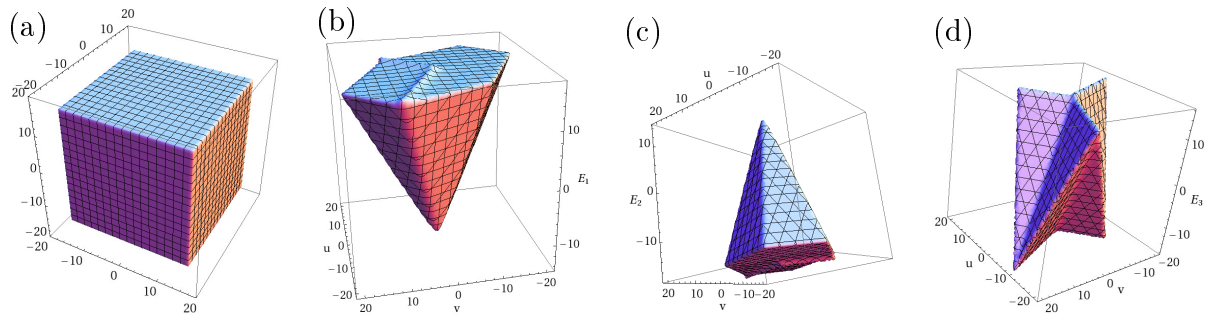

Figure 6.4: The domain of definition for variables (a) $\varepsilon_1, \varepsilon_2, \varepsilon_3$ (b) E_1, u, v (c) E_2, u, v (d) E_3, u, v in a three-site model.

depend on u and v only, $R_2(u, v)$. Picking one of the eigenvalues the problem can be transformed to the variables E_i, u and v. The probability density function remains constant, $p(E_i, u, v) = 3/W^3$. The difficult part of the problem is that the domain changes to a very complicated object, which is shown in Figure 6.4(b)(c) and (d) for E_1, E_2 and E_3. To compute $p(E_i, R_2)$ one has to express u as a function of R_2 and v, then calculate the new domain and then integrate over v.

This resulted in a difficult task analytically because the expressions of the IPRs are very complicated. Instead we performed our calculation based on $p(E_i, u, v) = 3/W^3$ using a Monte Carlo integration over the domains depicted in Figure 6.4(b),(c) and (d). The result is given in Figure 6.5(b).

In view of Figure 6.5(b) it is clear that the three-site model gives a quantitatively better approximation of a large system, especially approaching the edge of the band (see the inset), but qualitatively the main behavior is captured already by the two-site model.

6.4 Higher dimensions and summary

Generalization of our results to higher dimensions, $d = 2, 3$ and their comparisons to the numerical simulations are presented in Figure 6.5. There is a striking similarity between the figures which is due to the fact that the strongly localized regime is effectively zero dimensional, i.e. as $W \to \infty$ the states become localized over a few sites only. The major difference is that the line separating the two components becomes less sharp with increasing dimensionality. In one dimension this line can be seen very clearly, in $d = 2$ it is still visible, but in $d = 3$ it becomes hardly visible.

To summarize we have shown that the Anderson-model at strong localization shows interesting behavior especially approaching the band-edge. As already known the states become more and more localized as energy increases from the band-center towards the band-edge, i.e. the inverse localization length of the states increases as a function of energy. The IPR, on the other hand, increases up to a critical energy, E_0 (6.2). Beyond this limit the effective extension of the states can be described by a multi-site (2-site or 3-site) model because in case the eigenenergy becomes larger than this critical energy, $E > E_0$, some kinetic (hopping) energy is needed besides the random potential energy yielding in an upper bound of the IPR which in turn results in a decrease of the average

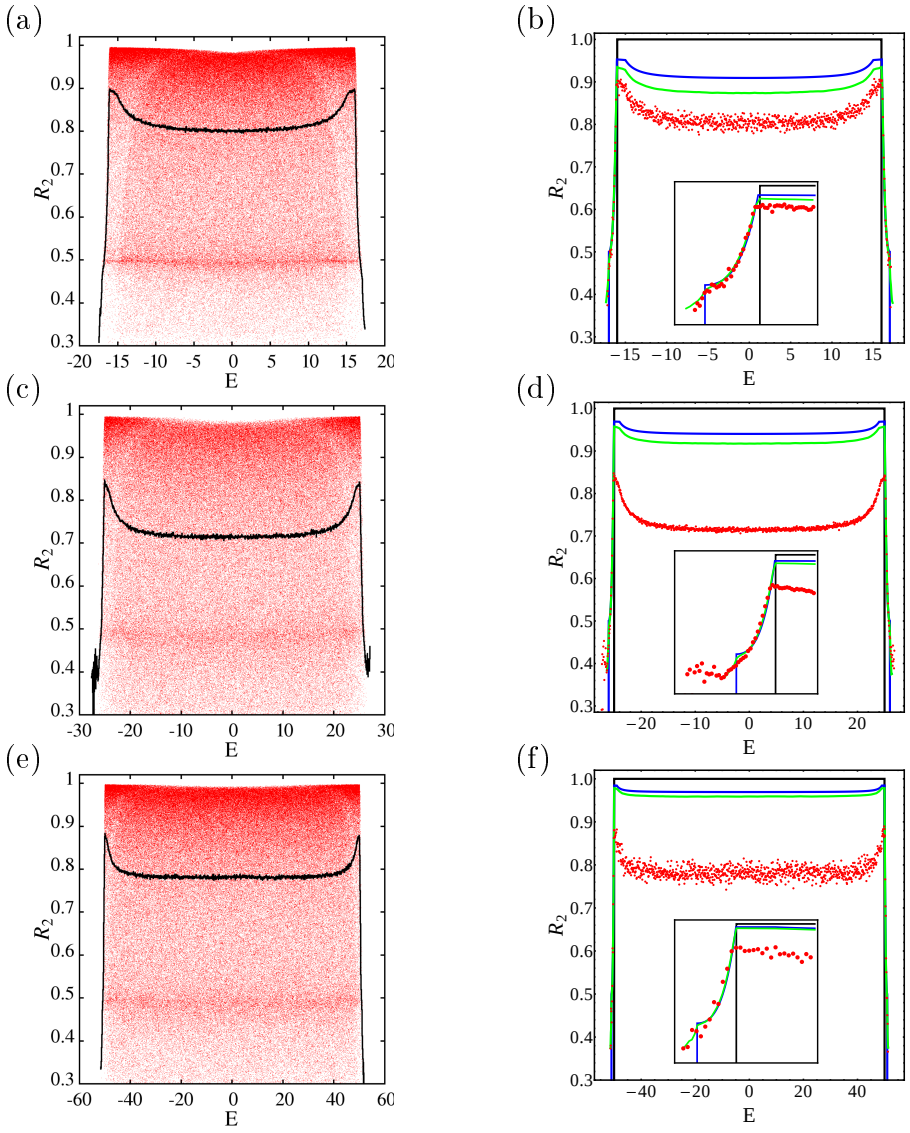

Figure 6.5: Left side: IPR as a function of energy (a) in $d = 1$ with $L = 512$ for $W = 32$, (c) in $d = 2$ with $L = 20$ for $W = 50$, (e) in $d = 3$ with $L = 8$ for $W = 100$. Red dots correspond to single states, black curve is the average. Right side: R_2 as the function of energy (b) in $d = 1$, (d) in $d = 2$, (e) in $d = 3$. Dots correspond to the numerically obtained average curve for a big system, black curve corresponds to the one-site model, blue to the two-site model, and green to the three-site model. Insets are the same, but zoomed to the left band edge.

IPR, $\langle R_2 \rangle$ as a function of energy in this regime. In order to understand the numerical simulations we introduced a few-site model and solved analytically capturing the main physics of the problem.

In Ref. [61] it is argued that the behavior explained in the present work is attributed to the crossover towards resonant states similar to the effect produced by the Lifshitz-tail (see Section 1.2). It would be interesting to find the relation between our results and the resonant states.

Chapter 7

Anderson transition and multifractals in the spectrum of the Dirac operator of Quantum chromodynamics at high temperature

7.1 Introduction

Several recent works show that there is an Anderson transition in the spectrum of the Dirac operator of Quantum chromodynamics (QCD) [62, 63, 64, 65]. These works used mainly spectral statistics to characterize the transition, our goal in this chapter is to investigate eigenvectors through GMFEs. We show that MFSS works for this problem, implying multifractality of the eigenvectors at the critical point. Moreover the estimated MFEs are compatible with the ones for the corresponding Anderson model confirming that this transition is really an Anderson transition.

QCD is the theoretical description of strong interaction. It contains 6 flavors of quarks (fermions), which build up hadronic matter, and carry 3 possible color charge. Gluons (bosons) are mediating the strong interaction, and they carry color charge also. Due to exact SU(3) symmetry in color space, the theory is an SU(3) gauge theory. An interesting feature of QCD is that it behaves completely different at low and high temperature. At low temperature anti-screening is present, because beside quarks, gluons also have color charge. This leads to confinement, which makes impossible to observe a single quark. At high temperature the coupling constant, g, decreases, leading to asymptotic freedom of the quarks, the matter forms in this regime a quark-gluon plasma. In between, at temperature T_c, there is a crossover from one state to the other.

Let us denote the quark fields by ψ (flavor and color indexes are left for simplicity), the color vector potential by A_μ, and the field strength, expressible from A_μ, by $F_{\mu\nu}$. Introducing the inverse temperature, $\beta = 1/T$ as imaginary time, $\beta = it$, the partition function has the fallowing form:

$$Z = \mathrm{Tr}\left(e^{-\beta H}\right) = \int \mathcal{D}\bar{\psi}\mathcal{D}\psi\mathcal{D}A\; e^{-S_E[\bar{\psi},\psi,A]}, \tag{7.1}$$

where $\mathcal{D}\bar{\psi}$, $\mathcal{D}\psi$ and $\mathcal{D}A$ denote path integrals, and S_E is the Euclidean action, $S_E =$

$\int d^4x \mathcal{L}_E$. The Euclidean Langrangian of QCD has the following form:

$$\mathcal{L}_E = \underbrace{\sum_f \bar{\psi}_f \left(\gamma_\mu(\partial_\mu + igA_\mu) + m_f\right)\psi_f}_{\mathcal{L}_E^{quark}} + \underbrace{\frac{1}{4}\mathrm{Tr}\left(F_{\mu\nu}F^{\mu\nu}\right)}_{\mathcal{L}_E^{gauge}}, \tag{7.2}$$

The first term in Eq.(7.2) describes the quarks, f is an index for different flavors, the second term describes the gauge field. The operator between the quark fields (without the mass term) is the Dirac operator [66],

$$D = \gamma_\mu(\partial_\mu + igA_\mu), \tag{7.3}$$

which will be investigated in this chapter. Since quarks are fermions, they are Grassmann-valued, hence the quark terms in the partition function can be written as

$$Z_f = \int \mathcal{D}\bar{\psi}\mathcal{D}\psi \; e^{-\bar{\psi}\left(D(A)+m_f\right)\psi} = \det\left(D(A) + m_f\right) \; , \tag{7.4}$$

leading to

$$Z = \int \mathcal{D}A \prod_f \det(D(A) + m_f) e^{-S_E^{gauge}[A]} \; . \tag{7.5}$$

7.2 Spectral properties of the Dirac operator

Our aim in this chapter is to investigate the properties of the eigenvectors of the Dirac operator, describing quark modes. The Dirac operator plays an important role, because the quark Green's function between spacetime points x and x' is the matrix element of the inverse of the Dirac operator corresponding x and x'. The low-energy eigenmodes are dominant in this respect, therefore it is important to know their nature.

To be clear about the structure of the Dirac operator, defined in Eq.(7.3), we would like to note that the Euclidean γ matrices satisfy the relations

$$\{\gamma_\mu, \gamma_\nu\} = 2\delta_{\mu\nu} \qquad \gamma_5 = \gamma_1\gamma_2\gamma_3\gamma_4 = \begin{pmatrix} 1 & 0 & 0 & 0 \\ 0 & 1 & 0 & 0 \\ 0 & 0 & -1 & 0 \\ 0 & 0 & 0 & -1 \end{pmatrix}. \tag{7.6}$$

The Dirac operator is an anti-hermitian and chiral operator, because the following equations hold:

$$D = -D^\dagger \qquad \{\gamma_5, D\} = 0 \qquad \gamma_5^\dagger\gamma_5 = \gamma_5^2 = I. \tag{7.7}$$

Therefore it has the following structure:

$$D = \begin{pmatrix} 0 & iW \\ iW^\dagger & 0 \end{pmatrix}. \tag{7.8}$$

W is a complex matrix with no further symmetry [66], thus according to Section 1.3, the system should belong to the chiral unitary class. Due to anti-hermiticity the Dirac

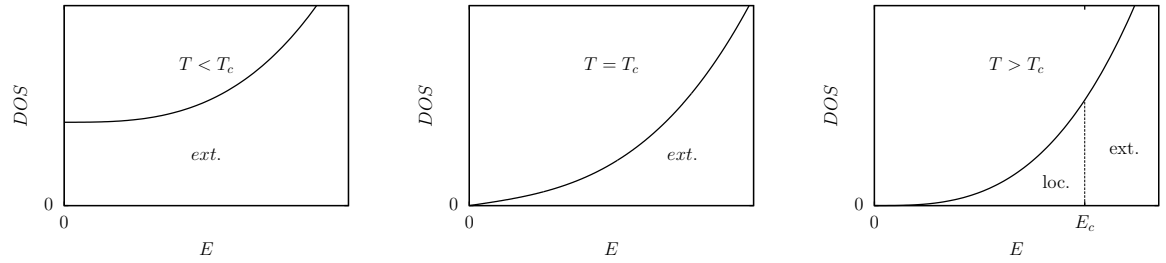

Figure 7.1: Schematic figure of the density of states of the Dirac operator at different temperatures.

operator has purely imaginary eigenvalues, iE_n, chirality leads to eigenvalue pairs $iE_n \leftrightarrow -iE_n$. Therefore we use only the magnitude, E_n, and we investigate the $E \geq 0$ regime.

Figure 7.1 shows how the Density of states, i.e. the probability density function of eigenvalue magnitudes, E_n, changes with growing temperature. At low temperature, when confinement is present, the eigenmodes of the Dirac operator are extended. In this regime eigenvalue correlations obey random matrix statistics with level repulsion, and the DOS is nonzero at zero energy. Increasing the temperature to T_c a pseudogap opens in the DOS. Increasing the temperature above T_c, a critical energy appears, which moves to higher energies with increasing temperature. Recent studies show that above T_c quarks with small energy are localized, having Poisson spectral correlations, while quarks at large energy are extended, having Wigner-Dyson statistics [62, 64, 65]. An example how the eigenvectors change with energy is given in Figure 7.2. In Ref. [65] the authors performed finite-size scaling for an order parameter derived from the nearest neighbor level spacing distribution. For fixed temperature they found a sharp transition as a function of energy between the two limiting cases (Poisson an Wigner-Dyson), with a critical exponent compatible with the three-dimensional unitary Anderson model. For fixed temperature E_c seems to be a real critical point, where an Anderson-transition occurs. Our goal is to investigate this transition through the eigenvectors instead of eigenvalues, and see whether multifractality is present at E_c or not. Therefore temperature is fixed to $T \approx 2.6T_c$ as written in Section 7.3. In Ref. [64] the authors investigated also the temperature-dependence of the critical energy, $E_c(T)$, forming a mobility edge. They found that it reaches zero energy at a temperature compatible with the crossover temperature, T_c.

7.3 Numerical method

For our investigation we use numerical simulations for QCD, called Lattice QCD, which requires the discretization of Eq.(7.5) on a finite lattice. For a review of lattice QCD see, e.g., Ref. [67]. While the discretization of the gauge fields poses no particular problem, and can be performed preserving exact gauge invariance [68], fermion fields are known to be more problematic, and the discretization of the Dirac operator spoils some of the properties of its continuum counterpart. Nevertheless, the discretization that we employed, namely staggered fermions [69], preserves the anti-hermiticity and the symmetry of the spectrum with respect to the origin, and moreover preserves the chiral unitary symmetry

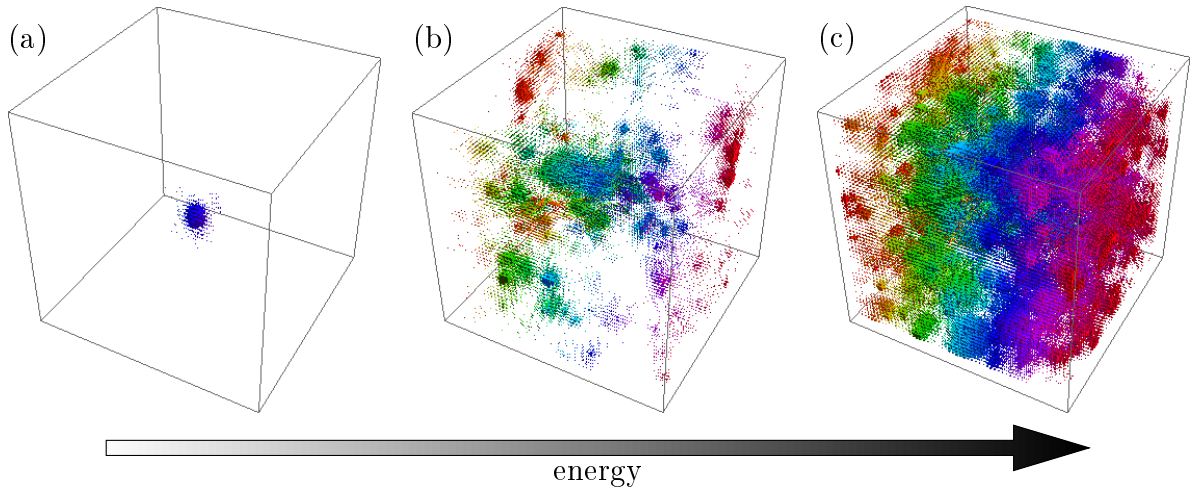

Figure 7.2: Eigenvectors of the Dirac operator of QCD at $T \approx 2.6T_c$ at (a) $E = 0.15$ in the insulating regime (b) $E = 0.3355$ near criticality (c) $E = 0.365$ in the metallic regime. Box sizes correspond to $A \cdot \sqrt{|\Psi|^2}$. Multiplying factor, A, was tuned to best sight for each subfigure. Spatial system size is $L = 56$ for all subfigures. Coloring is due to x coordinate.

class [66].

Let us now describe the numerical setting in some detail. QCD is discretized on a periodic hypercubic lattice, of spatial extent L in each direction and temporal extent L_t. The gauge fields A_μ are replaced by corresponding gauge links, i.e., parallel transporters along each link of the lattice, which are elements of the gauge group, $SU(3)$. The functional S_E^{gauge} is discretized and expressed in terms of the gauge links, and the integration over gauge fields is replaced by the integration with the Haar measure over gauge links, i.e., over the gauge-group valued variables on the links. Finally, the continuum Dirac operator is replaced by the staggered Dirac operator, which reads

$$D_{xy}^{\text{stag}} = \frac{1}{2} \sum_{\mu=1}^{4} \eta_\mu(x) \left[\delta_{x+\hat{\mu},y} U_\mu(x) - \delta_{x-\hat{\mu},y} U_\mu^\dagger(x-\hat{\mu}) \right] , \tag{7.9}$$

with $\eta_\mu(x) = (-1)^{\sum_{\nu<\mu} x_\nu}$, and $U_\mu(x) \in SU(3)$ the gauge link connecting the lattice site x to the neighboring site along direction $\hat{\mu}$. The staggered Dirac operator carries only spacetime and color indexes, i.e., it has no spinorial structure. The eigenvalue equation $D^{\text{stag}}\chi = iE\chi$ must be supplemented with the antiperiodic boundary condition in imaginary time direction, and to avoid surface effects we used periodic boundary condition in spatial directions.

The Dirac operator can be viewed as i times a random Hamiltonian, with disorder provided by the fluctuations of the gauge fields, and distributed according to the Boltzmann weight appearing in the partition function. In its discretized version, the Dirac operator is a large sparse matrix, with nonzero random elements only in the off-diagonal, nearest-neighbor hopping terms, which depend on the parallel transporter on the corresponding link of the lattice. This resembles an Anderson model with off-diagonal disorder,

although here the fluctuations of the gauge links are correlated, rather than independent. However, since the theory has a mass gap, correlations decrease exponentially with the distance. The size of the gauge field fluctuations are determined by the temperature, which therefore is expected to play the same role as the amount of disorder in the Anderson model. This is confirmed by the fact that the temperature governs the position of the mobility edge.

In this chapter we study the spectrum of the Dirac operator by generating gauge link configurations, i.e., realizations of disorder, by means of Monte-Carlo methods. Numerical calculations were done on a GPU cluster. In our simulations we have included only the three lightest flavors (up, down, and strange), with equal masses for the up and down quark, which is a good approximation of the real world for many purposes. Because of the fermion doubling problem with staggered quark fields we can simulate four degenerate fields at the same time, hence a fourth root has to be introduced for the determinant of the strange quark, and a square root for the up and down quarks leading to

$$Z_{2+1} = \int \mathcal{D}U \, \det{}^{\frac{1}{2}}(D(U) + m_{ud}) \det{}^{\frac{1}{4}}(D(U) + m_s) e^{-S_E^{gauge}[U]} \, . \tag{7.10}$$

The lattice spacing in physical units was set to $a = 0.125$ fm and the temporal size was fixed to $L_t = 4$, resulting in the temperature $T \approx 2.6\, T_c$, well above the crossover temperature (see Refs. [62, 63, 64, 65] for more details). Technical details about the numerical implementation and the scale-setting procedure can be found in Refs. [70, 71]. We have computed the eigenpairs of the Dirac operator from the smallest eigenvalue up to the upper end of the critical region, on lattices of spatial sizes in the range $L = 24 - 56$ (in lattice units). A detailed list is reported in Table 7.1 along with the corresponding number of samples.

The three-dimensional box probability, Eq.(2.4), required for the multifractal analysis, was constructed as follows. To have a gauge-invariant description we summed over the color components, labeled by c. Moreover, due to the strong correlation between the lattice time-slices, the eigenvectors of the Dirac operator look qualitatively the same on each of them, so we can also sum over the time-slices, t. The squared amplitude at site i, $|\Psi_i|^2$ is then defined as $|\Psi_i|^2 \equiv \sum_{t,c} |\chi^c_{i,t}|^2$, and provides the basic three-dimensional spatial probability distribution, from which the box probability distribution is then obtained in the usual way.

7.4 Correlations between eigenvectors

In this section we would like to investigate the correlations between different eigenvectors of an edge configuration. Our motivation is twofold: On one hand we want to compare the eigenvector correlations in QCD with the eigenvector correlations in the unitary Anderson model. On the other hand we also want to check how much the data, which we use in Section 7.5 for fitting, are correlated. Cuevas and Kravtsov showed for the Anderson model that there are non-negligible correlations between eigenvectors in a disordered system [26]. They investigated the density-density correlations, therefore let us define

system size (L)	number of samples
24	41517
28	20548
32	19250
36	14869
40	8812
44	5242
48	7008
56	3107

Table 7.1: System sizes and number of samples of the simulation for the Dirac operator of QCD.

the overlap integral of the ith and jth eigenfunctions:

$$K_2^{ij} = \int d^3r \, |\Psi_i|^2 \, |\Psi_j|^2 \tag{7.11}$$

If two states are localized to the same volume, the overlap integral is high, $K_2^{ij} \approx K_2^{ii} = R_2^i(\ell = 1)$ (cf. Eq (7.11) and (2.6)), while for two delocalized states $K_2^{ij} \approx 1/N$, where $N = L^3$ is the volume of the system. This quantity, and the energy difference of states will be in our main interest in this section, thus the joint probability distribution of these is important:

$$P(\omega, k) = \left\langle \sum_{i,j} \delta(E_i - E_j - \omega)\delta(K_2^{ij} - k) \right\rangle . \tag{7.12}$$

$P(\omega, k)d\omega dk$ is the probability that two randomly chosen eigenvectors have energy difference in the interval $[\omega, \omega + d\omega)$, and overlap integral in the interval $[k, k + dk)$. Let us introduce two more quantities:

$$K(\omega) = \int dk \; kP(\omega, k) = \left\langle \sum_{i,j} K_2^{ij} \delta(E_i - E_j - \omega) \right\rangle \tag{7.13}$$

$$R(\omega) = \int dk \; P(\omega, k) = \left\langle \sum_{i,j} \delta(E_i - E_j - \omega) \right\rangle . \tag{7.14}$$

The conditional distribution function of k has the form

$$P(k \mid \omega) = \frac{P(\omega, k)}{R(\omega)}, \tag{7.15}$$

which describes the probability distribution of k for a fixed energy difference, ω. To characterize the average behavior of the overlap integral as a function of energy, the conditional expectation value of k is the natural choice,

$$C(\omega) = \mathbb{E}_k(k \mid \omega) = \int dk \; \frac{kP(\omega, k)}{R(\omega)} = \frac{K(\omega)}{R(\omega)}. \tag{7.16}$$

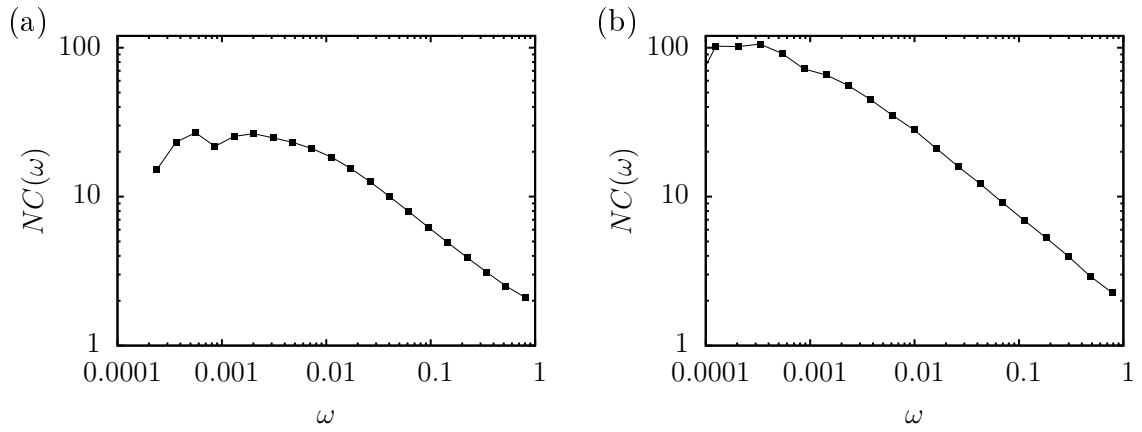

Figure 7.3: Correlations between the eigenfunctions of the unitary Anderson model at system size $L = 10$ (a) at criticality, $W = 18.37$ (b) in the localized phase, $W = 30$.

In the extended phase $C(\omega) \approx 1/N$, because $K_2^{ij} \approx 1/N$ in this regime. In the localized phase $C(\omega) \approx 1/N$ should hold again, because one expects localized states distributed independently over the sample, and the probability of that such localized states overlap is approximately ξ^3/N. Therefore $NC(\omega) \approx 1$ should hold for states in the metallic and insulating regime also. In contrast to this, Cuevas and Kravtsov found notable correlations for the orthogonal Anderson model deep in the insulating phase also by examining this quantity, $NC(\omega)$ [26]. Figure 7.3 shows the correlations for the unitary Anderson model at criticality and in the localized phase. One can see large enhancement of correlations at small ω in both cases, and decreasing behavior with growing energy separations, ω, similar to the results of Ref. [26]. According to Ref. [26] the reason behind this is that these exponentially localized states have a reminiscent multifractal-like texture.

By examining the correlations in QCD we find also an enhancement at small energy separations, see Figure 7.4. In the critical regime the behavior of the two systems is very similar, even the approximate exponent of the decay is close to 0.5 in both cases. Even though in the localized regime one can see an enhancement at small energy separations, and it shows mainly decreasing behavior, in Figure 7.4(b) a large hump is also visible around $\omega \approx 0.02$.

This suggests that there are eigenvectors separated in energy typically by $\omega \approx 0.02$, whose overlap integral is large. This behavior is visible in Figure 7.5(a), where $P(k \mid \omega)$, defined in Eq. (7.15), is depicted. As written above, the overlap integral depends on the nature of the states, therefore we compared this quantity to the inverse participation ratio of the corresponding states. We considered the overlap large, if the relation $K_2^{ij}/\sqrt{R_2^i R_2^j} \geq 0.8$ held. We divided the $C(\omega)$ function to two parts corresponding to eigenstate-pairs with large and small overlap: $C_(\omega) = C_L(\omega) + C_S(\omega)$. The line on Figure 7.5(a) shows $NC_L(\omega)$, which has a hump around $\omega \approx 0.02$, where $P(k \mid \omega)$ has non-vanishing probability at large k, showing largely overlapping eigenvectors separated by $\omega \approx 0.02$. The behavior of $C_S(\omega)$ is visible in Figure 7.5(b), where the hump is almost completely missing, and one can see a decreasing behavior with growing energy

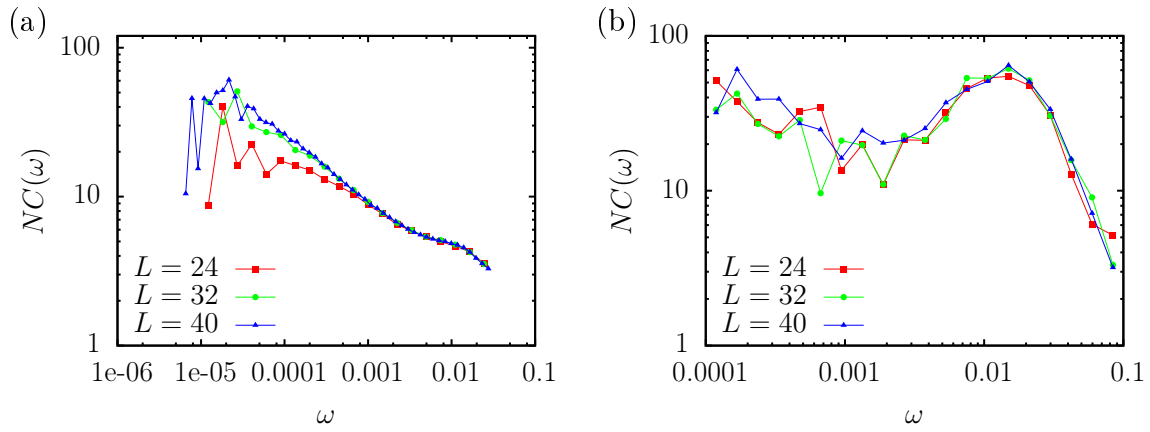

Figure 7.4: Correlations between the eigenfunctions of the Dirac operator of QCD (a) in the critical regime, $0.32 \leq E \leq 0.35$ (b) in the localized regime, $0.15 \leq E \leq 0.25$ for different systems sizes.

separation, ω.

We do not know the precise origin of the hump, but one possible explanation is the following: Because of the fermion doubling problem [62] we would simulate $2^4 = 16$ fermions on the our four-dimensional lattice. Using staggered fermions reduces this to 4, which means that we would simulate 4 degenerate fermions in the absence of the gauge field, i.e. with unity values on the edges. The gauge field breaks up the degeneracy, but on our scales for the lattice constant doublets of these fermions can still survive. We believe that the hump is caused by these doublets of states. We also experienced that large overlap was produced by two states in 95% of the cases, the rest can be accidental large overlap of three states. This phenomenon supports also the idea of doublets. Since the fermion doubling problem is the consequence of our discretization scheme of the continuum model, it has no physical effect. Therefore we believe that in the continuum limit $NC(\omega)$ should behave as $NC_S(\omega)$ in Figure 7.5(b), which shows the expected decreasing tendency.

7.5 MFSS for the eigenvectors of the Dirac operator

In this section we would like to characterize the Anderson phase transition in the spectrum of the Dirac operator of QCD (see Section 7.2) in the frame of and MFSS, see Section 3.2. As written in Section 7.3, a three-dimensional spatial probability distribution was calculated from the eigenvectors. From that the GMFEs $\tilde{\alpha}_q$ and $\tilde{D}_q$ were computed according to Eq. (2.14b) and (2.14c). In this case the only difference compared to these equations is that now „disorder strength" (gauge field coupling, g, determined by the temperature) is fixed, and we observe the transition as a function of energy, thus W should be replaced with E. An example of the resulting GMFEs at fixed $\lambda = 0.125$ is depicted in Figure 7.6. The curves shift to the opposite direction with growing system size on the different sides of the transition. At low energy they shift down, indicating a localized phase, while at high energy they shift up, suggesting a metallic phase, as expected. In between there

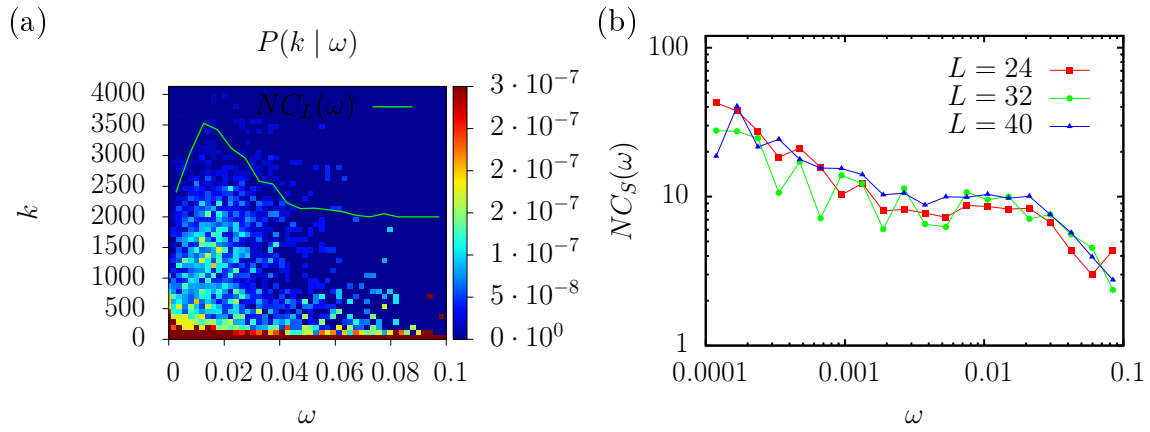

Figure 7.5: (a) $P(k \mid \omega)$ at system size $L = 40$ for the eigenvectors of the Dirac operator of QCD. The line shows the behavior of $NC_L(\omega)$, the contribution of the largely overlapping eigenvector pairs to $NC(\omega)$. (b) $NC_S(\omega)$ which characterizes the contribution of eigenvectors with small overlap.

should be a crossing point, which is not precisely visible due to finite size effects and irrelevant scaling.

Important to mention that since there are strong correlations between two eigenvectors of a gauge field configuration, described in Section 7.4, we had to take them into account. We took 26 values of energy, E_i, from the range $E \in [0.32, 0.35]$. In order to decrease the numerical noise for the kth gauge-field configuration we performed averaging for of all the eigenvectors in a $\Delta E = 0.0012$ wide energy range around E_i, resulting R_{qi}^k and S_{qi}^k. The GMFEs $\tilde{\alpha}_q(E_i, L, \ell)$ and $\tilde{D}_q(E_i, L, \ell)$ can be computed from averages for R_{qi}^k and S_{qi}^k over the index k. However, GMFEs at different energies $\tilde{\alpha}_q(E_i, L, \ell)$ and $\tilde{\alpha}_q(E_j, L, \ell)$ (or $\tilde{D}_q(E_i, L, \ell)$ and $\tilde{D}_q(E_j, L, \ell)$) are of course correlated, since the eigenvectors we used to calculate them are correlated. Therefore to compute the χ^2, we had to use the whole covariance matrix, and not just the variances even for the fixed λ method.

For the MFSS, described in Section 3.2, we used first fixed $\lambda = 0.125$, because this value is close to the previously used $\lambda = 0.1$, and it is compatible with several system sizes, listed in Table 7.1. This fixed λ method is more stable, since the number of parameters to fit grows only linear with the expansion orders. Stability was a serious issue, because the largest system size, listed in Table 7.1, was about the half we used for the Anderson models in Wigner-Dyson classes, see Table 4.1, or for the quantum percolation model, see Table 5.1. This resulted that fits were stable for adding or removing an expansion parameter only in the range $0 \leq q \leq 1$.

The results are independent of q and the type of averaging, as expected. The results at different values of q were calculated from the same quark modes, hence they are strongly correlated and cannot be averaged. Since critical parameters computed from $D_{0.1}^{ens}$ represent well the results and their error bar a small, we choose these values for our final result. Our critical point, $E_c = 0.3355$ (0.3345..0.3364), is compatible with the values of Giordano *et. al*, $E_c^G = 0.33637$ (0.33589..0.33685) (using the double of the standard deviation as error bar listed in Table I of Ref. [65]). The critical point and

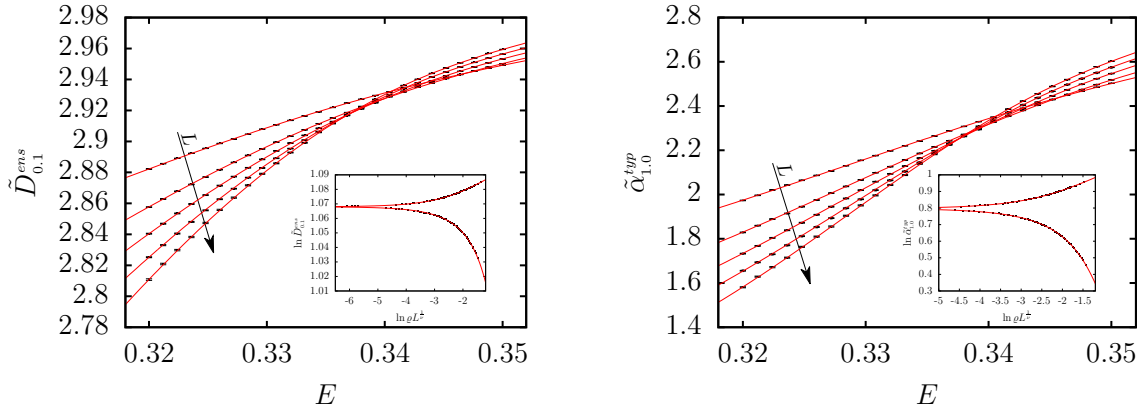

Figure 7.6: Dots are the raw data for GMFEs (a) $\tilde{D}^{ens}_{0.1}$ (b) $\tilde{\alpha}^{typ}_{1.0}$ at fixed $\lambda = 0.125$ for different system sizes. Red line is the best fit obtained by MFSS. Insets are scaling functions on a log-log scale, after the irrelevant term was subtracted. Error bars are shown only on the large figures, in order not to overcomplicate the insets.

critical exponent is also independent of the width of the energy window, ΔE, used for averaging, which is shown in Figure 7.8. Our critical exponent, $\nu = 1.449$ (1.429..1.481), also agrees with the result of Giordano *et. al*, $\nu^G = 1.434$ (1.33..1.538) [65], and with our value in Table 4.5 for the unitary Anderson model. However, our values for the critical point seem to be a bit lower, and for the critical exponent seem to be higher than the reference values, our results at different values of q are strongly correlated, therefore this cannot be interpreted as a tendency. On the other hand our value for the irrelevant exponent, $y = 3.178$ (2.258..4.134), is significantly different from the value in Table 4.5. The irrelevant term with the second or the third largest irrelevant exponent might have larger contribution at our smaller system sizes compared to the ones for the Anderson model. Therefore we might measured a different irrelevant exponent. It is also possible, that at our smaller system sizes we measured a mixture of different irrelevant exponents resulting an effective irrelevant exponent, which can explain our difference. But since irrelevant exponent describes a sub-leading term, it is extremely hard to calculate it accurately. Therefore it is also possible, that our results are not complete, and they deserves further analysis. The fact that MFSS converges for the problem, shows that multifractality is present, and the system undergoes a true localization-delocalization transition. As mentioned in Section 1.3, one expects similar behavior in the bulk of a chiral and the corresponding non-chiral class. From the symmetries of the Dirac operator one expects unitary symmetry, and as written above, our critical exponent for QCD matches with our value for the unitary Anderson model. This shows that the transition belongs to the chiral unitary Anderson class.

The varying λ method resulted more precise critical parameters for the Anderson models in the WD classes (see Section 4.4), and it also provides the multifractal exponent. Therefore we tried to use this method also. The $\chi^2/(N_{df}-1)$ ratio reached a value close to unity only if we left out the smallest system sizes, leading to $L_{min} = 36$, and if we used data corresponding to $\ell = 1$ and 2. The reason behind this is that by adding new values

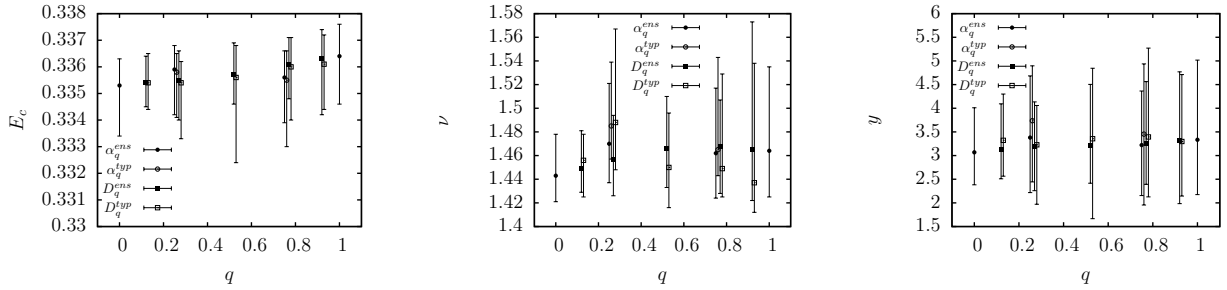

Figure 7.7: Critical parameters of the MFSS for the eigenvectors of the QCD Dirac operator at fixed $\lambda = 0.125$. Corresponding data is listed in Table 7.2.

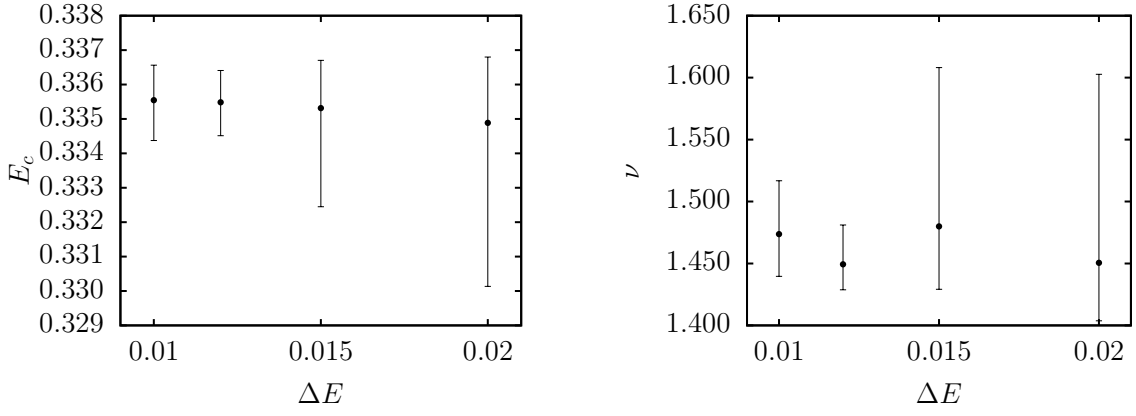

Figure 7.8: Critical point and critical exponent obtained from $D_{0.1}^{ens}$ at fixed $\lambda = 0.125$ for various energy windows ΔE. Error bars denote 95% confidence band.

q	exp	W_c	ν	y	NDF	χ^2	$n_r n_{ir} n_\varrho n_\eta$
0	$\alpha^{ens/typ}$	0.3353 (0.3340..0.3363)	1.443 (1.421..1.478)	3.069 (2.382..4.010)	118	120	4 2 2 0
0.1	D^{ens}	0.3355 (0.3345..0.3364)	1.449 (1.429..1.481)	3.130 (2.509..4.094)	118	119	4 2 2 0
	D^{typ}	0.3354 (0.3344..0.3365)	1.456 (1.425..1.478)	3.322 (2.564..4.301)	118	120	4 2 2 0
0.25	α^{ens}	0.3359 (0.3342..0.3368)	1.470 (1.437..1.521)	3.380 (2.217..4.683)	118	118	4 2 2 0
	α^{typ}	0.3358 (0.3341..0.3365)	1.485 (1.457..1.539)	3.736 (2.443..4.896)	117	121	4 2 2 1
	D^{ens}	0.3355 (0.3340..0.3366)	1.457 (1.426..1.494)	3.190 (2.258..4.134)	118	117	4 2 2 0
	D^{typ}	0.3354 (0.3333..0.3362)	1.488 (1.448..1.567)	3.228 (1.971..4.058)	117	116	4 3 2 0
0.5	D^{ens}	0.3357 (0.3346..0.3369)	1.466 (1.433..1.510)	3.220 (2.416..4.504)	118	117	4 2 2 0
	D^{typ}	0.3356 (0.3324..0.3368)	1.450 (1.416..1.496)	3.356 (1.666..4.845)	116	117	4 3 2 1
0.75	α^{ens}	0.3356 (0.3339..0.3366)	1.462 (1.424..1.517)	3.221 (2.154..4.364)	118	119	4 2 2 0
	α^{typ}	0.3355 (0.3330..0.3366)	1.465 (1.443..1.543)	3.453 (1.955..4.937)	117	122	4 2 2 1
	D^{ens}	0.3361 (0.3348..0.3371)	1.468 (1.428..1.507)	3.264 (2.392..4.563)	118	117	4 2 2 0
	D^{typ}	0.3360 (0.3340..0.3371)	1.449 (1.425..1.529)	3.394 (2.127..5.271)	117	119	4 2 2 1
0.9	D^{ens}	0.3363 (0.3342..0.3374)	1.465 (1.422..1.573)	3.313 (1.984..4.770)	118	118	4 2 2 0
	D^{typ}	0.3361 (0.3344..0.3372)	1.437 (1.412..1.538)	3.298 (2.145..4.711)	117	118	4 2 2 1
1	$\alpha^{ens/typ}$	0.3364 (0.3346..0.3376)	1.464 (1.425..1.535)	3.334 (2.175..5.018)	118	118	4 2 2 0

Table 7.2: Result of the MFSS at fixed $\lambda = 0.125$ for the eigenvectors of the Dirac operator of QCD, which is visible in Figure 7.7.

of L or ℓ one adds new information, but in the same time the scaling function must be fitted for a wider range. The interplay of these two effects resulted in convergence using data described above only.

However, using $L_{min} = 36$ and $\ell = 1, 2$ resulted in convergence, fits were still unstable for changing the expansion orders. We have similar amount of independent data as for the fixed λ case, but many more parameters to fit, as described in Section 3.2. In order to be able to estimate the MFEs, we fixed the critical energy and the critical exponent to the average of the values obtained with the fixed-λ method, $E_c^{av} = 0.3357$ and $\nu^{av} = 1.461$, in this way stabilizing the fits. The systematic uncertainty corresponding to this procedure was estimated by repeating the fits with E_c and ν fixed to one of the four possible combinations of the values $E_c^{l,u}$ and $\nu^{l,u}$, which are the average of the lower and upper boundaries of the confidence interval of E_c and ν, respectively (see Figure 7.7 and Table 7.2). The largest and smallest values obtained in this way were then used as upper and lower error bar on the MFEs. We experienced that the main source of uncertainty comes from the choice of E_c, while fits are much less sensitive to the choice of ν. Moreover, statistical errors (estimated by Monte-Carlo) were comparatively negligible.

The results of this procedure are depicted in Figure 7.9. A set of nontrivial MFEs was obtained, thus providing direct evidence of the multifractality of the critical eigenfunctions of the QCD Dirac operator. Moreover, our results for the MFEs in QCD are compatible with the ones obtained in the unitary Anderson model, which further confirms that the transition belongs to the chiral unitary Anderson class.

(a) (b)

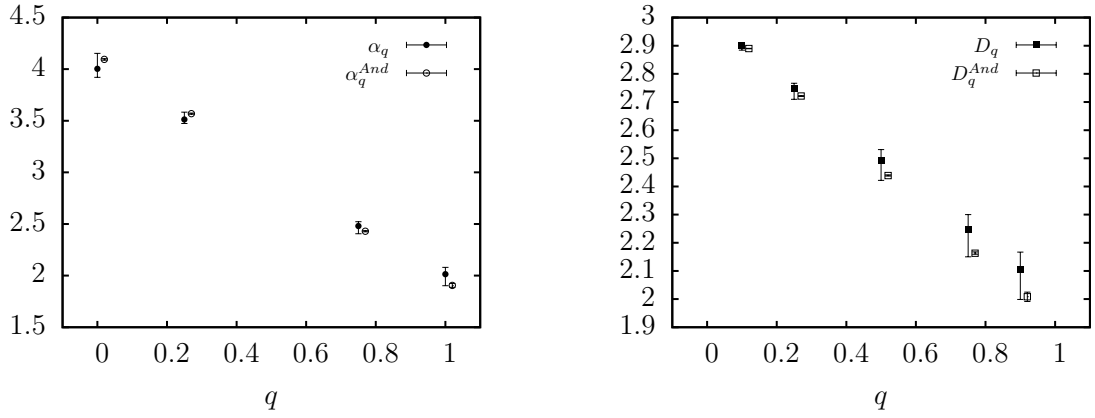

Figure 7.9: Estimated values of MFEs (a) α_q and (b) D_q of the QCD model, and the MFEs of the unitary Anderson model taken from Table 4.10. Values for the Anderson model were shifted a bit horizontally for better sight.

7.6 Summary

In this chapter we investigated the Anderson transition in the spectrum of the Dirac operator of QCD at high temperature, which was found by the authors of Ref. [65] using spectral statistics. Our aim was to examine the transition through eigenvectors, and search for similarities between this model and the corresponding Anderson model. The Dirac operator has only chiral symmetry, thus the transition should belong to the chiral unitary Anderson class. Because of the similarity between the bulk behavior of chiral- and corresponding non-chiral classes, we compared the results to the unitary Anderson model. First we examined the correlations between eigenvectors of an edge configuration. Even though probably doublets of the fermion doubling problem disturb the picture in the localized regime, we found basically the same phenomenon for the Dirac operator of QCD and the unitary Anderson model. MFSS with the fixed λ method resulted matching results with Ref. [65] for the critical point, and with our results for the critical exponent for the unitary Anderson model, see Figure 7.7. For several reasons we could only approximate the MFEs using MFSS at different values of ℓ if we fixed the critical point and critical exponent. The resulting MFEs are compatible with the MFEs of the unitary Anderson model, see Figure 7.9. Our work confirms that there is a metal-insulator phase transition in the spectrum of the Dirac operator of QCD, and it belongs to the chiral-unitary Anderson class. Our work shows also that critical wave-functions are multifractals. The physical consequences of the QCD Anderson transition and of multifractality still largely need to be explored. Further work along these lines might prove beneficial for condensed matter physics as well, as it approaches the subject of localization/delocalization transitions from a broader perspective.

Chapter 8

Thesis statements, publications and acronyms

8.1 Thesis statements

In this Section I list the thesis statements.

1. I examined the three-dimensional Anderson models belonging to the conventional Wigner-Dyson symmetry classes with the help of multifractal finite-size scaling. With the fixed λ and varying λ methods I confirmed the presence of multifractality in all three Wigner-Dyson symmetry classes. I obtained the critical point, critical exponent and irrelevant exponent for each symmetry class. These parameters were in agreement with each other for the different methods, and with previous results known from the literature. The varying λ method provided significantly different critical exponents for the different symmetry classes. I computed the multifractal exponents also for every symmetry class. Multifractal exponents of different symmetry classes were very close to each other for fixed q, but significantly different for most of the values of q.
   Publication **[a]** is related to this thesis point.

2. I investigated numerically the quantum percolation model in 3D. In order to describe the localization transition I used multifractal finite-size scaling. I determined the mobility edge of the system, confirming previous calculations. For the critical exponent I obtained energy-independent values within 95% confidence level. The average of these values is the same as the critical exponent of the orthogonal Anderson model, implying that quantum percolation belongs to the chiral orthogonal Anderson universality class. I also determined the multifractal exponents D_q and α_q along the mobility edge, and for larger values of p_c^Q I found no significant difference from the Anderson model confirming the statement of the universality class further.
   Publication **[b]** is related to this thesis point.

3. I have shown that the Anderson model at strong localization shows non-trivial behavior especially approaching the band-edge. I showed that only a 2-site or a

3-site model can describe qualitatively well the system.
Publication **[c]** is related to this thesis point.

4. I investigated the Anderson transition in the spectrum of the Dirac operator of Quantum chromodynamics at high temperature. I found similar correlations between the eigenvectors of the Dirac operator of QCD and the Hamiltonian of the unitary Anderson model. Multifractal finite-size scaling with the fixed λ method resulted matching results with previous works for the critical point, and with my results for the critical exponent for the unitary Anderson model. The approximate values of the multifractal exponents were compatible with the multifractal exponents of the unitary Anderson model. My work confirms that there is a metal-insulator phase transition in the spectrum of the Dirac operator of QCD, and it belongs to the chiral-unitary Anderson class.
Publication **[d]** and **[e]** are related to this thesis point.

8.2 Publications

Publications related to this thesis:

[a] L. Ujfalusi and I. Varga : Finite size scaling and multifractality at the Anderson transition for the three Wigner-Dyson symmetry classes in three dimensions, *Physical Review B* **91**, 184206 (2015).

[b] L. Ujfalusi and I. Varga: Quantum percolation transition in three dimensions: Density of states, finite-size scaling, and multifractality, *Physical Review B* **90**, 174203 (2014).

[c] L. Ujfalusi and I. Varga: Anderson localization at large disorder, *Physical Review B* **86**, 125143 (2012).

[d] M. Giordano, T. G. Kovács, F. Pittler, L. Ujfalusi and I. Varga : Dirac eigenmodes at the QCD Anderson transition, PoS LATTICE2014 (2015) 212.

[e] L. Ujfalusi, M. Giordano, F. Pittler, T. G. Kovács and I. Varga: Anderson transition and multifractals in the spectrum of the Dirac operator of Quantum Chromodynamics at high temperature, submitted to PRB

Other publication:

[f] L. Ujfalusi, D. Schumayer and I. Varga: Quantum chaos in one dimension?, *Physical Review E* **84**, 016230 (2011).

8.3 Acronyms

MIT	Metal-insulator transition
AMIT	Anderson Metal-insulator transition
DOS	Density of states
LDOS	Local density of states
WD	Wigner-Dyson
IPR	Inverse participation ratio
GIPR	Generalized inverse participation ratio
MFE	Multifractal exponent
GMFE	Generalized multifractal exponent
FSS	Finite-size scaling
MFSS	Multifractal finite-size scaling

Table 8.1: Anacronyms used in this work.

Bibliography

[1] P. W. Anderson, *Phys. Rev.* **109**, 1492 (1958).

[2] V. Dobrosavljevic, *Introduction to Metal-Insulator Transitions* (Oxford University Press, Oxford, 2012).

[3] *50 Years of Anderson Localization*, ed. E. Abrahams (World Scientific, Singapore, 2010); *The Anderson Transition and its Ramifications – Localisation, Quantum Interference, and Interactions*, eds. T. Brandes and S. Kettemann (Springer, Berlin, 2003); P. A. Lee and T. V. Ramakrishnan, *Rev. Mod. Phys.* **57**, 287 (1985).

[4] A. MacKinnon and B. Kramer, Rep. Prog. Phys. **56**, 1469 (1993).

[5] F. Evers and A. D. Mirlin, *Rev. of Mod. Phys.* **80**, 1355 (2008).

[6] H. Aoki and T. Ando, *Solid State Comm.* **38**, 1079 (1981).

[7] M.V. Feigel'man, L.B. Ioffe, V.E. Kravtsov, E. Cuevas, *Annals of Physics* **325**, 1390 (2010), I. S. Burmistrov, I. V. Gornyi and A. D. Mirlin, *Phys. Rev. Lett.* **108**, 017002 (2012).

[8] S. Kettemann, E. R. Mucciolo, I. Varga and K. Slevin, *Phys. Rev. B* **85**, 115112 (2012).

[9] M. Sade, T. Kalisky, S. Havlin, and R. Berkovits, *Phys. Rev. E* 72, 066123 (2005).

[10] A. Richardella, P. Roushan, S. Mack, B. Zhou, D. A. Huse, D. D. Awschalom, and A. Yazdani, *Science* **327**, 665, (2010).

[11] F. Jendrzejewski, A. Bernard, K. Müller, P. Cheinet, V. Josse, M. Piraud, L. Pezzé, L. Sanchez-Palencia, A. Aspect and P. Bouyer, *Nature Physics* **8**, 398, (2012).

[12] H. Hu, A. Strybulevych, J. H. Page, S.E. Skipetrov, and B.A. van Tiggelen, *Nature Physics* **4**, 945 (2008).

[13] S. Faez, A. Strybulevych, J. H. Page, A. Lagendijk, and B. A. van Tiggelen *Phys. Rev. Lett.* **103**, 155703 (2009).

[14] M. Segev, Y. Silberberg and D. N. Christodoulides, *Nature Photonics* **7**, 197, (2013).

[15] R. Nandkishore and D. A. Huse, *Annu. Rev. Condens. Matter Phys.* **6**, 15, (2015).

[16] N. F. Mott, *Metal-Insulator Transition* (Taylor & Francis, London, 1990).

[17] T. F. Rosenbaum K. Andres, G. A. Thomas and R. N. Bhatt, *Phys. Rev. Lett.* **45** 1723 (1980).

[18] F. Wegner, *Z. Phys. B* **35**, 207 (1979).

[19] E. Abrahams, P. W. Anderson, D. C. Licciardello and T. V. Ramakrishnan, *Phys. Rev. Lett* **42**, 673 (1979).

[20] I. M. Lifshitz, Adv. Phys. **13**, 483 (1964).

[21] H. Grussbach and M. Schreiber, *Phys. Rev. B* **51**, 663 (1995).

[22] S. N. Evangelou and D. E. Katsanos, *J. Phys. A: Math. Gen.* **36**, 3237 (2003).

[23] P. Biswas, P. Cain, R. A. Römer and M. Schreiber, *Phys. Status Solidi B* **218**, 205 (2000).

[24] A. L. Stella and C. Vanderzande, *Phys. Rev. Lett.* **62**, 1067 (1989).

[25] M. Janssen, *Fluctuations and localization in mesoscopics electron systems* (World Scientific Lecture Notes in Physics - Vol. 64, Singapore, 2001); M. Janssen, *Phys. Rep.* **295**, 1 (1998).

[26] E. Cuevas and V. E. Kravtsov, *Phys. Rev. B* **76**, 235119 (2007).

[27] A. D. Mirlin, Y. V. Fyodorov, A. Mildenberger, and F. Evers, *Phys. Rev. Lett.* **97**, 046803 (2006).

[28] A. Mildenberger and F. Evers, *Phys. Rev. B* **75**, 041303(R) (2007).

[29] F. Evers, A. Mildenberger, and A. D. Mirlin, *Phys. Stat. Sol. B* **245**, 284 (2008); F. Evers, A. Mildenberger, and A. D. Mirlin, *Phys. Rev. Lett.* **101**, 116803 (2008).

[30] L. J. Vasquez, A. Rodriguez, and R. A. Römer, *Phys. Rev. B* **78**, 195106 (2008); A. Rodriguez, L. J. Vasquez, and R. A. Römer, *Phys. Rev. B* **78**, 195107 (2008); A. Rodriguez, L. J. Vasquez, and R. A. Römer, *Phys. Rev. Lett.* **102**, 106406 (2009).

[31] C. Monthus and Th. Garel, *J. Stat. Mech.* **2011**, P05005 (2011); see also C. Monthus, B. Berche, and Ch. Chatelain, *J. Stat. Mech.* **2009**, P12002 (2009).

[32] A. Rodriguez, L. J. Vasquez, K. Slevin and R. A. Römer, *Phys. Rev. B* **84**, 134209 (2011).

[33] J. Cardy *Scaling and Renormalization in Statistical Physics* (Cambridge University Press, Cambridge UK, 1996).

[34] D. J. Thouless, *Phys. Rep.* **13**, 93 (1974).

[35] F. Wegner, *Z. Phys. B* **25**, 327 (1976).

[36] F. James and M. Roos, *Comput. Phys. Commun.* **10**, 343 (1975).

[37] A. Rodriguez, L. J. Vasquez, K. Slevin and R. A. Römer, *Phys. Rev. Lett.* **105**, 046403 (2010).

[38] K. Slevin and T. Ohtsuki, *Phys. Rev. Lett.* **78**, 4083 (1997).

[39] Y. Asada, K. Slevin and T. Ohtsuki, *J. Phys. Soc. Jpn.* **74**, 238 (2005).

[40] O. Schenk, M. Bollhöfer and R. A. Römer, *SIAM Review* **50**, 91 (2008).

[41] A. Stathopoulos and J. R. McCombs *ACM Transaction on Mathematical Software* **37**, 2, 21:1–21:30 (2010).

[42] T. Dröse, M. Batsch, I. K. Zharekeshev, B. Kramer, *Phys. Rev. B.* **57**, 37 (1998).

[43] F. Wegner, *Nucl. Phys. B* **280**, 210 (1987).

[44] D. Stauffert and A. Aharony, *Introduction To Percolation Theory*, CRC Press, (1994).

[45] K. Christensen and N. R. Moloney, *Complexity and Criticality*, Imperial College Press, (2005).

[46] M. E. J. Newman and R. M. Ziff, *Phys. Rev. Letters* **85**, 4104 (2000).

[47] J. Wang, Z. Zhou, W. Zhang, T. M. Garoni, and Y. Deng, *Phys. Rev. E* **87**, 052107 (2013).

[48] S. Kirkpatrick, T. P. Eggarter, *Phys. Rev. B* **6**, 3598 (1972).

[49] A. Kusy, A. W. Stadler, G. Haldas, R. Sikora, *Physica A* **241**, 403 (1997).

[50] C. M. Soukoulis, Q. Li, G. S. Grest, *Phys. Rev. B* **45**, 7724 (1992).

[51] J. Hoshen and R. Kopelman, *Phys. Rev. B* **14**, 3438 (1976).

[52] G. Schubert, H. Fehske, *Lec. Not. Phys.* **762**, 135 (2009).

[53] Ch. Bordenave, A. Sen, B. Virág, arXiv:1308.3755

[54] G. G. Naumis, Ch. Wang and R. A. Barrio, *Phys. Rev. B* **65**, 134203 (2002).

[55] I. Travenec, Int. J. Mod. Phys. B, 22, 5217 (2008).

[56] L. J. Root, J. D. Bauer, J. L. Skinner, *Phys. Rev. B* **37**, 5518 (1988).

[57] Th. Koslowski, W. von Niessen, *Phys. Rev. B* **44**, 9926 (1991).

[58] R. Berkovits, Y. Avishai, *Phys. Rev. B* **53**, R16125(R) (1996).

[59] A. Kaneko, T. Ohtsuki, *J. Phys. Soc. Jap.* **68**, 1488 (1999).

[60] I. Varga, Helv. Phys. Acta, **68**, 64 (1995).

[61] S. Johri and R. N. Bhatt, *Phys. Rev. Lett.* **109**, 076402 (2012); *Phys. Rev. B* **86**, 125140 (2012); R. N. Bhatt and S. Johri, *Int. J. Mod. Phys. Conf. Ser.* **11**, 79 (2012).

[62] F. Pittler, *Poisson - Random Matrix transition in the QCD Dirac spectrum*, Ph.D. thesis (2013).

[63] T. G. Kovács and F. Pittler, *Phys. Rev. Lett.* **105**, 192001 (2010).

[64] T. G. Kovács and F. Pittler, *Phys. Rev. D* **86**, 114515 (2012).

[65] M. Giordano, T. G. Kovács and F. Pittler, *Phys. Rev. Lett.* 112, 102002 (2014).

[66] J. J. M. Verbaarschot and T. Wettig, *Annu. Rev. Nucl. Part. Sci.* **50**, 343 (2000).

[67] I. Montvay and G. Münster, *Quantum fields on a lattice* (Cambridge University Press, Cambridge UK, 1994).

[68] K. G. Wilson, *Phys. Rev. D* **10**, 2445 (1974).

[69] L. Susskind, *Phys. Rev. D* **16**, 3031 (1977); J. B. Kogut and L. Susskind, Phys. Rev. D **11**, 395 (1975); T. Banks *et al. Phys. Rev. D* **15**, 1111 (1977).

[70] Y. Aoki, Z. Fodor, S. D. Katz and K. K. Szabo, JHEP **0601**, 089 (2006).

[71] S. Borsanyi, G. Endrodi, Z. Fodor, A. Jakovac, S. D. Katz, S. Krieg, C. Ratti and K. K. Szabo, JHEP **1011**, 077 (2010).